An Energy-Regenerative Vehicle Suspension System – Development, Optimization, and Improvement

by

Bo Huang

M.Phil., The Hong Kong University of Science and Technology, 2010
B.Eng., Tianjin University, 2007

Thesis Submitted in Partial Fulfillment of the
Requirements for the Degree of
Doctor of Philosophy

in the
School of Mechatronic Systems Engineering
Faculty of Applied Sciences

SIMON FRASER UNIVERSITY

Summer 2016

Approval

Name: **Bo Huang**

Degree: **Doctor of Philosophy**

Title of Thesis: ***An Energy-Regenerative Vehicle Suspension System – Development, Optimization, and Improvement***

Examining Committee: **Chair:** Amr Marzouk
Lecturer

Farid Golnaraghi
Senior Supervisor
Professor

Mehrdad Moallem
Supervisor
Professor

Siamak Arzanpour
Supervisor
Associate Professor

Gary Wang
Internal Examiner
Professor
School of Mechatronic Systems Engineering

Ebrahim Esmailzadeh
External Examiner
Professor
Department of Automotive, Mechanical and Manufacturing Engineering
University of Ontario Institute of Technology

Date Defended/Approved: August 23, 2016

Abstract

With the rapid development of hybrid and fully electric vehicles, electromagnetic suspensions have shown great potential for capturing energy while offering high-level ride comfort. The objective of this research was to develop an electromagnetic-based vehicle suspension system that allows for regeneration of road-induced vibration energy and supplies better dynamics control. A small-scale proof-of-concept system consisting of a mass-spring-damper system, ball screw mechanism, and direct current (DC) machine was designed. The vibration energy in the mass-spring-damper system caused vertical motion of sprung mass and the ball screw mechanism to convert the translational motion into rotary motion, which resulted in the generation of back electromotive force of the DC machine.

Systematic optimization methodologies were utilized to provide for selective adaption of suspension parameters, such as spring constant (rate) and damping coefficient, according to different road surface conditions, including harmonic and stochastic waveforms. By maximizing the average of power generation or minimizing the root-mean-square of the sprung mass's absolute acceleration by selecting optimal parameters, the suspension allowed operation in either energy-oriented mode or control-oriented mode.

Furthermore, a bandwidth enhancement technique utilizing cubic nonlinearities was demonstrated to improve the energy harvesting capability of the suspension system. A self-powered regenerative Skyhook control strategy was proposed to overcome the trade-off between passive control (insufficient control) and active control (external energy demand) for the suspension system.

Keywords: Energy harvesting, regenerative vehicle suspension, design optimization, bandwidth enhancement, Skyhook control

Dedication

To my beloved wife, Xueling, and my daughter, Lydia

To my parents

Acknowledgements

It is my pleasure to express my deep gratitude to my senior supervisor, Dr. Farid Golnaraghi, for his tremendous support and patient guidance during my Ph.D. study. His experience and insight into this research are invaluable, and have helped me advance and achieve my academic goals.

Moreover, I would like to thank my co-supervisor, Dr. Mehrdad Moallem, and my supervisory committee member, Dr. Siamak Arzanpour, for taking their time and effort and providing valuable advices through my research. I would also like to thank my internal and external examiners, Dr. Gary Wang and Dr. Ebrahim Esmailzadeh, for attending my Ph.D. defence and giving helpful feedback on this thesis. In addition, I would like to thank my friends and colleagues, Dr. Chen-Yu Hsieh and Dr. Amr Marzouk, for their collaboration and help in working on this project.

Finally, it does not matter where I am, it matters who I am with that makes life meaningful. I would like to give special thanks to my wife and my parents, for their love that becomes the most important support and encouragement for every progress I have made.

Table of Contents

List of Tables

List of Figures

List of Acronyms

back-EMF	Back electromotive force
cc	Complex conjugate
DC	Direct current
EM	Electromagnetic
EVs	Electrical vehicles
GVs	Gasoline vehicles
MSE	Mean-square error
MR	Magneto-rheological
PSD	Power spectral density
RMS	Root-mean-square
SMR	Switch-mode rectifier
1-DOF	One-degree-of-freedom
2-DOF	Two-degrees-of-freedom

Nomenclature

Symbol	Description	Unit	Symbol	Description	Unit
a	Absolute acceleration transmissibility of the sprung mass	1/s^2	AVG_p	Average of power generation transmissibility	W/m^2
$\overline{AVG_p}$	Normalized value of AVG_p	1	c	Motor damping coefficient	N·s/m
c_f	Viscous damping coefficient	N·s/m	c_{max}	Upper bound of the damping coefficient	N·s/m
c_{min}	Lower bound of the damping coefficient	N·s/m	c_{opt}	Optimal damping coefficient	N·s/m
c_{sa}	Semi-active damping coefficient	N·s/m	c_{sky}	Damping coefficient of the Skyhook damper	N·s/m
d	Coefficient of the ball screw	mm/rad	E_{all}	Total energy into the system	J
E_c	Energy absorbed by the DC motor/generator	J	E_d	Required energy for the damping force	J
E_f	Energy dissipated by viscous damping	J	E_{gen}	Cumulative generated energy	J
E_k	Kinetic and potential energies	J	E_m	Back-EMF voltage	V
E_P	Expectation of generated power by the damper	W	f	Temporal excitation frequency	Hz
F_b	Output force of the shock absorber	N	f_c	Temporal cut-off frequency of the filter to simulate ground-tire interface	Hz
f_{fc}	Full cut-off temporal frequency	Hz	f_n	Natural frequency	Hz
$G_d(n)$	Road displacement PSD	m^3	$G_d(n_0)$	Road roughness coefficient	m^3

I	Current through the load resistor	A	i_L	Instantaneous current through the inductor	A
I_{ref}	Reference current of SMR	A	J_b	Inertia of the ball screw	kg·m^2
J_g	Inertia of the gearbox	kg·m^2	J_m	Inertia of the motor	kg·m^2
k	Spring constant	N/m	k_1	First spring constant of the piecewise spring system	N/m
k_2	Second spring constant of the piecewise spring system	N/m	k_e	Back-EMF coefficient	V/rad/s
k_g	Transmission ratio of the gearbox	1	k_N	Nonlinear stiffness	N/m
k_t	Torque constant	N·m/A	l	Lead ratio of the ball screw	mm/rev
L_a	Inductance in SMR	H	L_N	Nonlinear inductance	H
m	Sprung mass	kg	n	Spatial frequency ($= 0.01\sim10$)	m^{-1}
n_0	Reference spatial frequency ($= 0.1$)	m^{-1}	n_{fc}	Full cut-off spatial frequency	m^{-1}
p	Power generation transmissibility	W/m^2	P_{avg}	Average power flow per cycle	W
P_d	Desired power for the damping force	W	P_{inst}	Instantaneous power generated by the damper	W
R_{int}	Internal resistance of DC motor	Ω	R_{load}	Load resistance	Ω
RMS_a	RMS of absolute acceleration transmissibility	1/s^2	$\overline{RMS_a}$	Normalized value of RMS_a	1
S_{aa}	PSD of absolute acceleration of the sprung mass	m^2/ s^3·rad	S_{vv}	PSD of relative velocity between sprung mass and excitation	m^2/ s·rad

v	Relative velocity transmissibility	1/s	V	Vehicle speed	m/s
V_c	Terminal voltage controlled by SMR	V	V_{load}	Terminal voltage of the load resistor	V
w	Road index (=2)	1	W	Length of the tire footprint	m
x	Displacement of the sprung mass	m	$\dot{x}$	Velocity of the sprung mass	m/s
$\ddot{x}$	Acceleration of the sprung mass	m/s^2	y	Displacement of base excitation	m
$\dot{y}$	Velocity of base excitation	m/s	$\ddot{y}$	Acceleration of base excitation	m/s^2
z	Stroke displacement of the shock absorber	m	$\dot{z}$	Stroke velocity of the shock absorber	m/s
$\ddot{z}$	Stroke acceleration of the shock absorber	m/s^2	α_N	Factor of the nonlinearity	1
Δ	Clearance of the coupler	mm	ζ	Damping ratio	1
η	Total efficiency of power regeneration	1	η_b	Efficiency of the ball screw	1
η_{elec}	Electrical efficiency of power transfer	1	η_g	Efficiency of the gearbox	1
η_{gen}	DC generator efficiency	1	η_{mech}	Mechanical efficiency of energy generation	1
η_s	SMR power conversion efficiency	1	θ	Angular displacement of the motor gear shaft	rad
$\dot{\theta}$	Angular velocity of the motor gear shaft	rad/s	$\ddot{\theta}$	Angular acceleration of the motor gear shaft	rad/s^2
λ	Relative displacement transmissibility	1	σ	Detuning parameter for the nearness of excitation frequency to natural frequency	1

τ_b	Output torque of the shock absorber	N·m	τ_i	Output torque of the motor	N·m
φ	Flux of the inductor	V·s	ω	Excitation frequency	rad/s
ω_c	Radian cut-off frequency of the filter to simulate ground-tire interface	rad/s	ω_n	Natural frequency	rad/s

Chapter 1.

Introduction

Today, conventional gasoline vehicles (GVs) still have the edge in the market. However, partly due to their exhaust gas, air pollution is becoming more serious. Electric vehicles (EVs) are consequently becoming more popular. This has to do with their numerous attractive properties, which are listed below (U.S. Department of Energy, n.d.):

- They are environmentally friendly. EVs help improve the green environment since they emit no exhaust gas pollutants. Also, electricity can be generated from clean energy produced at nuclear-, solar-, or wind-powered plants. Such energy causes no air pollution.
- They are characterized by performance improvements. Electric motors used in EVs offer quieter operation, faster responses, and stronger acceleration than most GVs.
- They cost less. The price of electricity is only about one sixth of that of gas. Moreover, EVs require less maintenance than GVs.
- They are energy efficient. EVs convert about 59-62% of energy from the grid to power their wheels. This is about three times higher than what GVs convert.

With the development of EVs, extending the range of battery power has become increasingly important. This will help overcome the significant battery-related challenges of EVs, for instance, their limited driving ranges and long recharge times. A new approach to increasing the battery range is the use of energy-harvesting technology in vehicle parts such as the suspension system (Hsu, 1996).

Figure 1.1 illustrates a typical suspension system in Mercedes-Benz S-Class vehicles (Mercedes-Benz: Magic Body Control, n.d.). An automotive suspension system supports the vehicle body on the axles and suppresses undesirable vibration from road roughness. It is responsible for enhancing passengers' ride comfort and vehicles' road handling characteristics by absorbing the induced energy from the road into a spring and dissipating it into heat over time using a damper. Traditional suspension systems, such as passive suspension systems, have conventional springs and oil dampers with constant properties that are inexpensive and simple to manufacture, but performance is limited due to their compromise between ride comfort and road handling. To achieve better vibration isolation and control performance, many semi-active and active suspension systems have been designed (Dyer, 2015). However, these sophisticated systems need additional power to realize control tasks. To this end, sufficient available power is of the greatest importance. In addition, range of battery power has been introduced as a new performance indicator for EVs and hybrid EVs.

Figure 1.1 Mercedes-Benz active suspension system

Recent attention to vibration-based energy harvesting has resulted in the creation of techniques for regenerative vehicle suspension. Rather than dissipating energy through viscous damping, the suspension is able to convert the mechanical energy from systems into electrical energy and charge the battery directly. Therefore, a self-powered suspension system has been taken into consideration. The system is able to produce control force using regenerated power from the damper with no additional energy cost. Furthermore, the remaining energy can be used to extend the power range which is a strong merit for EVs.

Different from conventional passive suspension systems, regenerative suspension systems are expected to capture energy within a wide range of excitation frequencies when energy saving is concerned. On the other hand, they also act as vibration isolators to suppress road-disturbance-induced vibrations for improving passengers' comfort. It is necessary to note that the damper behaves contradictorily under these two scenarios. As a result, in the design of system parameters, it is impossible to achieve both objectives simultaneously. In practical applications, most optimization problems are multi-objective in nature. The best solution is usually subjective, taking many issues into consideration, and is contingent on compromise. Therefore, developing a systematic optimization method becomes the key challenge in determining the proper system parameters for energy harvesting – ride control scenarios.

1.1. Traditional Vehicle Suspension Systems

Typically, the suspension system on a vehicle has the following primary functions (Bastow, Howard, & Whitehead, 2004):

(1) To isolate a car body from road disturbances in order to provide good ride quality:

Ride quality in general can be qualified by the vertical acceleration of the passenger locations. The presence of a well-designed suspension provides isolation by reducing the vibratory forces transmitted from the axle to the vehicle body. This in turn reduces vehicle body acceleration. In the case of the two-degrees-of-freedom (2-DOF) quarter-car suspension as shown in Figure 1.2, sprung mass acceleration $\ddot{x}_s$ can be used to quantify ride quality.

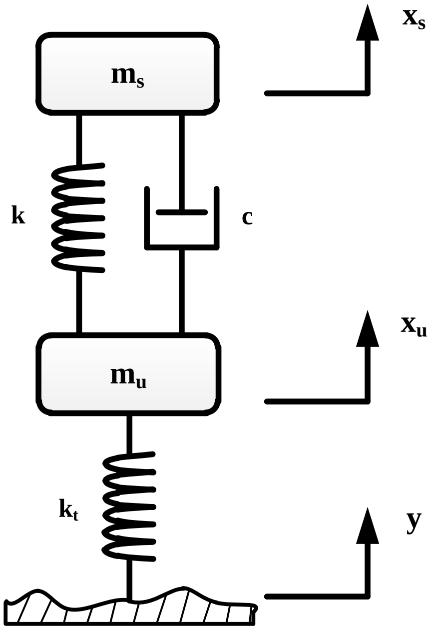

Figure 1.2 2-DOF quarter-car suspension model

(2) To keep good road holding:

The road holding performance of a vehicle can be characterized in terms of its cornering, braking and traction abilities. Improved cornering, braking and traction are obtained if the variations in normal tire load are minimized. This is because the lateral and longitudinal forces generated by a tire depend directly on the normal tire load. Since a tire roughly behaves like a spring in response to vertical forces, variations in normal tire load can be directly related to vertical tire deflection $(x_u - y)$. The road holding performance of a suspension can therefore be quantified in terms of tire deflection performance.

(3) To provide good handling:

The pitch and roll accelerations of a vehicle during cornering, braking and traction are measures of good handling. Half-car and full-car models can be used to study the pitch and roll performance of a vehicle. A good suspension system should ensure that pitch and roll motion are minimized.

(4) To support the vehicle’s static weight:

This task is performed well if the rattle space requirements in the vehicle are kept small. In the case of the quarter-car model, it can be quantified in terms of the maximum suspension deflection $(x_s - x_u)$ undergone by the suspension.

Based on controllability, suspension systems can be classified as passive, semi-active, or active systems. The simplest model of suspension systems is considered to be a one-degree-of-freedom (1-DOF) linear mass-spring-dashpot system, as shown in Figure 1.3, where (a), (b), and (c) indicate passive, semi-active, and active suspension systems, respectively.

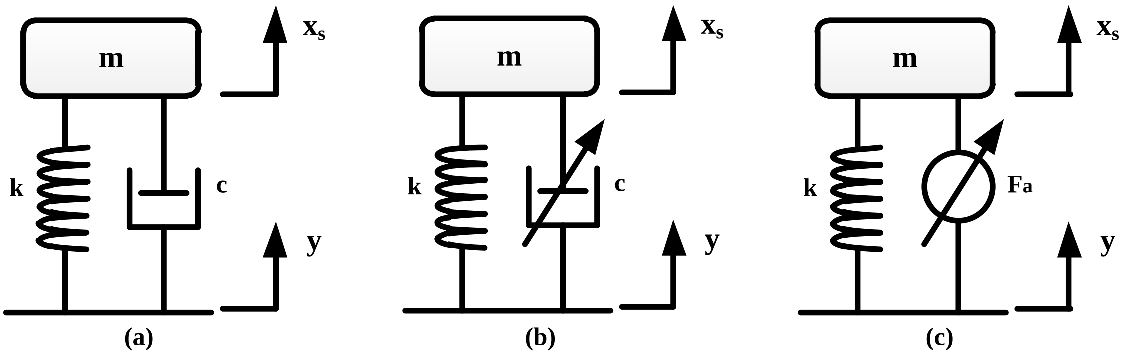

Figure 1.3 1-DOF linear model of suspension systems: (a) passive suspension, (b) semi-active suspension, and (c) active suspension

1.1.1. Passive Suspension Systems

Passive suspensions are the most common systems that are utilized in passenger vehicles. As indicated in Figure 1.3 (a), these systems are composed of conventional springs and dampers with fixed characteristics. The designer presets the parameter properties, such as spring constant and damping coefficient, to achieve an optimum performance for a certain application. Since the parameter values are not tunable, suspension performance is different under different conditions, and it is a compromise between ride comfort and road handling (Gillespie, 1992). On the other hand, passive suspension systems require no external power and are mechanically reliable. They are also simple and inexpensive to manufacture and are easily established.

1.1.2. Semi-Active Suspension Systems

Semi-active suspensions were first proposed by (Karnopp, Crosby, & Harwood, 1974) and have increasingly gained popularity in vehicle suspension applications. These systems can only change the damping coefficient, and do not add energy to the suspension system. The most popular method in this category is Skyhook control, which is an idea stating that the mass body can maintain a stable posture if it is travelling suspended by an imaginary straight line (i.e. Skyhook). This theory forms the bases of some other semi-active control methods, such as Rakheja-Sankar control (Rakheja & Sankar, 1985). They are referred to as adaptive-passive suspensions to some extent. The advantage of these systems over passive suspension systems is that their damping properties are able to be tuned to different levels through applying a low-power electrical command signal to a semi-active damper, as shown in Figure 1.3 (b). The command signal changes either the oil flow rate of the solenoid valve dampers or the properties of the material inside the magneto-rheological (MR) dampers. The other advantage of semi-active suspensions is they are essentially passive devices with adjustable properties (e.g., damping ratio). Therefore, they will act as passive suspensions if semi-active control fails, so they are robustly stable and more stable than active suspension systems. Semi-active suspension systems are considered to be a compromise between passive and active suspension systems (Alanoly & Sankar, 1987). MR-based suspension dampers have been developed and commercialized by Delphi Automotive Corporation and named MagneRide (Magneride™ Controlled Suspension System, n.d.). This system has been utilized in a number of high-end vehicles, such as GM Cadillac, Audi, and Ferrari.

1.1.3. Active Suspension Systems

In most cases, active suspension systems use hydraulic actuators to provide a desired force, which can actively control the acceleration and relative motion of the vehicle’s body by using external power. (Thompson, 1976) first applied modern optimal control theory to the design of an active suspension system for a motor vehicle. (Karnopp, 1983) studied an active suspension concept involving active damping force with velocity feedback. The essential elements of an active suspension system are the sensors that measure the system’s movement in real time. Although active suspensions have better control performance than semi-active and passive suspensions, their high power consumption, weight, cost, and low reliability/stability limit their practical implementation by vehicle manufacturers. Figure 1.3 (c) depicts a generalized active suspension system where F_a is the active damping force instead of the damping properties in the passive and semi-active suspension systems. Developed products include Mercedes-Benz’s Active Body Control System (Mercedes-Benz: Active Body Control ABC, n.d.), Bose’s linear Electromagnetic (EM) Suspension System (Bose Suspension System, n.d.), and Michelin’s Active Wheel System (Adcock, 2012).

1.2. Energy-Regenerative Suspension Systems

EM motors were first proposed for use as energy-regenerative dampers two decades age. From then on, they have held the interest of many researchers. Basically there are two different kinds of EM motors: linear and rotary. They have very different properties, and a number of researches on these two kinds of motors have been conducted. (Hsu, 1996) addressed the application of EM motors as actuators of active suspension systems and analyzed their power-recovery property. His analysis indicated that under 97 km/h highway driving condition, the potentially recoverable power is about 100 watts per wheel, which is about 5% of the propulsion power to maintain GM's EV1 at the same speed. (Suda, Nakadai, & Nakano, 1998) proposed a mechanism with two linear direct current (DC) motors aligned vertically. The upper one was utilized as an actuator for Skyhook control, and the lower one was utilized as a regenerative damper. The study confirmed the possibility of a hybrid system that attains active control only with regenerated vibration energy. (Nakano, Suda, & Nakadai, 2003) improved the regenerative suspension system using a single linear DC motor. The study showed that self-powered active control is attainable and had a suppression performance similar to externally powered active control. (Suda, Shiiba, Hio, Kawamoto, Kondo, & Yamagata, 2004) proposed an EM damper consisting of a rotary DC motor, planetary gears, ball screw, and nut, as shown in Figure 1.4. By utilizing the power electronic circuits, the EM damper achieved controllable and tunable nonlinear damping force for ride comfort improvement. Since it was used as an active suspension and energy generator simultaneously, no external power source was needed. Later this technique was put into other applications, such as the control of truck cabins (Nakano, 2004). (Zhang, Huang, Yu, Gu, & Li, 2007) designed an energy-regenerative actuator consisting of a three-phase brushless DC motor with a lead screw. The experiment results showed the total generated power was 11.73 watts. (Stribrsky, Hyniova, Honcu, & Kruczek, 2007) presented an active suspension system using a linear AC motor. The system was able to recuperate energy and maintain the energy balance using H_∞ control. The investigation of energy regeneration of active suspension systems in hybrid EVs by (Montazeri-Gh & Soleymani, 2010) indicated that around 68 watts of power was regenerated on a smooth highway, which is less than that needed by active control. The regenerated power made contributions, but the system was not completely self-powered. (Ebrahimi, Bolandhemmat, Khamesee, & Golnaraghi, 2011) proposed a hybrid linear EM damper based on the eddy current damping effect, which was utilized as a source of passive damping. The EM damper consisted of a fixed stator and a movable slider, as shown in Figure 1.5. The eddy currents produced a repulsive force that was proportional to the velocity between the slider and the stator, and acted as a viscous damper. Furthermore, it had energy harvesting capability and so did not require an external power supply. (David & Bobrovsky, 2011) proposed a similar active suspension with energy regeneration capabilities based on a linear generator. About 5% to 10% of a vehicle's power consumption might be restored by using their proposed suspension configurations. (Li, Zuo, Kuang, & Luhrs, 2012) introduced an EM shock absorber based on a rack-pinion mechanism for the purpose of energy harvesting and vibration suppression, as illustrated in Figure 1.6. The road test showed that peak power of 67.5 watts and average power of 19.2 watts could be obtained from four shock absorbers at 48 km/h (Li, Zuo, Luhrs, Lin, & Qin, 2013). (Singal & Rajamani, 2013) explored the idea of a fully self-powered active suspension system, providing performance similar to that of the active system at zero energy cost. However, the results were only based on sinusoidal excitation, which is not suitable to real-world situations. (Sabzehgar, Maravandi, & Moallem, 2014) designed an algebraic screw mechanism paired with a rotary permanent magnet synchronous generator that offered high efficiency.

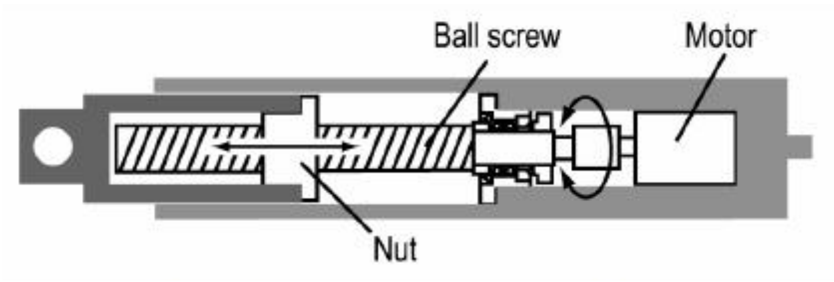

Figure 1.4 Electromagnetic (EM) damper using ball screw and nut

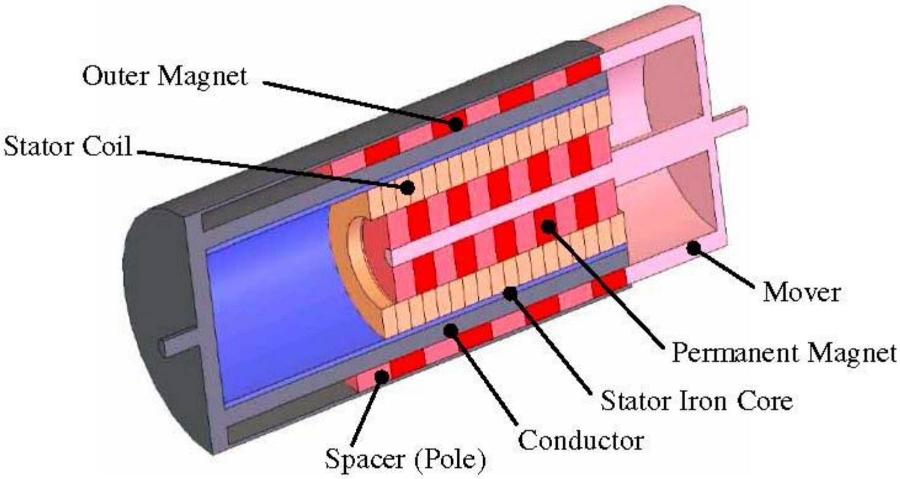

Figure 1.5 Schematic view of a hybrid EM damper

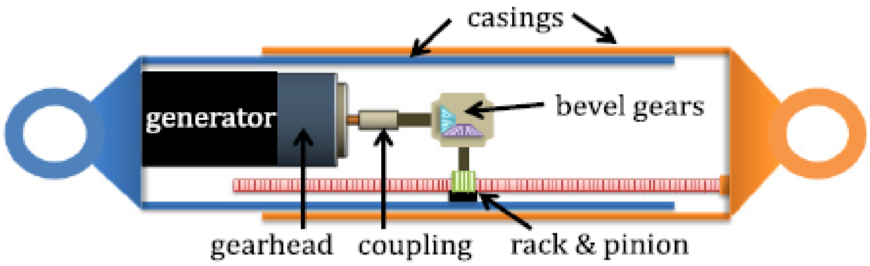

Figure 1.6 EM shock absorber using a rack-pinion mechanism

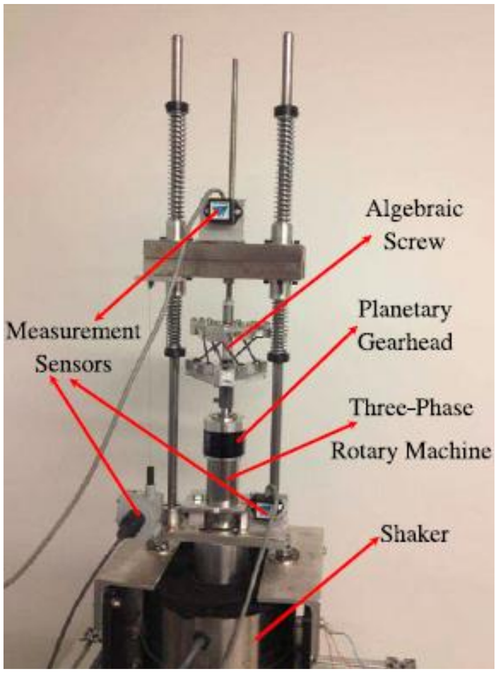

Figure 1.7 EM suspension using an algebraic screw mechanism

Besides EM-based regenerative dampers, many scholars have studied self-powered MR dampers in recent decades. (Wang, Chen, & Spencer Jr, 2009) proposed a MR damper system with a rack-pinion mechanism and linear permanent magnet DC generator. (Choi & Wereley, 2009) designed an energy harvesting device consisting of a stator and a permanent magnet added to a MR damper. (Kim, Jung, & Koo, 2010) presented a smart MR damping system employing an EM induction system with the aim of generating electrical energy to power the damper. (Sapiński, 2010, 2011) developed a vibration power generator composed of permanent magnets and a foil-wound coil that could harvest and apply the energy to vary the damping characteristics of the attached MR damper. (Chen & Liao, 2012) proposed a MR damper prototype that integrated self-sensing ability and self-contained power generation within a single device.

So far, the previous works intended to explore the possibility of power recovery from suspension systems, but lacked a systematic method to actively tune the system parameters to achieve the optimum of either dynamic control or power recovery requirements. Therefore, developing an analytical solution to optimize system performance metrics is a key element in the design of effective energy harvesting suspension systems.

1.3. Optimal Design of Suspension Systems

The optimization process is the coordination of the relationships between parameters, performance indices, and design constraints. In practical applications, most optimization problems are multi-objective in nature. Therefore, the best solution usually does not exist, and the decision to adopt the better solution may be subjective. Hence there is not a universally accepted method for every application. To date, there are various approaches to the optimization problems of suspension systems. (Tamboli & Joshi, 1999) analyzed a half-car model and suggested an optimization technique for minimizing the root-mean-square (RMS) acceleration response from the ride comfort point of view. The analysis is based on an exponential-type power spectral density (PSD) curve approximated to highway-type road conditions. (Gobbi & Mastinu, 2001) introduced an optimization method based on multi-objective programming (MOP) and monotonicity analysis, subjected to the excitation coming from road irregularities. The derivation of the analytical formula became possible by exploiting MOP, which represented a theoretical way of selecting parameters featuring the best compromise among conflicting performance indices. (Verros, Natsiavas, & Papadimitriou, 2005) proposed a methodology for optimizing the suspension damping and stiffness parameters of a nonlinear quarter-car model. The random road excitation was simulated by a series of sinusoidal inputs, and the cost function was a weighted sum of three performance indices. By selecting different sets of weights, the corresponding optimal parameters could be obtained. (Georgiou, Verros, & Natsiavas, 2007) employed multi-objective optimization in the design of passive and semi-active suspension systems, based on a 2-DOF quarter-car model moving over rough roads. (Jazar, Narimani, Golnaraghi, & Swanson, 2003) proposed an optimization method for a 1-DOF quarter-car model by minimizing the cost functions that were the RMS of absolute acceleration transmissibility and relative displacement transmissibility. As indicated in Figure 1.8, the RMS values were used to create the design charts and the optimal values of the parameters that could be selected regarding the minimization of acceleration transmissibility with respect to relative displacement transmissibility. Later, (Jazar, Alkhatib, & Golnaraghi, 2006) used a 2-DOF quarter-car model to derive the symbolical formula of the RMS of frequency responses and the corresponding design curves. The relationship between the parameters and selection criteria was presented in terms of the design curves. (Arzanpour, Eslaminasab, Shubert, Narimani, & Golnaraghi, 2006) extended the RMS optimization method from the frequency domain to the time domain. Unlike the steady-state response that was concerned with the frequency domain, the transient response was concerned with the time domain. The results showed the optimal parameters in the two domains are not the same, so there is no exclusively optimal value for both transient and steady-state responses. (Eslaminasab, Arzanpour, & Golnaraghi, 2007) utilized similar RMS methods to design the optimal parameters for asymmetric passive dampers and also discussed the feasibility of the optimal design of semi-active dampers. RMS optimization techniques were proven to be useful in the suspension system design.

All the above works have been theoretically proven and verified by numerical simulations. However, lack of experimental verification casts doubt on their feasibility in practice. Furthermore, in these studies, only conventional suspension designs were considered; hence, above methods cannot be applied to a regenerative suspension system for optimization of energy harvesting performance. (Zuo & Zhang, 2013) investigated the relationships between power generation and road roughness, driving speed, and suspension parameters for their proposed regenerative suspension system; however, there no closed-form analytical solutions were derived, so the study is not generally applicable to other systems.

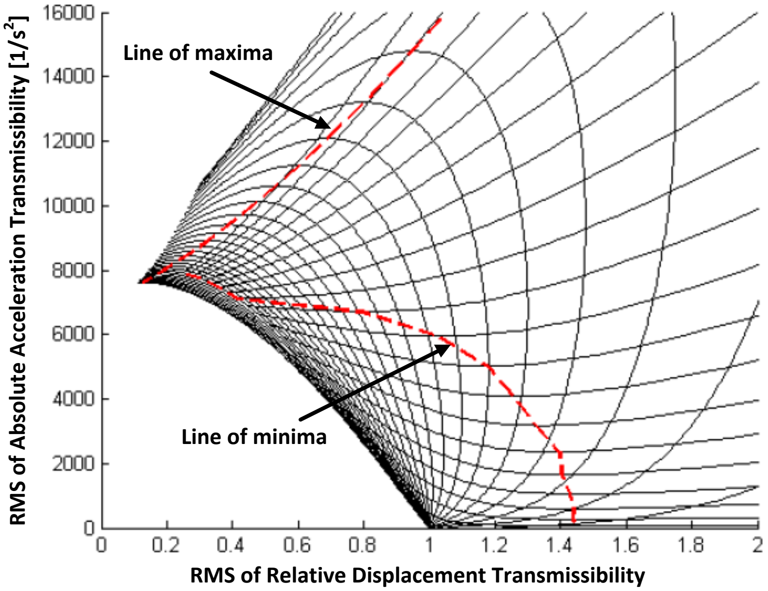

Figure 1.8 Root-mean-square (RMS) optimization design chart

1.4. Bandwidth Enhancement

In view of energy harvesting, the limited bandwidth of the linear resonant generator restricts effectiveness and becomes a big concern. A fundamental drawback of this kind of generator is that it must ensure that its natural frequency matches the main frequency of the input vibration. To overcome the disadvantage of the linear energy harvester, a number of strategies for the purpose of increasing operating frequency have been studied. Basically there are two strategies broadly investigated by researchers (Zhu, Tudor, & Beeby, 2010):

- Tuning the resonant frequency

(Cammarano, Burrow, Barton, Carrella, & Clare, 2010) proposed a tuning method for the resonant energy harvester, using a generalized electrical load. The operating frequency range was shown to be over three times greater with optimized load impedance compared to a normal resonant energy harvester. (Challa, Prasad, Shi, & Fisher, 2008) designed a vibration energy harvesting device with bidirectional resonance frequency tunability using a magnetic force technique, which enabled a $\pm 20\%$ extension of the unturned frequency region. The problem of tuning resonant frequency is that it is hard to realize when the excitation frequency is unknown or unpredictable, which is the case with random road excitation.

- Widening bandwidth

Widening the bandwidth eliminates the uncertainty of the excitation frequency, so it is more suitable to apply to the suspension system. (Burrow, Clare, Carrella, & Barton, 2008) added magnetic reluctance forces to the linear spring compliance to introduce a third-order nonlinearity, thus providing a wider bandwidth of operation. (Ramlan, Brennan, Mace, & Kovacic, 2010) investigated a nonlinear mechanism with hardening stiffness, which also introduced a cubic nonlinearity and had the effect of shifting the resonance frequency, so a greater bandwidth could be obtained. (Mann & Sims, 2009) proposed an energy harvesting device with magnetic restoring forces to levitate an oscillating center magnet. The system was able to be modeled with the Duffing equation under static and harmonic excitation, thus improving energy harvesting performance.

Besides the nonlinear techniques mentioned above, there are other sophisticated nonlinear methods currently implemented in the control and dynamical applications that can be utilized in bandwidth enhancement. (Nayfeh, Mook, & Marshall, 1973) investigated nonlinear couplings of different modes in ships and found that internal resonance (IR) led to energy transfer into the roll mode. (Anderson, Nayfeh, & Balachandran, 1996) studied on a flexible cantilever beam with widely separated natural frequencies, investigating the exchange of energy between high-frequency modes and a low-frequency mode due to quadratic nonlinear couplings. (Golnaraghi, 1991) exploited beat phenomena resulting from quadratic nonlinearities as a control technique for flexible structures. He designed a sliding mass-spring-dashpot mechanism as a vibration controller. When the IR condition was satisfied by tuning the linear spring, the energy of the plant was transferred and dissipated through the controller. (Tuer, Duquette, & Golnaraghi, 1993) and (Duquette, Tuer, & Golnaraghi, 1993) conducted theoretical and experimental studies on vibration suppression of a similar beam as (Golnaraghi, 1991) with improved performance, by means of a more dominant rotational IR controller.

All the researches discussed above were performed based on a coupling quadratic nonlinear phenomenon known as IR, which transfers energy from 1-DOF to the other in superharmonic or subharmonic resonance when the natural frequencies of two modes are commensurable or nearly commensurable, such as $\omega_2 = 2\omega_1$ or $\omega_1 = 2\omega_2$. The other nonlinear technique that can be utilized in bandwidth enhancement is parametric resonance, which can be described by Mathieu's equation. A similar energy-transferring phenomenon occurs in superharmonic or subharmonic resonance when the frequency of the parametric cyclic term is commensurable with the natural frequency of the system. (Oh, Nayfeh, & Mook, 2000) investigated the indirectly excited roll motion in ships and found the vessel could exhibit a large-amplitude roll motion because of the energy transferred from the pitch or heave motions, where the roll motion was not directly excited. (Ramakrishnan & Feeny, 2012) analyzed the dynamic behavior of a horizontal axis wind turbine blade rotation in steady operation and wind conditions, and modeled the system using a forced Mathieu equation with cubic nonlinearity, considering direct and parametric excitations.

1.5. Research Objectives and Thesis Outline

This research aims at introducing a novel regenerative suspension system that is capable of providing damping control and energy harvesting. The main objectives of this research include design and development of such a system, fabrication of a proof-of-concept prototype and its experimental verification, optimization of the system parameters design for the best control and power regeneration performance, and improvement of the system such as bandwidth enhancement and a self-powered control strategy. Specifically, the outline of this thesis is as follows:

In Chapter 1, a brief background of traditional vehicle suspension systems is introduced. A literature review of related researches on energy-regenerative suspension systems is discussed.

In Chapter 2, an energy-regenerative suspension system consisting of a DC machine, a ball screw mechanism, and an adjustable load resistor is developed, and mathematical modeling of such system is derived. A test-bed is established and experimental results are obtained and compared with numerical simulations to confirm the effectiveness of the system.

In Chapter 3, a systematic optimization method is presented to provide a graphical design guideline by selection of stiffness and damping coefficients to reach either best ride comfort or maximum energy harvesting. A bench experiment is carried out to experimentally verify the proposed technique.

In Chapter 4, a design optimization methodology is proposed for predicting and optimizing the performance of the suspension system to efficiently capture the vibrational energy induced by random road irregularities to maintain the passenger’s comfort. Closed-form analytical solutions of performance metrics are derived. An experimental test is implemented to confirm the theoretical analysis.

In Chapter 5, a bandwidth enhancement technique utilizing nonlinear stiffness for the linear suspension system is provided. Perturbation methods are applied to obtain approximate solutions of the nonlinear responses analytically. A piecewise spring system is developed to produce a cubic-like nonlinearity to the original suspension system. Experimental results are obtained to prove the improvement on the power regeneration performance.

In Chapter 6, a regenerative Skyhook control strategy is studied to supply active Skyhook control to the system using the self-regenerated power. An algorithm is designed to efficiently and safely control the system operating between energy regeneration mode and active control mode. Numerical simulations are performed to prove the theoretical work.

In Chapter 7, conclusions of the research are stated and future works are discussed.

1.6. Thesis Contributions

1. The mathematical modeling of the 1-DOF quarter-car system, the fabricated prototype and established test bench can be used in other similar applications for vibrational energy harvesting.
2. The design optimization methodologies can be easily implemented as guidelines for vehicle designers and applied in the real world. They have great potential for practical usage, not only in automotive areas but other aspects of vibration applications.
3. Three journal papers and several conference papers have been published based on the research in this thesis.

Chapter 2.

Development of an Energy-Regenerative Suspension System

2.1. System Description and Prototype Design

Regenerative shock absorbers were designed to replace traditional dampers to achieve the desired damping while harvesting energy. In general, there are two types of configurations of regenerative shock absorbers, that is, linear and rotary. The linear shock absorbers utilize the relative motion between the magnetic field and the coils to generate power. The rotary shock absorbers convert the linear motion to the rotary motion of a permanent magnetic DC generator, which has higher efficiency and is capable of generating more power. To this end, an energy-regenerative suspension system was designed and can be simplified as a 1-DOF quarter-car model, which is shown in Figure 2.1. The model comprises sprung mass, physical springs, and shock absorbers, consisting of a DC motor/generator, planetary gearbox, and a ball screw mechanism to convert the vertical motion between the sprung mass and base excitation to the rotary motion of the screw shaft. A load resistor was connected to the motor terminal that acted as a battery. The motor was able to provide different values of damping force by adjusting the value of the load resistor. Based on the system description, a proof-of-concept prototype was designed using SolidWorks 2012, as shown in Figure 2.2.

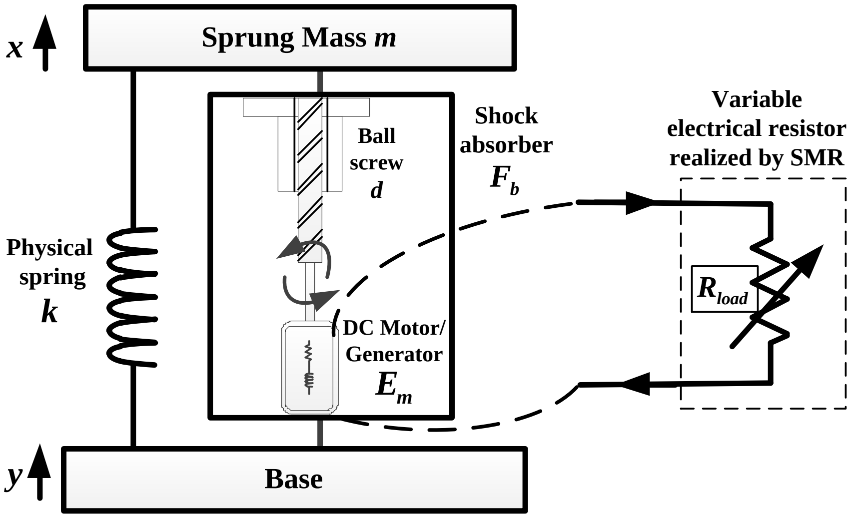

Figure 2.1 1-DOF model of the regenerative suspension system

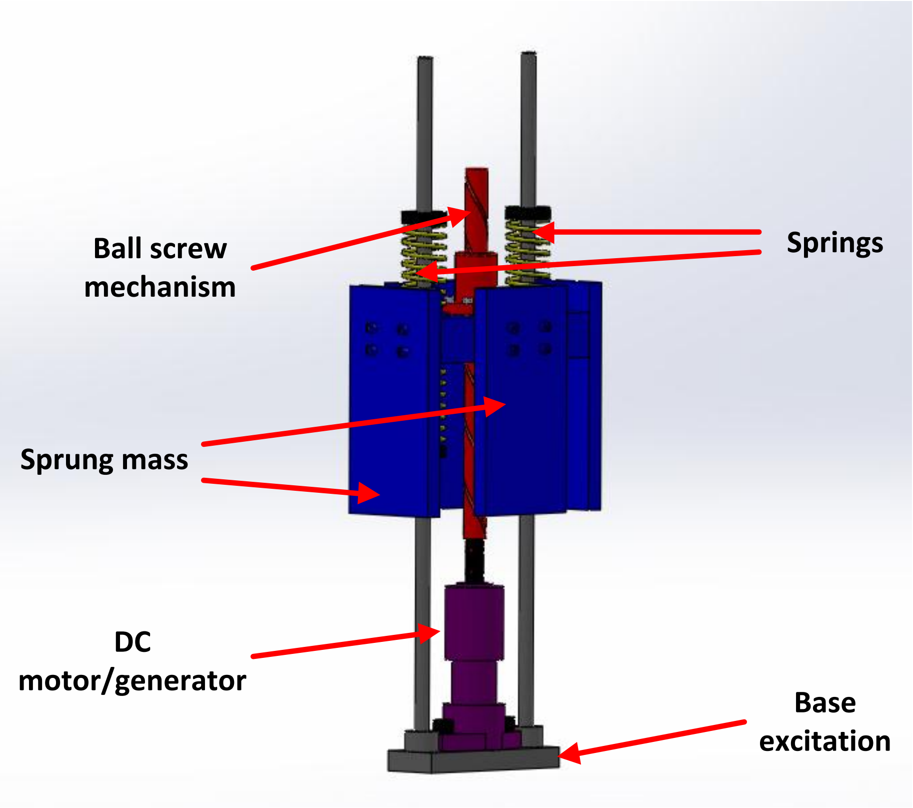

Figure 2.2 CAD prototype of the regenerative suspension system

2.2. Mathematical Modeling

The whole system shown in Figure 2.1 represents the dynamics of one wheel of the vehicle and a quarter of the suspended mass. It consists of elements in both mechanical and electrical domains. The mechanical domain is represented by a 1-DOF mass-spring-damping system, while the electrical domain includes a low-power switch-mode rectifier (SMR) connected to the terminal of the DC motor. The purpose of such power electronic circuit is not only to represent the dynamics of a variable physical resistor, but to harvest instantaneous power dissipated by the DC motor. The study on variable resistance synthesis through SMR was done by (Hsieh, Huang, Golnaraghi, & Moallem, 2014), and its operation and control are not covered by this thesis, so the details are not explained here.

2.2.1. DC Motor and Generator

Figure 2.3 depicts a model of the DC machine connected to the SMR in electrical domain. When the motor is used as a generator, the internal inductance is ignored in common like most previous investigations (Stephen, 2006).

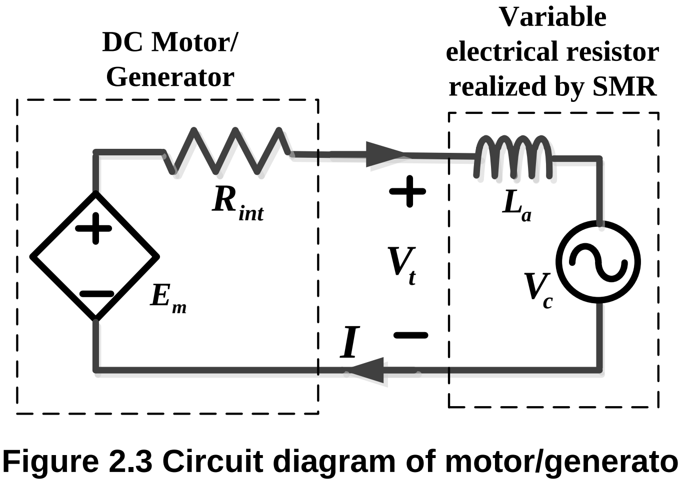

Figure 2.3 Circuit diagram of motor/generator

The back electromotive force (back-EMF) voltage was generated due to the rotation of the motor and can be defined as

$$E_m = k_e k_g \eta_g \dot{\theta} \tag{1}$$

where k_e is back-EMF coefficient, k_g and η_g are transmission ratio and efficiency of the gearbox, $\dot{\theta}$ is angular velocity of the motor gear shaft.

Simultaneously, the motor provides mechanical torque according to the current I passing through the load resistor R_{load}. Therefore, by controlling the current I through SMR, the torque generated by the motor can be adjusted accordingly. To ensure correct resistor synthesis, the expected current I is derived in terms of R_{load} as follows:

$$I = \frac{E_m}{R_{int} + R_{load}} = \frac{k_e k_g \eta_g}{R_{int} + R_{load}} \dot{\theta} \tag{2}$$

where R_{int} is the Internal resistance of DC motor. To guarantee that current I varies according to Eq. (2), the terminal voltage V_c is controlled in SMR based on

$$V_c = E_m - I R_{int} - L_a \frac{\mathrm{d}I}{\mathrm{d}t} \tag{3}$$

where L_a is the inductance in SMR. Therefore, the output torque of the motor is expressed in terms of the current as

$$\tau_i = k_t I = \frac{k_t k_e k_g \eta_g}{R_{int} + R_{load}} \dot{\theta} \tag{4}$$

2.2.2. Ball Screw Mechanism

A ball screw mechanism transforms an axial stroke into rotary motion and then induces the motor shaft to rotate dynamically. There are some assumptions in the following modeling procedure:

- Motor rotor and ball screw are assumed to be rigid.
- Backlash and torsion of the ball screw are not considered.

That is, the relationship between angular θ and stroke motion z in the transformation of the ball screw should be

$$\theta = z/(d\eta_b) \tag{5}$$

Where η_b is the efficiency of the ball screw, and

$$d = \frac{l}{2\pi} \tag{6}$$

The relationship between the ball screw and the DC motor is illustrated in Figure 2.4.

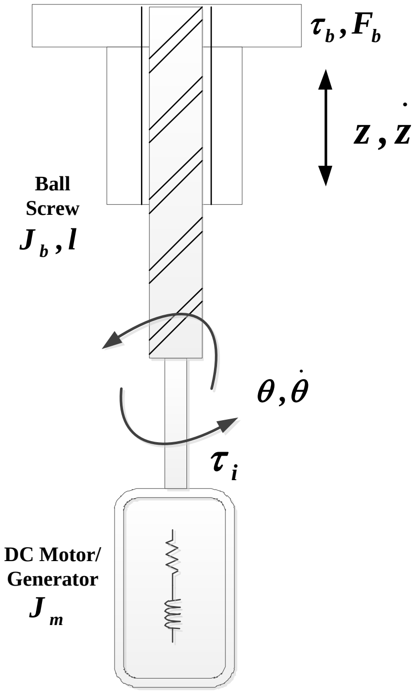

Figure 2.4 Dynamics of ball screw and DC motor

It should be noted that nonlinearities from the ball screw, such as backlash effect, were ignored since the ball screw used in this work was the pre-load type that reduces backlash influence significantly.

2.2.3. *Output Force of the Regenerative Damper*

The damper consisted of the DC machine with a gearbox and a ball screw mechanism. The gearbox amplified the rotation of the motor by k_g and diminishes the torque to the motor by k_g. Therefore, the equations of the rotor dynamics are as follows

$$\frac{\tau_b - (J_g + J_b)\ddot{\theta}}{k_g \eta_g} - \tau_i = J_m k_g \eta_g \ddot{\theta} \tag{7}$$

$$\tau_b = \frac{k_e k_t k_g^2 \eta_g^2}{R_{int} + R_{load}} \dot{\theta} + (J_m k_g^2 \eta_g^2 + J_g + J_b) \ddot{\theta} \tag{8}$$

where J_m, J_g, and J_b are the inertia of the motor, gearbox, and ball screw, respectively. k_t is the torque constant of the motor. $\ddot{\theta}$ is the angular acceleration of the motor gear shaft. τ_b and τ_i are output torque of the shock absorber and motor respectively.

According to the properties of the ball screw mechanism, the relationship between torque and force of the damper F_b is given by

$$\tau_b = d \eta_b F_b \tag{9}$$

Consequently, the equivalent output force of the damper is obtained as follows

$$F_b = \frac{k_e k_t k_g^2 \eta_g^2}{(R_{int} + R_{load}) d^2 \eta_b^2} \dot{z} + \frac{(J_m k_g^2 \eta_g^2 + J_g + J_b)}{d^2 \eta_b^2} \ddot{z} \tag{10}$$

2.2.4. Dynamics of the Quarter-Car Suspension System

The dynamic equation of the suspension system can be derived as

$$m(\ddot{x} - \ddot{y}) + k(x - y) + F_b = -m\ddot{y} \tag{11}$$

where the excitation is considered as $y = Y \sin \omega t$. x is the displacement of the sprung mass. m is the sprung mass. k is the spring constant. The wheel exhibits a low pass filter characteristic that smooths out disturbances due to road input. Substituting Eq. (10) into Eq. (11), the dynamic equation can be expressed as

$$\left(m+\frac{J_m k_g^2 \eta_g^2+J_g+J_b}{d^2 \eta_b^2}\right)\ddot{z}+\left(c_f+c\right)\dot{z}+kz=m\omega^2 Y \sin \omega t \tag{12}$$

where c_f is the coefficient of inherent viscous damping and

$$z=x-y \tag{13}$$

$$c=\frac{k_e k_t k_g^2 \eta_g^2}{(R_{int}+R_{load}) d^2 \eta_b^2} \tag{14}$$

Eq. (12) can be simplified as

$$m_{eq}\ddot{z}+c_{eq}\dot{z}+kz=m\omega^2 Y \sin \omega t \tag{15}$$

where

$$m_{eq}=m+\frac{J_m k_g^2 \eta_g^2+J_g+J_b}{d^2 \eta_b^2} \tag{16}$$

$$c_{eq}=c_f+c \tag{17}$$

2.3. Numerical Simulation and Experimental Test

An experimental test-bed was developed to provide verification of the proposed regenerative suspension system, as depicted in Figure 2.5. The system physically implemented a 1-DOF quarter-car system, consisting of a mass plate on bearings and four parallel springs. A Maxon DC motor (RE40-

218011) was used in the place of a traditional damper and was attached with a planetary gearhead (GP52C-223083). A THK precision-ground ball screw (KX-10) was connected to the DC motor for converting vertical movement to rotary motion. The accuracy grade of the ball screw is between C0 and C5,[1] and the travel distance error ranges from 3μm to 18μm per 100 mm. Since the test result of the suspension stroke does not exceed 12mm, the travel distance error is limited to under 2.25μm. A MTS Hydraulic Actuator (Series 248) was utilized as a shaker to provide base excitation to the suspension system. A dSPACE DS1103 system was used as the I/O interface to acquire the voltage signal, displacement signal, and acceleration signal, from the DC generator, a string potentiometer, and an accelerometer. Table 2.1 shows the parameter values of the experimental setup.

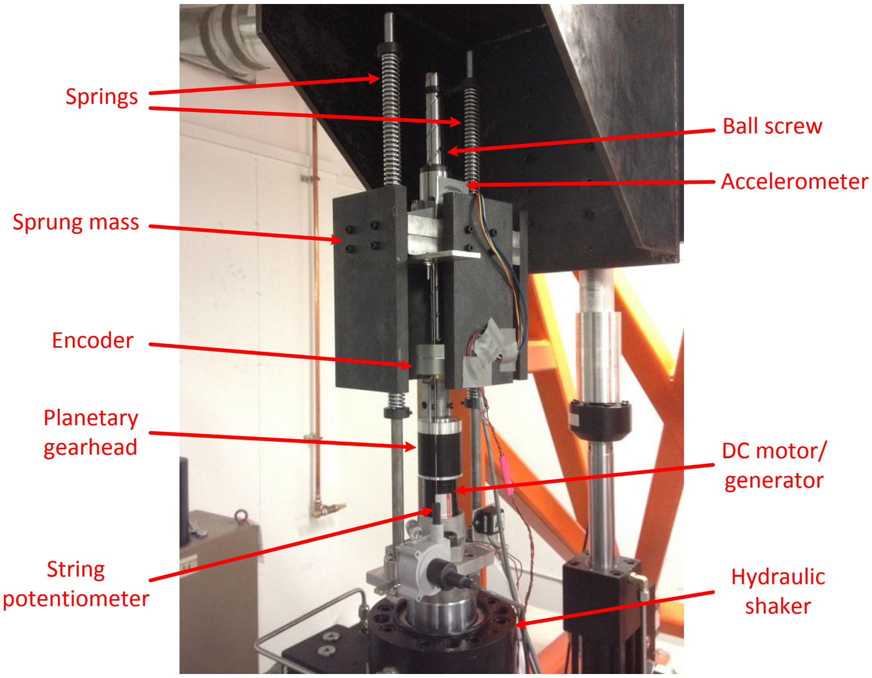

Figure 2.5 Experimental test setup for the regenerative suspension system

---

[1] According to the JIS standards (JIS B 1192-1997)

Table 2.1 Parameter values of the experimental setup

Parameter	Value
Sprung mass (m)	20 kg
Total spring constant (k)	25220 N/m
Softest spring constant used for optimization (k_{low})	10795 N/m
Hardest spring constant used for optimization (k_{high})	73320 N/m
Inherent viscous damping coefficient (c_f)	234.42 Ns/m
Rotor inertia of the DC motor (J_m)	120 gcm^2
Torque constant of the DC motor (k_t)	170 mNm/A
Back-EMF coefficient of the DC motor (k_e)	170 mV/rad/s
Internal resistance of the DC motor (R_{int})	10.2 Ω
Rotor inertia of the gearhead (J_g)	17.6 gcm^2
Gear ratio of the gearhead (k_g)	12:1
Efficiency of the gearhead (η_g)	83%
Rotor inertia of the ball screw (J_b)	1248 gcm^2
Lear ratio of the ball screw (l)	60 mm/r
Efficiency of the ball screw (η_b)	95%
Travel length of the ball screw	300mm

2.3.1. Equivalent Damping Ratio

The damping coefficient of the regenerative suspension system depends on the value of the load resistor. Therefore, the variable damping coefficient was realized by adjusting the load resistor according to Eq. (14). By changing the load resistance from 490 Ω to 10 Ω, the equivalent damping coefficient ranged from 304.1 Ns/m to 1959 Ns/m. Since the damping coefficient does not reflect the extent of the damping in the system, we used damping ratio to quantify it. Mathematically, the damping ratio can be described as

$$\zeta_{eq} = \frac{c_{eq}}{2\sqrt{km_{eq}}} \tag{18}$$

Based on Eq. (18), the value of the damping ratio was calculated and varied from 0.059 to 1.46. The different values of the load resistor and corresponding damping values are listed in Table 2.2, and their relationship is shown in Figure 2.6.

Table 2.2 Values of load resistor and equivalent damping ratio

Load Resistance (Ω)	490	250	120	100	80	60
Damping Coefficient (c_{eq})	304.1	368.3	502	550.5	620.6	730.7
Damping Ratio (ζ_{eq})	0.16	0.19	0.26	0.29	0.33	0.38
Load Resistance (Ω)	50	40	30	20	10	
Damping Coefficient (c_{eq})	813.1	928.4	1101	1387.9	1959	
Damping Ratio (ζ_{eq})	0.43	0.49	0.58	0.73	1.03	

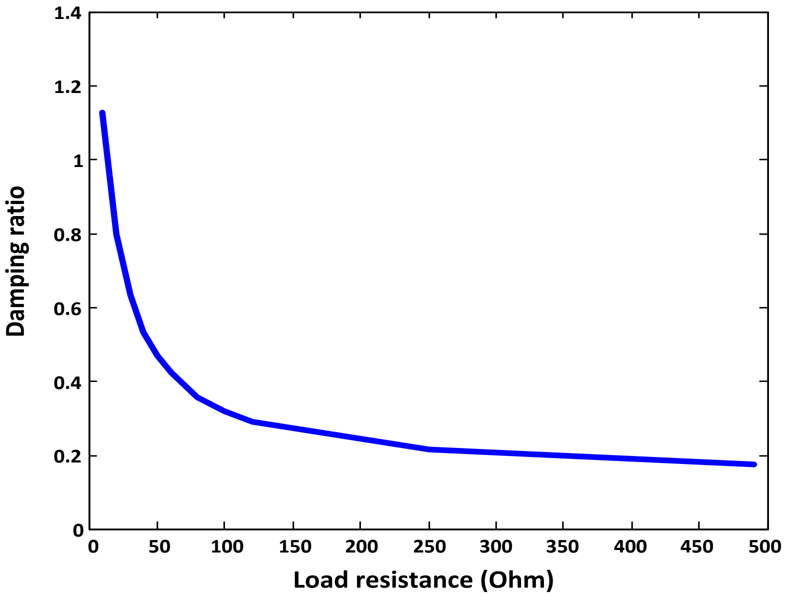

Figure 2.6 Damping ratios with different load resistances

2.3.2. *Time Responses Based on Harmonic Excitations*

The experiment was conducted by the base excitation with constant amplitude (10 mm) and certain frequencies (5 Hz and 8 Hz). The damping ratio was selected as 0.18 and realized by using the 490 Ω load resistor. In Figure 2.7, it can be seen that simulation results shown in the red curves match the experimental results indicated by the blue curves.

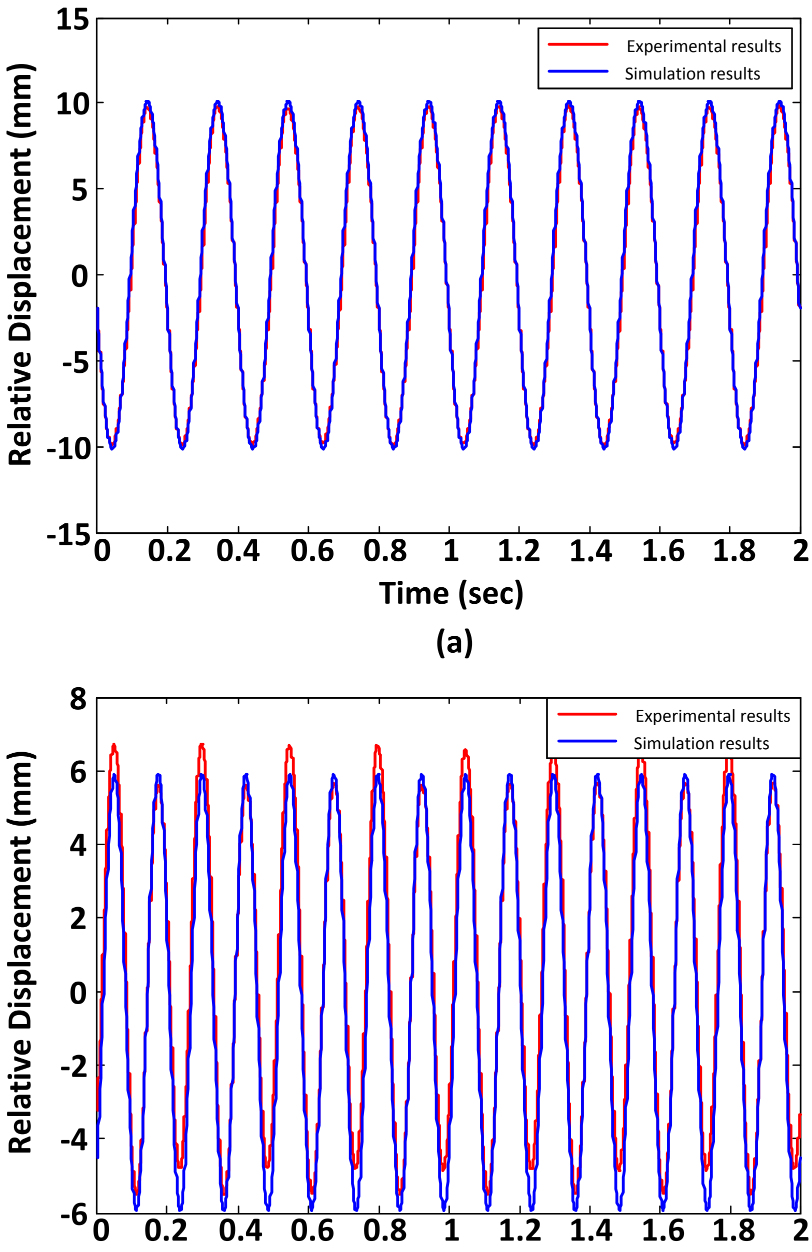

(a)

(b)

Figure 2.7 Time responses based on harmonic excitations in (a) 5 Hz and (b) 8 Hz

2.3.3. Frequency Responses Based on Harmonic Excitations

The performance of the experimental system was also examined by producing the frequency response over frequencies of 2 Hz to 9 Hz, with base excitation amplitude of 10 mm. Different values of load resistors and their corresponding damping ratio were chosen according to Table 2.2. Both numerical simulation results and experimental results of frequency responses of relative displacement between sprung mass and base excitation, sprung mass's absolute acceleration, and generated power are indicated in Figure 2.8. From the results, it can be seen that the simulation results well match the experimental results. Therefore, the dynamic model is able to provide an acceptable prediction of the real system's responses. The regenerative damper is able to provide the desired damping force as the traditional damper, by selecting the proper load resistance.

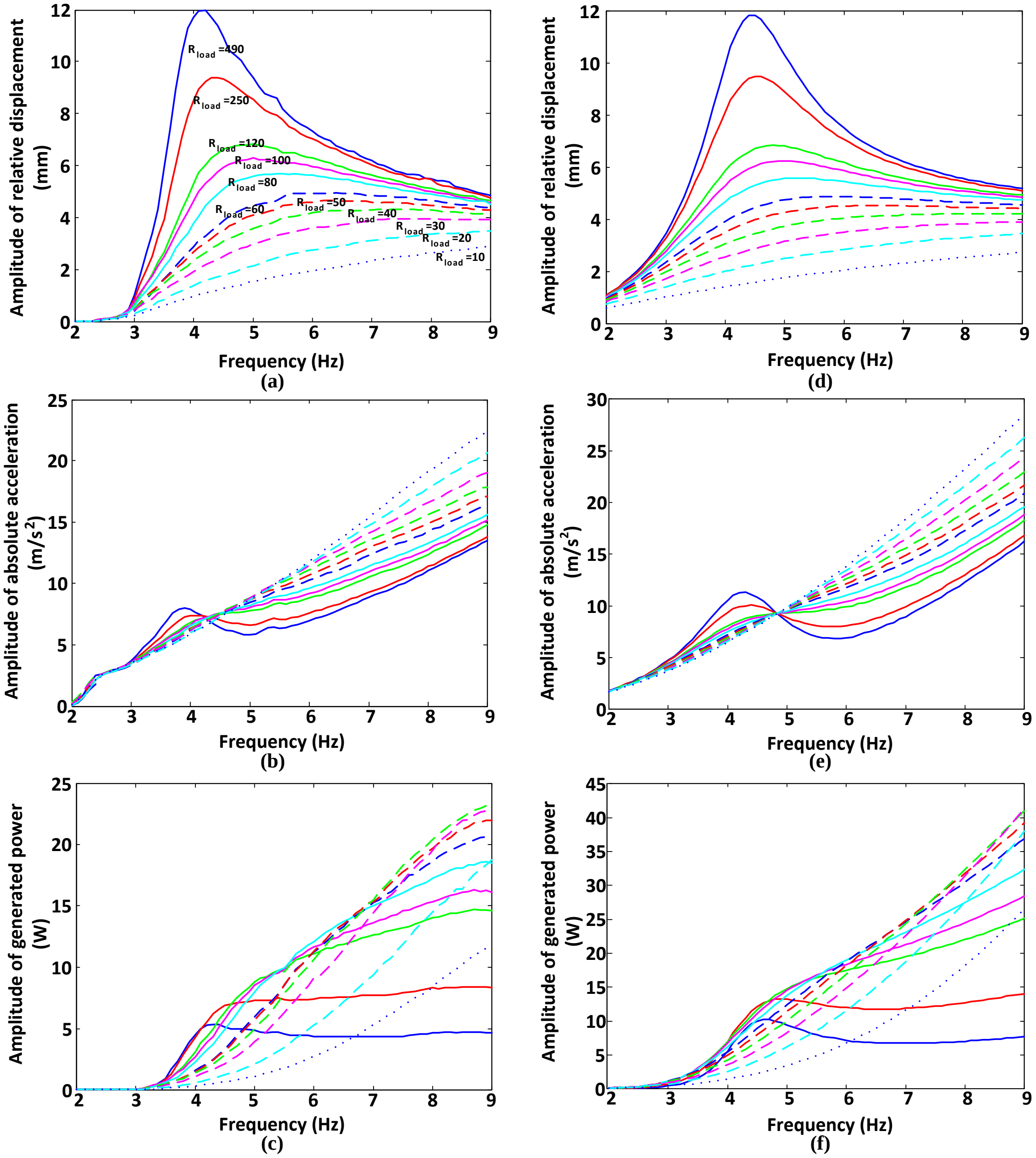

Figure 2.8 Frequency responses of relative displacement, absolute acceleration and generated power from experimental results (a-c) and simulation results (d-f)

2.3.4. Power Regeneration Efficiency

The total efficiency of power regeneration should be separated into mechanical efficiency and electrical efficiency. The energy into the system (E_{all}) is equal to the energy dissipated by viscous damping (E_f) plus the energy absorbed by the DC motor/generator (E_c) plus the kinetic and potential energies (E_k) that build up the mass-spring oscillation. Therefore, the mechanical efficiency can be derived by

$$\eta_{mech} = \frac{E_c}{E_{all}} = \frac{E_c}{E_f + E_c + E_k} \tag{19}$$

It can be seen that only energy absorbed by electrical damping contributes to power regeneration. Figure 2.9 shows the mechanical efficiency of the system with the load resistance of 30 Ω under excitation frequencies of 5 Hz to 9 Hz. From the results, the mechanical efficiency ranges from 31% to 41% and achieves the maximum around 8Hz. The viscous damping loss ratio is also calculated based on E_f/E_{all} and ranges from 6% to 8%. Therefore, 51% to 63% of the total input energy flows into the mass-spring oscillation.

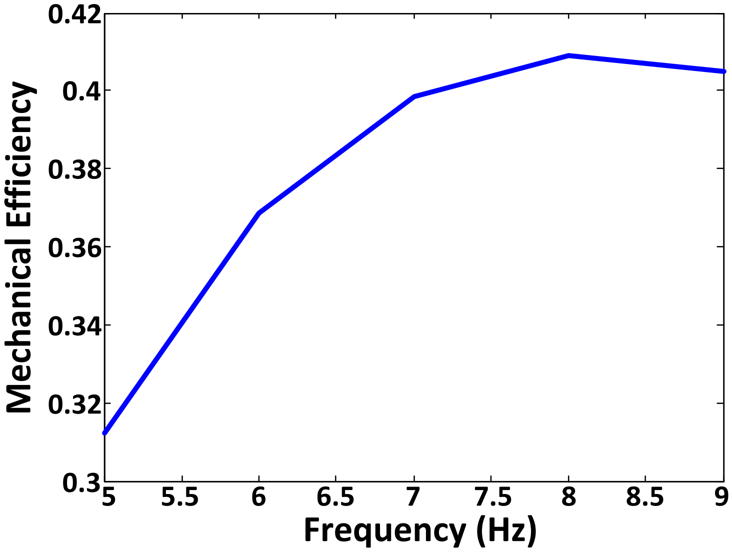

Figure 2.9 Mechanical efficiency of the system with 30 Ω load resistance for different excitation frequencies

The electrical efficiency refers to DC generator efficiency η_{gen} and SMR power conversion efficiency η_s, where η_{gen} and η_s can be defined below (Huang, Hsieh, Golnaraghi, & Moallem, 2015):

$$\eta_{gen} = \frac{R_{load}}{R_{int} + R_{load}} \tag{20}$$

$$\eta_s = \frac{\overline{P}_{DC}}{\overline{P}_e} = \frac{V_{out} \int_t^{t+T_i} i_{out}(t)dt}{\int_t^{t+T_i} V_{in}(t) i_{in}(t)dt} \tag{21}$$

where $\overline{P}_{DC}$ and $\overline{P}_e$ are the average charged battery power and harvestable power. Subsequently, the total power transfer efficiency in the electrical domain, defined as the product of DC generator efficiency and SMR power conversion efficiency, can be written as

$$\eta_{elec} = \eta_{gen} \cdot \eta_s \tag{22}$$

The experimental result of the electrical efficiency is presented in Figure 2.10, under the same conditions as for mechanical efficiency. The electrical efficiency ranges from 67% to 95%, and the highest efficiency is obtained around 7 Hz.

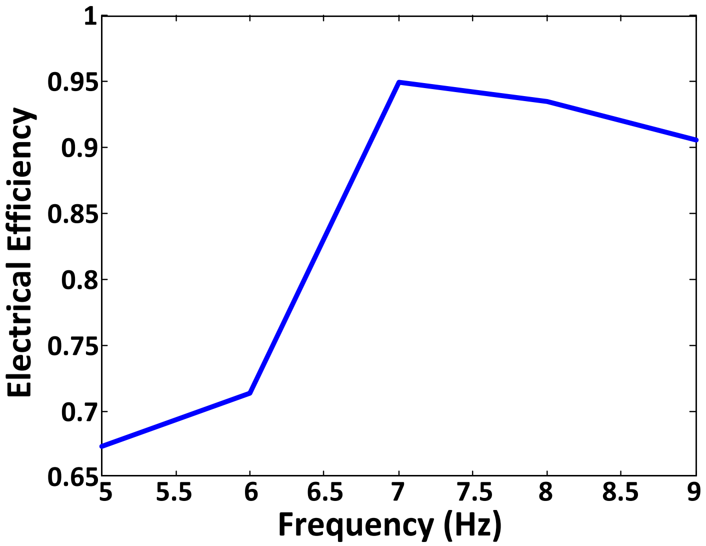

Figure 2.10 Electrical efficiency of the system with 30 Ω load resistance for different excitation frequencies

Overall, the total efficiency of power regeneration can be obtained as

$$\eta = \eta_{mech} \cdot \eta_{elec} \tag{23}$$

Figure 2.11 shows the total power regeneration efficiency of the system.

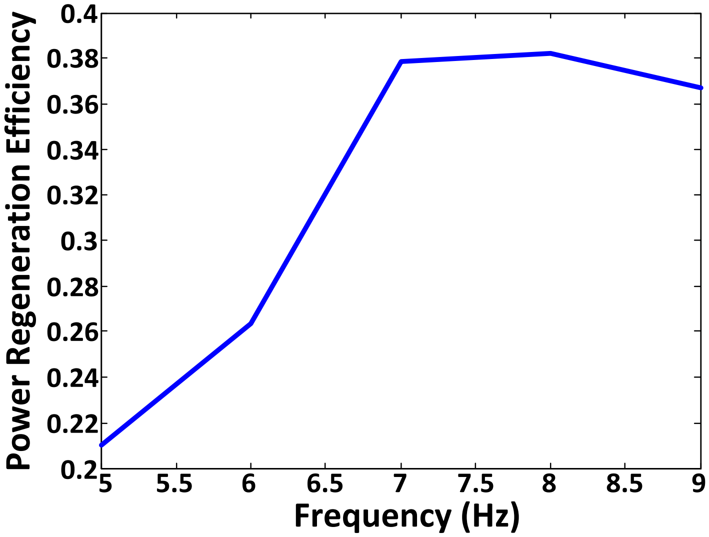

Figure 2.11 Power regeneration efficiency of the system

2.4. Conclusion

In order to improve the energy efficiency of electric vehicles, an energy-regenerative suspension system was proposed, and its mathematical modeling was represented. Compared to the linear motor, a DC rotary motor was used because of its low cost and low weight. In order to convert the translational motion between the sprung mass and excitation into the rotary motion of the motor's terminal, a precision-ground preload type ball screw mechanism was chosen as it has small travel error and nonlinearities, such as backlash, etc. A test-bed based on the dSPACE DS1103 data acquisition platform was established to perform experimental tests to verify the effectiveness of the proposed suspension system. The results indicated that the electrical damping was adjustable in terms of the load resistance, and showed a good agreement between experiments and simulations. Up to 40% of the input power is able to be captured by the proposed system.

For the purpose of finding the optimum solutions of suspension parameters, spring constant and damping coefficient, optimization studies based on two different types of excitations, harmonic and stochastic, are presented in Chapter 3 and Chapter 4, respectively.

Chapter 3.

Optimization of Energy-Regenerative Suspension System Under Harmonic Excitation

A systematic method for predicting and optimizing the performance of an energy-regenerative suspension system to efficiently capture the vibratory energy induced by road irregularities is presented. The optimization of a vehicle's ride comfort and power regeneration performance is realized by selecting the optimized spring constant and actively tuning the damping coefficient. The method provides a graphical guideline for the selection of system parameters aimed at either best ride comfort or maximum energy harvesting. A design chart is created according to the optimization rule, and used to choose the optimal spring constant and real-time damping switch of suspension systems, based on system performance indices as introduced in Section 2.3. A test-bed is utilized to experimentally verify the effectiveness of the proposed technique. The results indicate that the analytical and simulation results concerning the optimal values for dynamic control and power regeneration match the experimental results.

3.1. System Performance Indices

3.1.1. Ride Comfort – Absolute Acceleration Transmissibility

For evaluation of the suspension system's ride comfort performance, the transmissibility of absolute acceleration of the sprung mass is defined as follows:

$$a = \left|\frac{\ddot{X}}{Y}\right| = \frac{\frac{m}{m_{eq}}\omega^2\sqrt{k^2 + \left(c_f + c\right)^2\omega^2}}{\sqrt{\left(k - \omega^2 m_{eq}\right)^2 + \left(c_f + c\right)^2\omega^2}} \tag{24}$$

The ride comfort of the suspension system across the operational frequency range of road excitation was determined by calculating the RMS of the absolute acceleration transmissibility. For an operational range from ω_{low} to ω_{high}, the RMS value can be calculated as follows:

$$RMS_a = \sqrt{\frac{1}{\omega_{high} - \omega_{low}}\int_{\omega_{low}}^{\omega_{high}} a^2 d\omega} \tag{25}$$

To create an optimization chart in the next chapter, the normalized value of RMS_a was derived by

$$\overline{RMS_a}(i) = \frac{RMS_a(i) - \min(RMS_a)}{\max(RMS_a) - \min(RMS_a)} \tag{26}$$

where $RMS_a = (RMS_a(1), \dots, RMS_a(i), \dots, RMS_a(n))$ and $\overline{RMS_a}(i)$ is the i^{th} normalized data of RMS_a.

3.1.2. *Energy Harvesting – Power Generation Transmissibility*

In the design of an energy harvesting suspension system, the power generated from vibration is distributed to three areas: mechanical dissipation, electrical loss, and power feeding the electrical load. To capture useful power, the amount delivered to the electrical load needs to be maximized. The total current passing through the electrical load and the motor's internal resistor can be obtained as

$$I = \frac{k_e k_g \eta_g}{(R_{int} + R_{load}) d \eta_b} \dot{z} \tag{27}$$

The instantaneous electrical power generated by the damper is a function of the relative speed of the system, which is

$$P_{inst} = I^2 R_{load} = \frac{{k_e}^2 {k_g}^2 \eta_g^2 R_{load}}{(R_{int} + R_{load})^2 d^2 \eta_b^2} \dot{z}^2 = \frac{R_{load}}{(R_{int} + R_{load})} c \dot{z}^2 \tag{28}$$

From Eq. (14) we can get

$$R_{load} = \frac{k_e k_t {k_g}^2 \eta_g^2}{c d^2 \eta_b^2} - R_{int} \tag{29}$$

Substituting Eq. (29) into (28), we obtain

$$P_{inst} = \left(c - \frac{c^2 d^2 \eta_b^2 R_{int}}{k_e k_t {k_g}^2 \eta_g^2} \right) \cdot \dot{z}^2 \tag{30}$$

Considering the period of the cycle as $T = \frac{2\pi}{\omega}$, the average power flow per cycle is calculated as follows (Stephen, 2006):

$$P_{avg} = \frac{1}{T} \int_0^{\frac{2\pi}{\omega}} P_{inst} dt = \frac{1}{2} \left(c - \frac{c^2 d^2 \eta_b^2 R_{int}}{k_e k_t {k_g}^2 \eta_g^2} \right) |\dot{z}|^2 \tag{31}$$

which is related to the square of the amplitude of relative velocity. Similar to Eq. (24), the relative velocity transmissibility can be obtained as follows:

$$v = \left|\frac{\dot{Z}}{Y}\right| = \frac{m\omega^3}{\sqrt{\left(k - \omega^2 m_{eq}\right)^2 + \left(c_f + c\right)^2 \omega^2}} \tag{32}$$

Similarly, the power generation transmissibility can be built as

$$\begin{aligned} p = \left|\frac{P_{avg}}{Y^2}\right| &= \frac{1}{2}\left(c - \frac{c^2 d^2 \eta_b^2 R_{int}}{k_e k_t {k_g}^2 \eta_g^2}\right)\left|\frac{\dot{Z}}{Y}\right|^2 \\ &= \frac{\left(c - \frac{c^2 d^2 \eta_b^2 R_{int}}{k_e k_t {k_g}^2 \eta_g^2}\right) m^2 \omega^6}{2\left[\left(k - \omega^2 m_{eq}\right)^2 + \left(c_f + c\right)^2 \omega^2\right]} \end{aligned} \tag{33}$$

To evaluate the generated power across the operational frequency range, the average of generated power transmissibility according to Eq. (25) can be calculated as follows:

$$AVG_p = \frac{1}{\omega_{high} - \omega_{low}} \int_{\omega_{low}}^{\omega_{high}} p\, d\omega \tag{34}$$

Similar to Eq. (26), AVG_p is normalized between 0 and 1 for the optimization analysis and expressed as

$$\overline{AVG_p}(i) = \frac{AVG_p(i) - \min(AVG_p)}{\max\left(AVG_p\right) - \min(AVG_p)} \tag{35}$$

where $AVG_p = \left(AVG_p(1), \dots, AVG_p(i), \dots, AVG_p(n)\right)$ and $\overline{AVG_p}(i)$ is the i^{th} normalized data of AVG_p.

3.2. Problem Definition

From Eq. (24) and (33), the RMS of absolute acceleration transmissibility and the average of power generation transmissibility are functions of spring constant k and electrical damping c. Hence, an optimization method was proposed to determine the value of (k, c) for best ride comfort or energy harvesting, by taking RMS_a and AVG_p as the objective functions, respectively. The optimization rule is defined as

$$\begin{aligned} & \underset{w.r.t.\ \ (k,c)}{\min} \ RMS_a(k,c) \\ & \underset{w.r.t.\ \ (k,c)}{\max} \ AVG_p(k,c) \\ & S.t. \quad \omega_{low} \leq \omega \leq \omega_{high} \\ & \qquad\ \ k_{low} \leq k \leq k_{high} \\ & \qquad\ \ c_{low} \leq c \leq c_{high} \\ & \qquad\ \ \mathrm{MAX}(|\lambda|) \leq Bounce_{limit} \end{aligned} \tag{36}$$

where

$$\lambda = \left|\frac{Z}{Y}\right| = \frac{m\omega^2}{\sqrt{\left(k - \omega^2 m_{eq}\right)^2 + \left(c_f + c\right)^2 \omega^2}} \tag{37}$$

The constraints of the optimization rule include the frequency range covered by the excitation, physical limitation of the spring, the limited range of the adjustable damping that can be applied by the DC motor, and the allowable bounce of the suspension (i.e., the maximum relative displacement transmissibility).

3.3. Optimization Procedure

3.3.1. Flowchart of the Optimization Procedure

A flowchart of the proposed optimization procedures is shown in Figure 3.1.

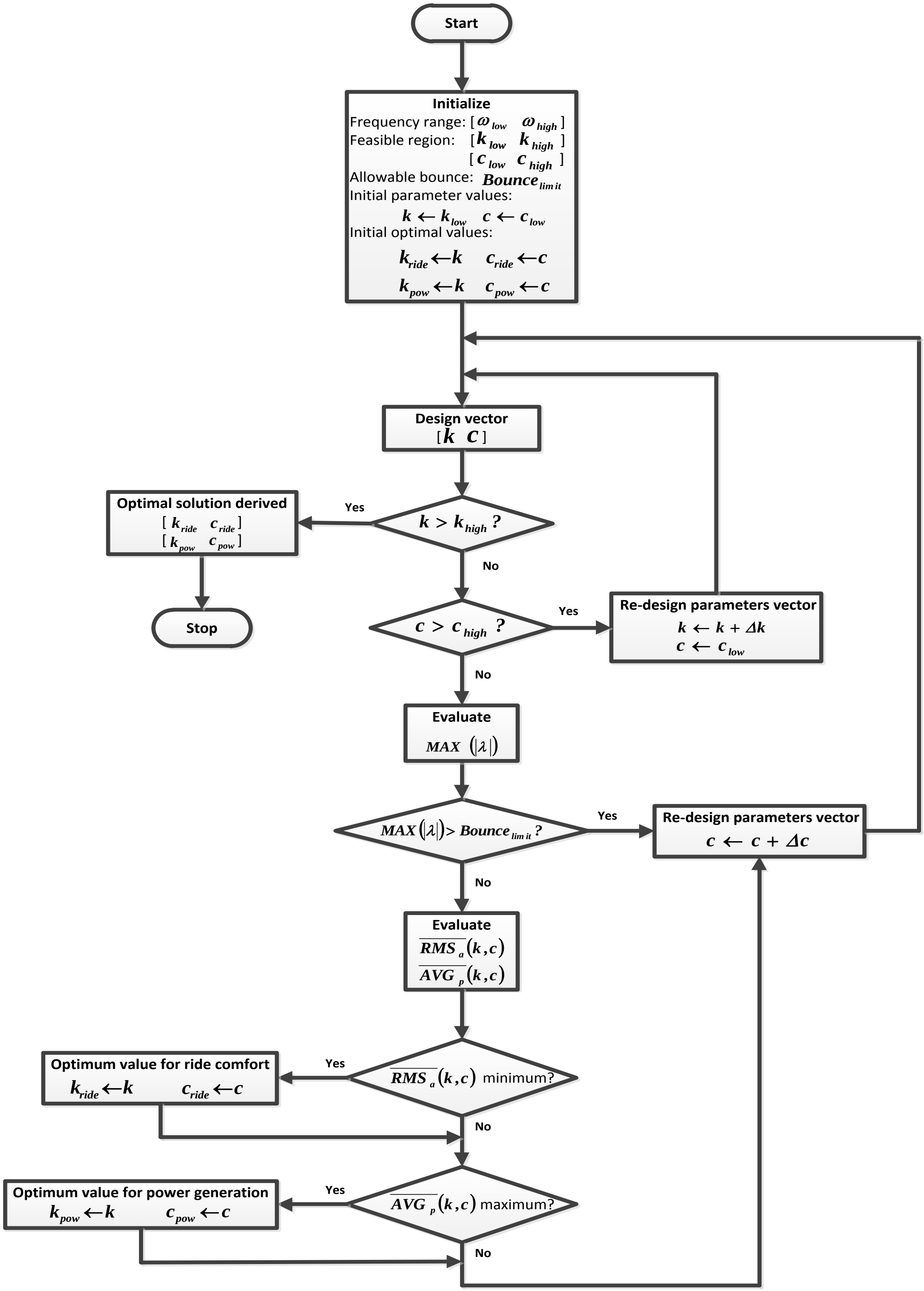

Figure 3.1 Flowchart of the optimization procedure

3.3.2. *Optimization Design Chart*

An optimization design chart was created by defining $\overline{RMS_a}$ and $\overline{AVG_p}$ as the Cartesian coordinates, using k and c as parameters. As illustrated in Figure 3.2, each solid curve indicates the values of $(\overline{RMS_a}, \overline{AVG_p})$ in terms of a certain value of k and different values of c; each dashed curve indicates the values of $(\overline{RMS_a}, \overline{AVG_p})$ in terms of a certain value of c and different values of k. By overlapping the solid and dotted curves, a grid figure was plotted where each intersection on the grid corresponds to a certain pair of (k, c), which uniquely determines a value of $(\overline{RMS_a}, \overline{AVG_p})$. The contour lines of the suspension bounce were drawn in colors, with an interval of 0.2. In this case, we supposed the road to be approximated as sinusoidal in cross section and the wavelength to be 3 m; a vehicle's speed from 20 km/h to 100 km/h determined the frequency of the base excitation, which ranges from 2 Hz to 9 Hz. $Bounce_{limit} = 2$ means the maximum damper play must be less than twice the excitation amplitude, which may vary due to different situations. Therefore, a convex feasible region of the optimization was produced by the constraints, which are shown in the shadow. Therefore, the design chart allows prediction of the system's performance based on any selection of (k, c). In practice, each type of vehicle presents a unique parameter distribution grid as in Figure 3.2. But the method is universal and applicable to the optimal design of all vehicle models (Huang, Hsieh, Golnaraghi, & Moallem, 2015).

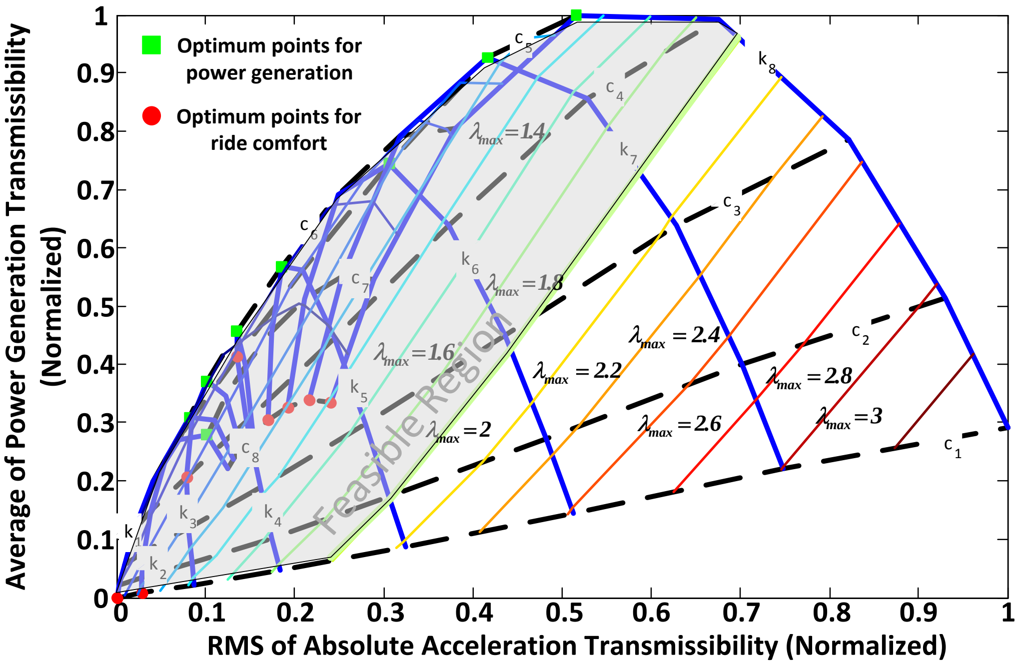

Figure 3.2 Contour curves for functions $\overline{RMS_a}$ and $\overline{AVG_p}$ in terms of (k, c), and optimization points for ride comfort and power generation

3.3.3. *Global Optimization*

Referring to Figure 3.2, the global optimum points for ride comfort and power generation performance can be found where $\overline{RMS_a}(k_1, c_1) = 0$ and $\overline{AVG_p}(k_8, c_5) = 1$. From the results, it can be seen that soft spring (k_1) and soft damping (c_1) provide the best ride comfort but the minimum power generation; hard spring (k_8) and moderate damping (c_5) lead to the best power generation and medium ride comfort. Global optimization provides a guideline for pre-setting the suspension parameters in terms of the performance requirements.

3.3.4. *Local Optimization*

For the present, the suspension parameters cannot be tuned when they are pre-set. In this work, an electronic circuit was developed to provide an adjustable damping coefficient in real time that could improve the suspension's performance. As a result, the local optimization is meaningful in guiding the on-line damping switch under different conditions. For each spring constant $(k_i,\ i = 1, \ldots, 8)$ selected, the local minima for ride comfort with respect to the damping coefficient (c) can be found where

$$\frac{\partial RMS_a(k_i, c)}{\partial c} = 0 \qquad \frac{\partial^2 RMS_a(k_i, c)}{\partial c^2} > 0 \tag{38}$$

Similarly, the local optimization for power generation performance is found where the maxima exist:

$$\frac{\partial AVG_p(k_i, c)}{\partial c} = 0 \qquad \frac{\partial^2 AVG_p(k_i, c)}{\partial c^2} < 0 \tag{39}$$

In Figure 3.3, the local optimization for ride comfort indicates that for the higher spring constants, the optimum damping coefficient is on the upper boundary, and for the lower spring constants, the optimum damping coefficient shifts to the lower boundary. In Figure 3.4, the local optimization for power generation indicates that for the higher spring constants, the optimum damping coefficient is lower, and for the lower spring constants, the optimum damping coefficient becomes higher.

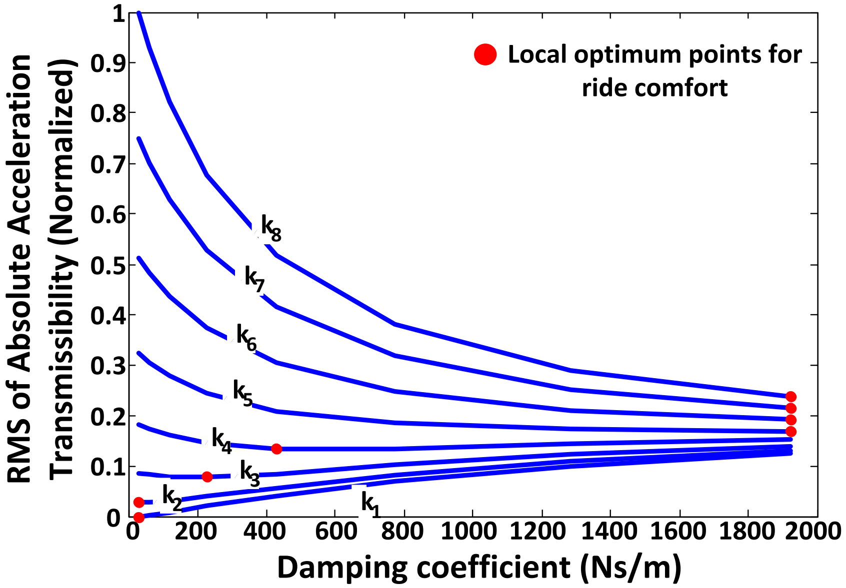

Figure 3.3 Local optimization for ride comfort performance versus damping coefficient for various spring constants

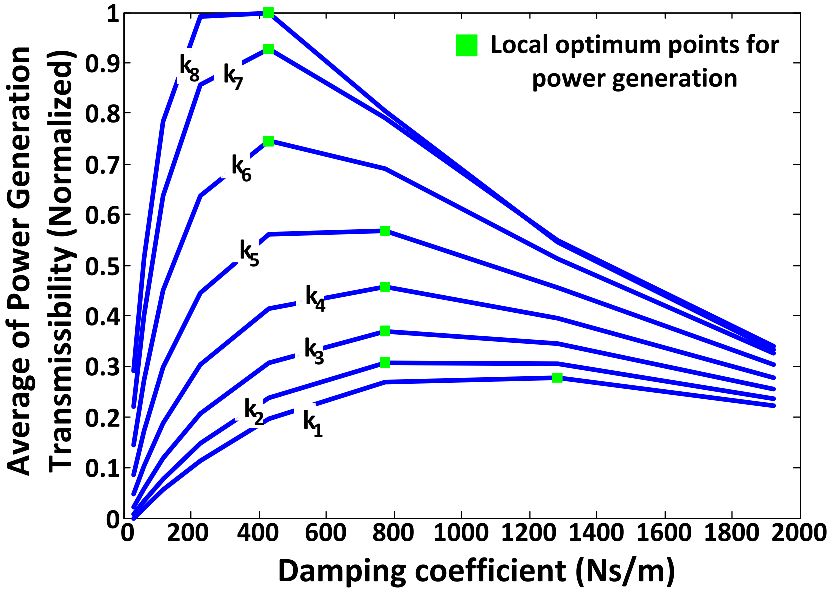

Figure 3.4 Local optimization for power generation performance versus damping coefficient for various spring constants

3.4. Simulation and Experimental Results

To verify the proposed optimization method, an experimental test was conducted using the developed regenerative suspension system. By producing the frequency responses over frequencies of 2 Hz to 9 Hz with base excitation amplitude of 10 mm, the curves of RMS of absolute acceleration transmissibility and average of power generation transmissibility with respect to the damping coefficient were built and plotted in Figure 3.5 and Figure 3.6. The parameters used for simulation were the same as shown in Table 2.1 and Table 2.2. All the results were normalized between 0 and 1 according to Eq. (26) and (35) for comparison between simulation and experimental results. Referring to Figure 3.5, optimum ride comfort performance exists at the lower boundary, where $c = 69.6\ Ns/m\ (R_{load} = 490\ \Omega)$. The results match the guidelines for optimization design of a suspension with a soft spring, which is detailed in Section 3.3.3 and 3.3.4. Also, referring to Figure 3.6, both simulation and experimental results denote that there is an optimum point at $c = 693.9\ Ns/m\ (R_{load} = 40\ \Omega)$, where maximum energy harvesting is achieved. Hence an important observation is that the maximum power can be generated when the damping is neither highest nor lowest. The absolute values of the performance indices for $R_{load} = 490\ \Omega, 60\ \Omega, 40\ \Omega, 10\ \Omega$ are listed in Table 3.1. The minimum and maximum values are depicted in bold.

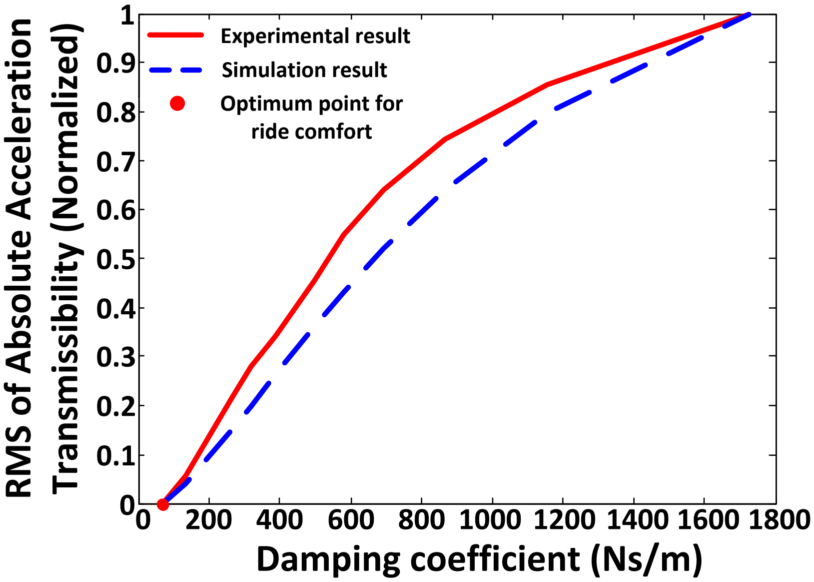

Figure 3.5 RMS of absolute acceleration transmissibility versus damping coefficient

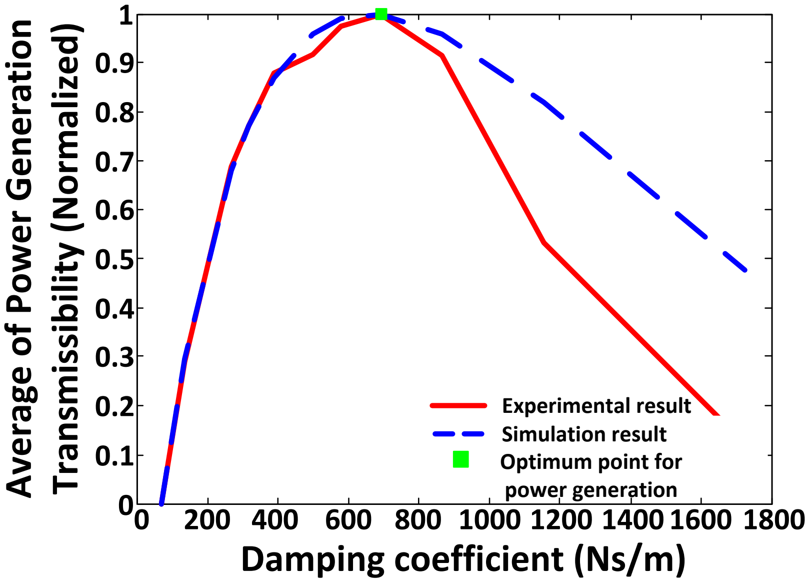

Figure 3.6 Average of power generation transmissibility versus damping coefficient

Table 3.1 Experimental results of performance indices for different load resistances

Load Resistance	RMS of Relative Displacement (mm)	RMS of Absolute Acceleration (m/s^2)	Average Generated Power (W)
$R_{load} = 490\ \Omega$	6.98	7.97	3.98
$R_{load} = 60\ \Omega$	3.92	10.08	11.73
$R_{load} = 40\ \Omega$	3.41	10.95	12.43
$R_{load} = 10\ \Omega$	1.85	12.62	5.03

3.5. Conclusion

In this chapter, an optimization strategy for finding optimum suspension parameters to achieve optimum ride comfort and power regeneration based on the harmonic excitation was presented. The strategy aimed at optimizing the suspension’s power regeneration or ride comfort performance by maximizing the average of the power generation transmissibility or minimizing the RMS of the absolute acceleration transmissibility. A graphical design rule was illustrated to demonstrate the existence of global and local optimum points. The experimental test was implemented, and results matched well with analytical results. In real world, the road excitation cannot be modeled as harmonic because it is stochastic in nature. Therefore, the optimization strategy is extended to the case of stochastic excitation, and is presented in the next Chapter.

Chapter 4.

Optimization of Energy-Regenerative Suspension System Under Stochastic Road Excitation

In this chapter, an analytical methodology for the optimal design of the system under stochastic road excitation is proposed. The optimization technique provides design guidelines for determining the stiffness and damping coefficients aimed at the optimal performance in terms of ride comfort and energy regeneration. The corresponding performance metrics are selected as RMS of sprung mass acceleration and expectation of generated power. The actual road roughness is considered as the stochastic excitation defined by ISO 8608 (International Organization for Standardization, 1995) standard road profiles and used in deriving the optimization method. A test-bed is utilized, and the experiments under different driving conditions are conducted to verify the effectiveness of the proposed method. The test results suggest that the analytical approach is credible in determining the optimality of the system's performance.

4.1. Problem Definition

4.1.1. Alternative Dynamic Equations of the Suspension System

To define cost functions for the optimization procedure, it is necessary to change the formula of the dynamic equation of the proposed regenerative suspension system. Eq. (12) can be alternatively expressed as

$$\begin{aligned}\left(m+\frac{J_m k_g^2\eta_g^2+J_g+J_a}{d^2\eta_b^2}\right)\ddot{x}+\left(c_f+\frac{k_e k_t k_g^2\eta_g^2}{(R_{\text{int}}+R_{\text{load}})d^2\eta_b^2}\right)\dot{x}+kx \\ =\frac{J_m k_g^2\eta_g^2+J_g+J_a}{d^2\eta_b^2}\ddot{y}+\left(c_f+\frac{k_e k_t k_g^2\eta_g^2}{(R_{\text{int}}+R_{\text{load}})d^2\eta_b^2}\right)\dot{y} \\ +ky\end{aligned} \tag{40}$$

or

$$\left(m+\frac{J_m k_g^2\eta_g^2+J_g+J_a}{d^2\eta_b^2}\right)\ddot{z}+\left(c_f+\frac{k_e k_t k_g^2\eta_g^2}{(R_{\text{int}}+R_{\text{load}})d^2\eta_b^2}\right)\dot{z}+kz=-m\ddot{y} \tag{41}$$

Eq. (40) and (41) can be simplified as

$$m_{\text{eq}}\ddot{x}+\left(c_f+c\right)\dot{x}+kx=m^{'}\ddot{y}+\left(c_f+c\right)\dot{y}+ky \tag{42}$$

and

$$m_{\text{eq}}\ddot{z}+\left(c_f+c\right)\dot{z}+kz=-m\ddot{y} \tag{43}$$

where

$$m'=\frac{J_m k_g^2\eta_g^2+J_g+J_a}{d^2\eta_b^2} \tag{44}$$

4.1.2. Standard Road Profile

The road profiles are characterized in terms of displacement PSD, which are considered as typical stochastic inputs. According to ISO 8608 (International Organization for Standardization, 1995), the displacement PSD in the spatial frequency can be described as

$$\begin{aligned} G_d(n) &= G_d(n_0)\left(\frac{n}{n_0}\right)^{-w} \\ &= G_0 n^{-w} \end{aligned} \tag{45}$$

where $G_0 = G_d(n_0)/n_0^{-w}$, $G_d(n_0)$ is road roughness coefficient, n_0 is the reference spatial frequency and $n_0 = 0.1$. Assuming a vehicle is driving at speed V, the temporal excitation frequency f and the spatial excitation frequency n have the relationship of $f = n \cdot V$, and similarly we have $\omega = 2\pi n \cdot V$. Therefore, the PSD of road excitation in the spatial frequency domain can be transferred to that in the temporal frequency domain by knowing that $G_d(n)\mathrm{d}n = G_d(\omega)\mathrm{d}\omega$, and can be described as

$$G_d(\omega) = \frac{2\pi G_0 V}{\omega^2} = \left|\frac{\sqrt{2\pi G_0 V}}{\mathrm{j}\omega}\right|^2 \tag{46}$$

4.1.3. Ground-Tire Interface

The ground-tire interface motion into the vehicle is used as the measure of the terrain elevation (Ashmore & Hodges, 1992), and the measurement is limited to the short wavelengths by the length of the tire footprint in contact with the terrain. Specifically, variations in the terrain elevation with a wavelength equal to or less than the length of the tire footprint cannot be measured, since the elevation seen by the tire at that wavelength is at the maximum attenuation.

Hence, the tire acts as a low-pass filter of the terrain elevation, with a full cut-off spatial frequency of $n_{fc} = W^{-1}\, m^{-1}$, where W is the length of the tire footprint. Suppose at vehicle speed V, the full cut-off temporal frequency should be around $f_{fc} = n_{fc}V = W^{-1}\, V$ Hz. Using a first-order low-pass filter to simulate the ground-tire interface, the cut-off frequency of the filter can be found at $f_c = 0.4 f_{fc}$ where -3 db attenuation happens. Therefore, the low-pass filter is derived to approximate the effects of the tire by

$$H_T(\mathrm{j}\omega) = \frac{\omega_c}{\mathrm{j}\omega + \omega_c} \tag{47}$$

where $\omega_c = 0.8\pi V W^{-1}$.

4.1.4. *The Ride Comfort Cost Function*

The optimization method was designed by deriving analytical formulas of performance indices (i.e., ride comfort and power regeneration) over the whole frequency range. The analytical formulas represent a theoretical way of selecting optimum parameters, such as stiffness and damping coefficients, and also create a design chart for visualizing the optimal values of the suspension parameters when a number of constraints and conflicting requirements on the system's performance have to be satisfied.

The ride comfort cost function is defined as RMS of absolute acceleration of the sprung mass. The transfer function between the excitation and absolute acceleration is given by Eq. (42)

$$H_a(\mathrm{j}\omega) = \frac{m'(\mathrm{j}\omega)^4 + \left(c_f + c\right)(\mathrm{j}\omega)^3 + k(\mathrm{j}\omega)^2}{m_{\mathrm{eq}}(\mathrm{j}\omega)^2 + \left(c_f + c\right)\mathrm{j}\omega + k} \tag{48}$$

According to ISO 2631-1 (International Organization for Standardization, 1997), a method evaluating the effect of exposure to vibration on humans is designed by weighting the RMS acceleration with human vibration-sensitivity curves, which can be approximated by a second-order quasi-least-square filter, whose transfer function is given by (Zuo & Nayfeh, 2003)

$$H_{\mathrm{asen}}(\mathrm{j}\omega) = \frac{86.51\mathrm{j}\omega + 546.1}{(\mathrm{j}\omega)^2 + 82.17\mathrm{j}\omega + 1892} \tag{49}$$

Therefore, the PSD of absolute acceleration can be obtained as

$$S_{aa} = |H_a(\mathrm{j}\omega)|^2 \cdot |H_{\mathrm{asen}}(\mathrm{j}\omega)|^2 \cdot |H_T(\mathrm{j}\omega)|^2 \cdot G_d(\omega) \tag{50}$$

and the expectation of absolute acceleration square is given by

$$E[a^2] = \frac{1}{2\pi}\int_{-\infty}^{\infty} S_{aa}\mathrm{d}\omega \tag{51}$$

The PSD of absolute acceleration, relative displacement, and relative velocity all can be expressed as a fraction with the polynomial of $\mathrm{j}\omega$ in both the numerator and denominator. According to (Newland, 2012), the analytical solutions exist for $E[a^2]$ if S_{aa} can be written as

$$S_{aa} = |H(\mathrm{j}\omega)|^2 \tag{52}$$

where

$$H(\mathrm{j}\omega)=\left\{\frac{B_0+(\mathrm{j}\omega)B_1+\cdots+(\mathrm{j}\omega)^{n-1}B_{n-1}}{A_0+(\mathrm{j}\omega)A_1+\cdots+(\mathrm{j}\omega)^{n}A_n}\right\} \tag{53}$$

Similar approaches have been utilized by a number of researchers in studies of optimization and energy harvesting from random vibrations, such as (Gobbi & Mastinu, 2001), (Halvorsen, 2008), (Adhikari, Friswell, & Inman, 2009), and (Zhao & Erturk, 2013). The PSD of absolute acceleration based on Eq. (50) can be obtained as

$$S_{aa}=\left|\frac{(\mathrm{j}\omega)B_1+(\mathrm{j}\omega)^2B_2+(\mathrm{j}\omega)^3B_3+(\mathrm{j}\omega)^4B_4}{A_0+(\mathrm{j}\omega)A_1+(\mathrm{j}\omega)^2A_2+(\mathrm{j}\omega)^3A_3+(\mathrm{j}\omega)^4A_4+(\mathrm{j}\omega)^5A_5}\right|^2 \cdot 2\pi G_0 V\omega_c^2 \tag{54}$$

where

$$\begin{aligned}
A_0&=1892\omega_c k\\
A_1&=1892\omega_c\left(c_f+c\right)+(82.17\omega_c+1892)k\\
A_2&=1892\omega_c m_{\mathrm{eq}}+(82.17\omega_c+1892)\left(c_f+c\right)+(\omega_c+82.17)k\\
A_3&=(82.17\omega_c+1892)m_{\mathrm{eq}}+(\omega_c+82.17)\left(c_f+c\right)+k\\
A_4&=(\omega_c+82.17)m_{\mathrm{eq}}+\left(c_f+c\right)\\
A_5&=m_{\mathrm{eq}}\\
B_1&=546.1k\\
B_2&=546.1\left(c_f+c\right)+86.51k\\
B_3&=546.1m^{'}+86.51\left(c_f+c\right)\\
B_4&=86.51m^{'}
\end{aligned} \tag{55}$$

and the analytical solutions of $E[a^2]$ can be derived and expressed as

$$\begin{aligned} E[a^2] = \pi G_0 V \omega_c^2 \{ & A_0 B_4^2 (A_0 A_3^2 + A_1^2 A_4 - A_0 A_1 A_5 - A_1 A_2 A_3) \\ & + A_0 A_5 (2B_2 B_4 - B_3^2)(A_1 A_2 - A_0 A_3) \\ & + A_0 A_5 (-2B_1 B_3 + B_2^2)(A_0 A_5 - A_1 A_4) \\ & + A_0 A_5 (-B_1^2)(A_3 A_4 - A_2 A_5)\} \\ & /\{A_0 A_5 (A_0^2 A_5^2 - 2A_0 A_1 A_4 A_5 - A_0 A_2 A_3 A_5 + A_1 A_2^2 A_5 \\ & + A_1^2 A_4^2 + A_0 A_3^2 A_4 - A_1 A_2 A_3 A_4)\} \end{aligned} \tag{56}$$

Therefore, the ride comfort cost function can be obtained as

$$RMS_a = \sqrt{E[a^2]} \tag{57}$$

4.1.5. *The Power Generation Cost Function*

From the energy harvesting perspective, the amount delivered to the electrical load needs to be maximized. Therefore, the expectation of the generated power is chosen as the power generation cost function. The total current passing through the electrical load can be obtained as

$$I = \frac{k_e k_g \eta_g}{(R_{\text{int}} + R_{\text{load}}) d \eta_b} \dot{z} \tag{58}$$

The instantaneous electrical power generated by the damper can be expressed as

$$P = I^2 R_{\text{load}} = \frac{{k_e}^2 {k_g}^2 \eta_g^2 R_{\text{load}}}{(R_{\text{int}} + R_{\text{load}})^2 d^2 \eta_b^2} \dot{z}^2 = \left(c - \frac{c^2 d^2 \eta_b^2 R_{\text{int}}}{k_e k_t {k_g}^2 \eta_g^2} \right) \cdot \dot{z}^2 \tag{59}$$

Thus the expectation of the generated power can be obtained by

$$E_P = \left(c - \frac{c^2 d^2 \eta_b^2 R_{\text{int}}}{k_e k_t {k_g}^2 \eta_g^2} \right) \cdot E[\dot{z}^2] \tag{60}$$

To obtain the analytical solutions of E_P, the expectation of relative velocity square $E[\dot{z}^2]$ should be given first. The transfer function between the excitation and relative velocity can be derived based on Eq. (43)

$$H_v(\mathrm{j}\omega) = \frac{-m(\mathrm{j}\omega)^3}{m_{\text{eq}}(\mathrm{j}\omega)^2 + \left(c_f + c\right)\mathrm{j}\omega + k} \tag{61}$$

Therefore, the PSD of relative velocity can be obtained as

$$S_{vv} = |H_v(\mathrm{j}\omega)|^2 \cdot |H_T(\mathrm{j}\omega)|^2 \cdot G_d(\omega) \tag{62}$$

and the expectation of relative velocity square is given by

$$E[\dot{z}^2] = \frac{1}{2\pi} \int_{-\infty}^{\infty} S_{vv} \mathrm{d}\omega \tag{63}$$

Similarly, the PSD of relative velocity is obtained as

$$S_{vv} = \left| \frac{(\mathrm{j}\omega)^2 D_2}{C_0 + (\mathrm{j}\omega) C_1 + (\mathrm{j}\omega)^2 C_2 + (\mathrm{j}\omega)^3 C_3} \right|^2 \cdot 2\pi G_0 V \omega_c^2 \tag{64}$$

and the expectation of relative velocity square is given by

$$E[\dot{z}^2] = \frac{\pi G_0 V \omega_c^2 \{-C_0 C_1 D_2^2\}}{C_0 C_3 (C_0 C_3 - C_1 C_2)} \tag{65}$$

where

$$\begin{aligned} C_0 &= \omega_c k \\ C_1 &= \omega_c \left(c_f + c\right) + k \\ C_2 &= \omega_c m_{\mathrm{eq}} + \left(c_f + c\right) \\ C_3 &= m_{\mathrm{eq}} \\ D_2 &= m \end{aligned} \tag{66}$$

Therefore, the power generation cost function is

$$E_P = \frac{\pi G_0 V \omega_c^2 C_0 C_1 D_2^2 \left(\frac{c^2 d^2 \eta_b^2 R_{\mathrm{int}}}{k_e k_t {k_g}^2 \eta_g^2} - c \right)}{C_0 C_3 (C_0 C_3 - C_1 C_2)} \tag{67}$$

4.2. Optimization Procedure

In this section, an image-based design optimization of the proposed quarter-car suspension model based on standard road excitation is examined. The following procedure was used to optimize the suspension stiffness and damping coefficients of the 1-DOF quarter-car model for ride comfort and power generation.

4.2.1. *Optimization Rule and Design Chart*

The objectives of this optimization are to minimize the RMS of absolute acceleration experienced by the sprung mass and maximize the expectation of the power generated by the damper. The constraints of the optimization rule include the physical limitation of the spring ($k_1 \leq k \leq k_8$) and the limited range of the adjustable damping that can be applied by the DC motor ($c_1 \leq c \leq c_8$). The values of the objective functions are calculated by Eq. (57) and (67).

The expression of the optimization rule is defined as

$$\begin{aligned} &\underset{\text{w.r.t.}\quad (k,c)}{\min} && RMS_a(k,c) \\ &\underset{\text{w.r.t.}\quad (k,c)}{\max} && E_p(k,c) \\ &\text{S.t.} && k_{\text{low}} \leq k \leq k_{\text{high}} \\ & && c_{\text{low}} \leq c \leq c_{\text{high}} \end{aligned} \tag{68}$$

An optimization design chart is created by defining RMS_a and E_P as the Cartesian coordinates, using k and c as parameters. As illustrated in Figure 4.1, each solid curve indicates the values of (RMS_a, E_P) in terms of a fixed value of k and different values of c; each dashed curve indicates the values of (RMS_a, E_P) in terms of a fixed value of c and different values of k. By overlapping the solid and dashed curves, a grid figure was plotted where each intersection on the grid corresponds to a certain pair of (k, c), which exclusively determines a value of (RMS_a, E_P). Four different conditions, shown in Table 4.1, were analyzed to deal with the practical situations in real life.

Table 4.1 Different driving situations

Driving Situation	Road Condition	Driving Speed
Highway I	Grade A	120 km/h
Highway II	Grade B	90 km/h
City	Grade C	50 km/h
Off-road	Grade D	30 km/h

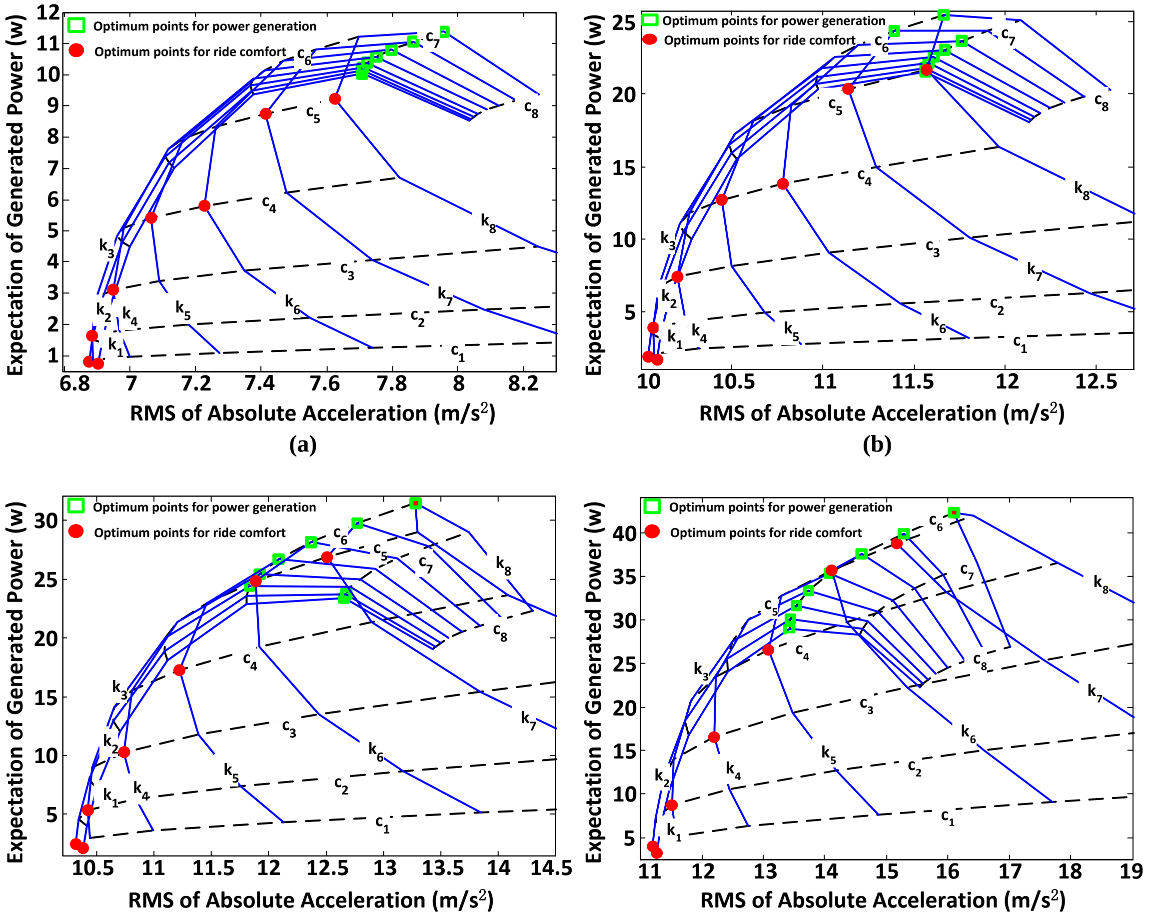

Figure 4.1 Contour curves for functions RMS_a and E_P in terms of (k, c) and optimum points for ride comfort and power generation, based on different driving situations: (a) Highway I, (b) Highway II, (c) City, and (d) Off-road

By inspecting Figure 4.1, it may be noted that

(1) The global optimum points for ride comfort and power generation performance can be found where a red circle with the lowest value in the x-axis and a green square with the highest value in the y-axis;

(2) For each stiffness denoted by a solid blue curve, the local optimum damping points can be found where a minima of absolute acceleration and a maxima of generated power exist;

(3) For ride comfort optimization, low stiffness and low damping provide the best performance; with an increase of stiffness, local optimal damping moves to a higher value;

(4) For power generation optimization, high stiffness and high damping provide the best performance; local optimal damping does not depend significantly on stiffness;

(5) With low stiffness, optimal ride comfort and power generation are in conflict; with high stiffness, both optimal damping points get closer, and optimal ride comfort and power generation become consistent and thus can be optimized simultaneously;

(6) Under Highway conditions, the variation range of absolute acceleration is small. Therefore, optimal stiffness and damping coefficient can be selected to improve power generation effectively while not sacrificing ride comfort significantly;

(7) When stiffness is pre-set, the damping coefficient can be changed between two local optimal points on the same blue curve in real time by an electronic circuit proposed by (Huang, Hsieh, Golnaraghi, & Moallem, 2015).

4.2.2. Local Optimization for Energy Harvesting

When the spring constant k_i is selected and its value is fixed, the local optimization for energy harvesting is determined by the damping coefficient chosen to satisfy the following condition:

$$\frac{\partial E_P(k_i,c)}{\partial c}=0 \qquad \frac{\partial^2 E_P(k_i,c)}{\partial c^2}<0 \tag{69}$$

The complete closed-form expression of the optimum damping coefficient can be obtained by solving Eq. (69). It should be noted that the damping coefficient must be a positive real number. Therefore, only one analytical solution was found that maximizes the electrical power generation. The expression is

$$c_{opt}=-\frac{\beta}{4\alpha}-\rho_6+\frac{1}{2}\sqrt{-4\rho_6^2-2\rho_3+\frac{\rho_4}{\rho_6}} \tag{70}$$

where

$$\begin{aligned}
\tau &= \frac{c^2 d^2 \eta_b^2 R_{\text{int}}}{k_e k_t {k_g}^2 \eta_g^2} \\
\alpha &= \omega_c^2 \tau \\
\beta &= 2\omega_c \tau \left(\omega_c^2 m_{\text{eq}} + 2\omega_c c_f + k\right) \\
\gamma &= \left(\omega_c^2 m_{\text{eq}} + \omega_c c_f + k\right)\left(4\omega_c c_f \tau - \omega_c + k\tau\right) + \omega_c\left(\omega_c c_f^2 \tau + c_f k\tau + k\right) \\
\delta &= -2c_f\left(\omega_c^2 m_{\text{eq}} + \omega_c c_f + k\right)\left(\omega_c - \omega_c c_f \tau - k\tau\right) \\
\varphi &= -c_f\left(\omega_c^2 m_{\text{eq}} + \omega_c c_f + k\right)\left(\omega_c c_f + k\right) \\
\rho_1 &= \gamma^2 - 3\beta\delta + 12\alpha\varphi \\
\rho_2 &= 2\gamma^3 - 9\beta\gamma\delta + 27\beta^2\varphi + 27\alpha\delta^2 - 72\alpha\gamma\varphi \\
\rho_3 &= \frac{8\alpha\gamma - 3\beta^2}{8\alpha^2} \\
\rho_4 &= \frac{\beta^3 - 4\alpha\beta\gamma + 8\alpha^2\delta}{8\alpha^3} \\
\rho_5 &= \sqrt[3]{\frac{\rho_2 + \sqrt{\rho_2^2 - 4\rho_1^3}}{2}} \\
\rho_6 &= \frac{1}{2}\sqrt{-\frac{2}{3}\rho_3 + \frac{1}{3\alpha}(\rho_5 + \frac{\rho_1}{\rho_5})}
\end{aligned} \tag{71}$$

In Figure 4.2, local optimization curves for power generation in the City driving situation are plotted. It can be seen that the analytical solutions match the maximum points on the curves. By decreasing the interval of the parameters selection, the optimum points from the design chart approach the analytical solutions.

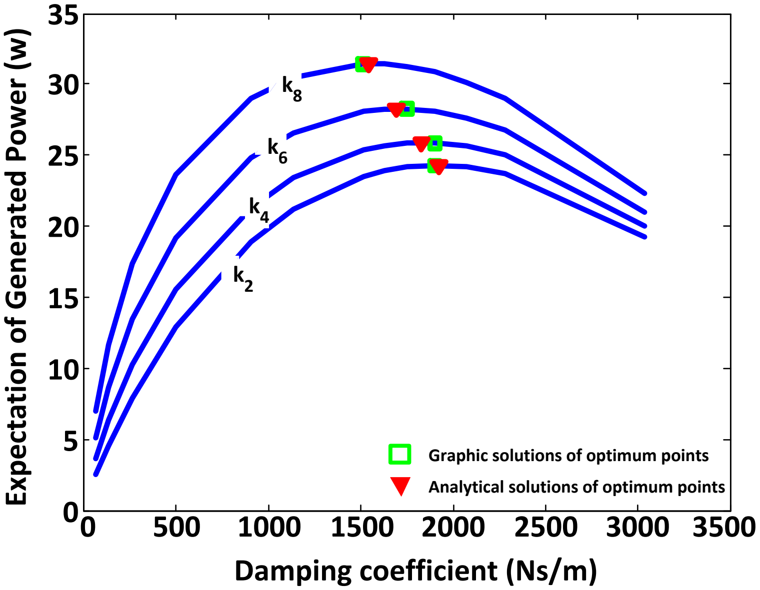

Figure 4.2 Local optimization for energy harvesting in a City driving situation when the spring constant is selected as $\boldsymbol{k_2, k_4, k_6, k_8}$, respectively

4.3. Simulation and Experimental Results

The 1-DOF experimental system proposed in Section 2.4 was utilized to verify the proposed optimization method.

4.3.1. Road Profile Generation

The road profile can be represented by a unit-intensity white noise signal passing through a first-order transfer function given by

$$G(s) = \frac{\sqrt{2\pi G_0 V}}{s} \tag{72}$$

The numerical calculation for the road profile was carried out by Matlab/Simulink. Figure 4.3 shows the generated road roughness in the time domain for Highway I and City situations (see Table 4.1). Fast Fourier transform was used to get the PSD from the time domain to the frequency domain. Figure 4.4 indicates that the transformed PSD curve fits the theoretical value well.

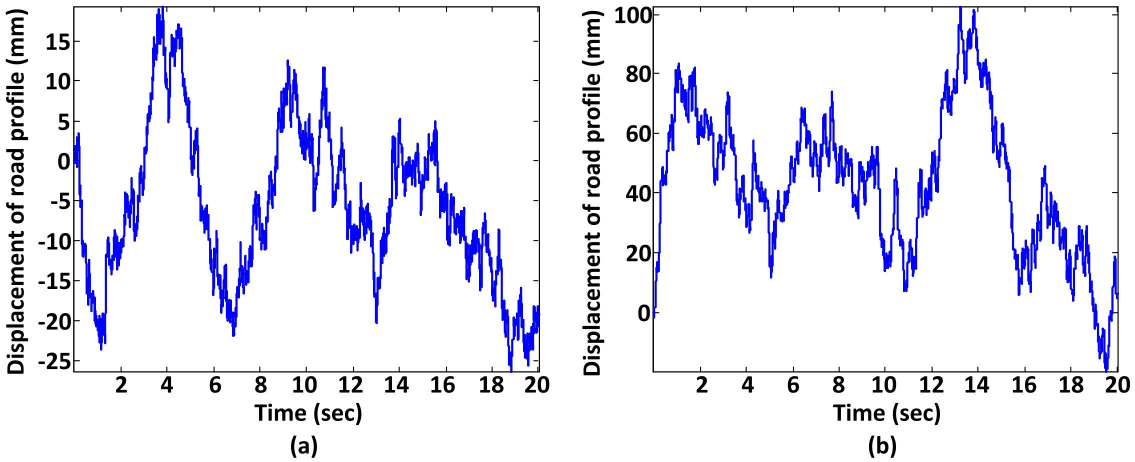

Figure 4.3 Standard road profile for (a) Highway I and (b) City situations

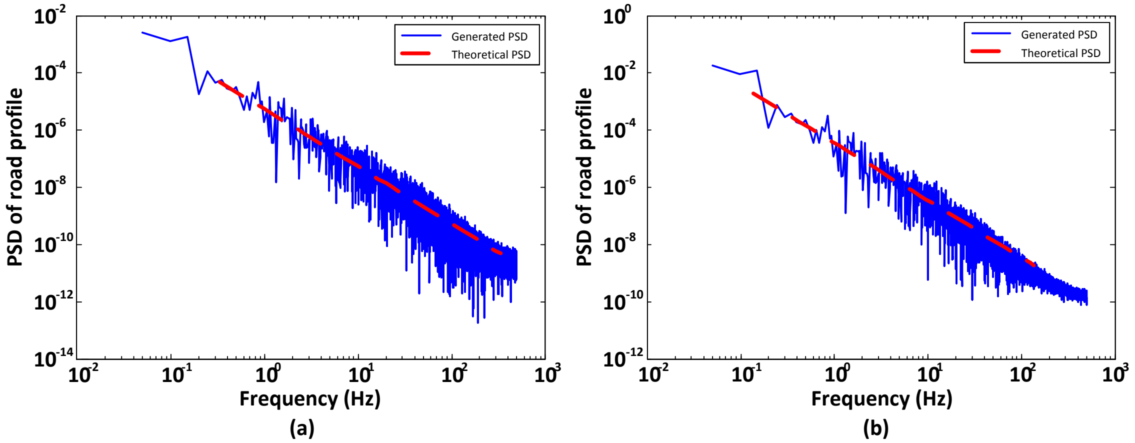

Figure 4.4 Power spectral density of road profile for (a) Highway I and (b) City situations

4.3.2. System Performance of Ride Comfort and Power Generation

In this experiment, the suspension was excited by the standard road profile, as depicted in Figure 4.3. The responses of the system, such as absolute acceleration and instantaneous power, were acquired, and RMS of absolute acceleration and expectation of generated power were calculated over the road range. Two different sets of springs were selected with soft stiffness and hard stiffness, respectively. The variable electrical damping coefficient ranges from 70.2 Ns/m to 3042.5 Ns/m by adjusting the value of the load resistor from 640 Ω to 5 Ω. The absolute acceleration of the sprung mass ($\ddot{x}$) and voltage of the load resistor (V_{load}) were measured, and the instantaneous electrical power was calculated based on $P = V_{load}^2 / R_{load}$.

To verify the proposed optimization method, the curves of RMS of absolute acceleration and expectation of generated power were built and compared with the optimization curves depicted in Figure 4.1. For a better view of the comparison, the plot, such as in Figure 4.1, was divided into two equivalent plots which show ride comfort and power generation performance individually. Referring to Figure 4.5 and Figure 4.6, the optimum points derived from the analytical solution (red solid circle and green solid square) and experimental test (red hollow circle and green hollow square) match well under different conditions, although some value differences between the curves exist due to the uncertainties in the experimental tests that cannot be estimated in the analytical solution.

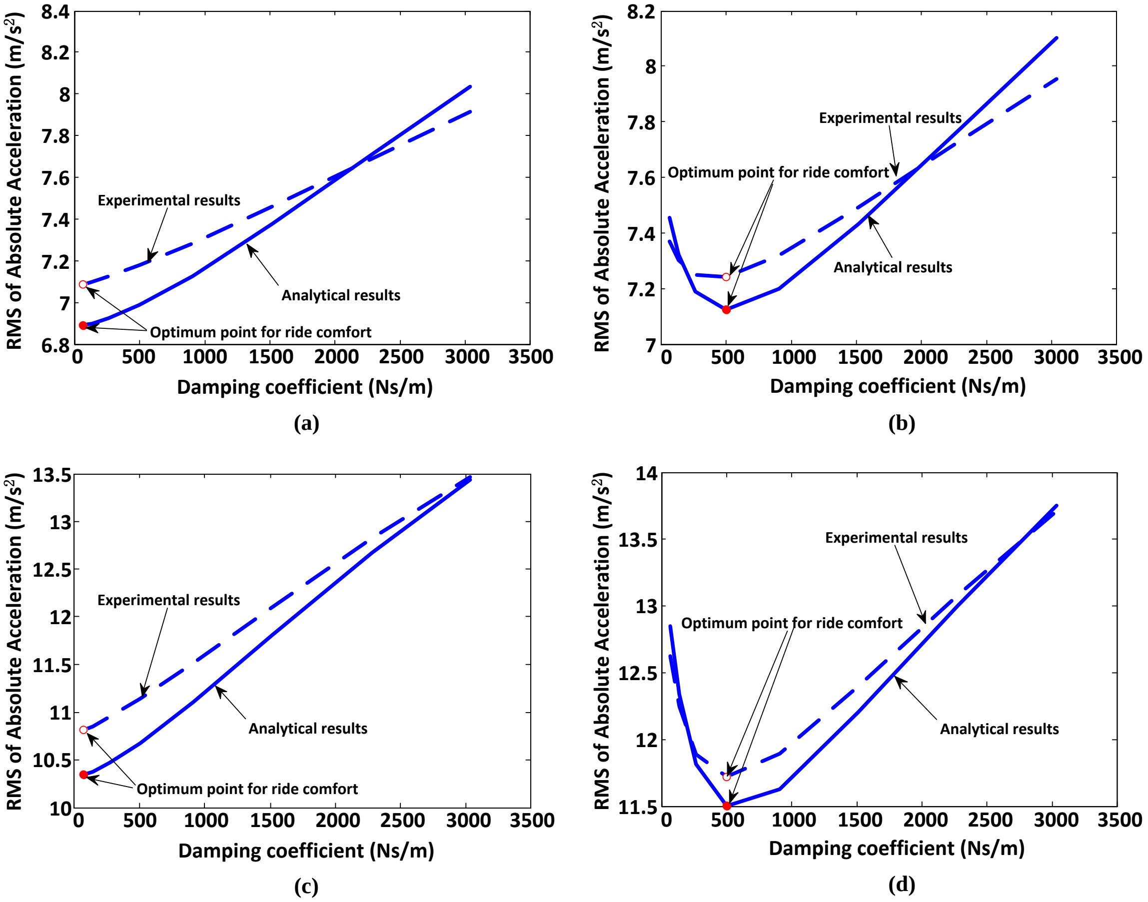

Figure 4.5 Comparison of RMS of absolute acceleration between analytical solution and experimental test for (a) Highway I situation and soft spring setup, (b) Highway I situation and hard spring setup, (c) City situation and soft spring setup, and (d) City situation and hard spring setup

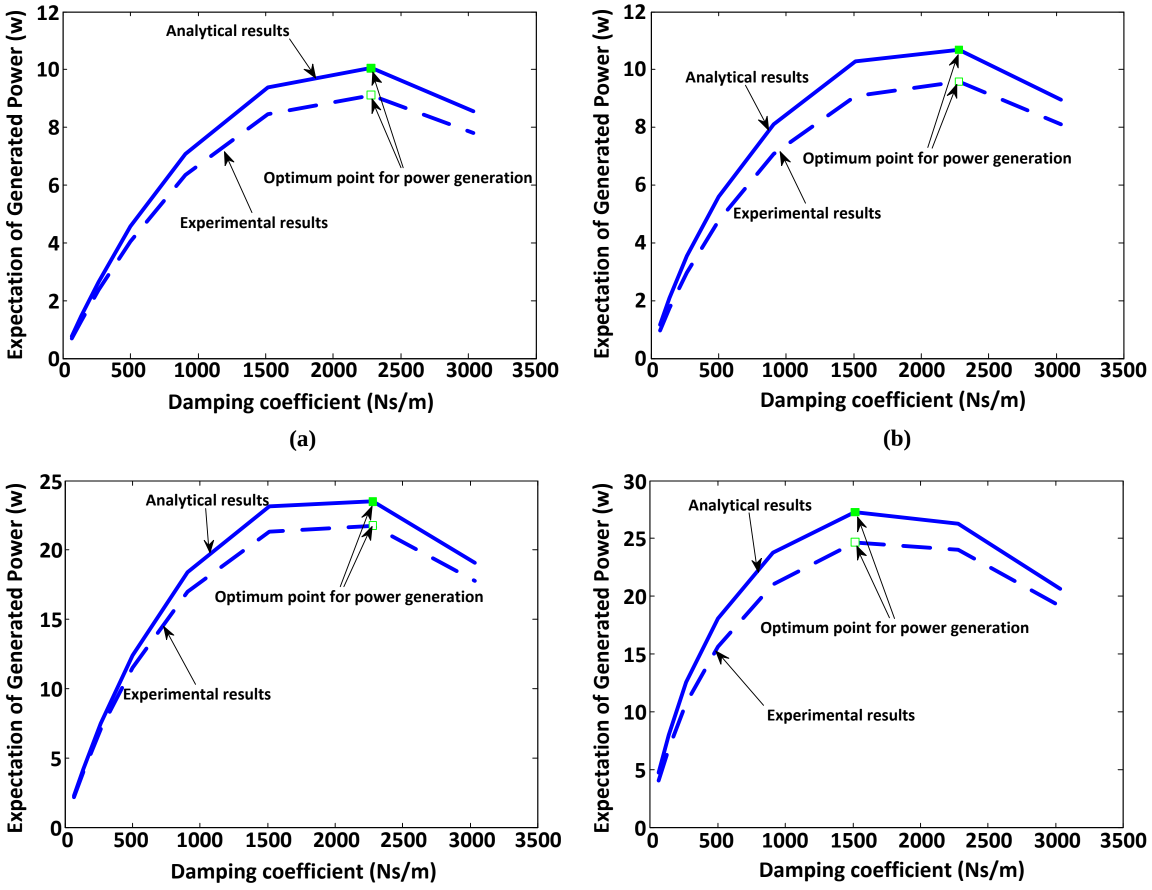

(a)

(b)

(c)

(d)

Figure 4.6 Comparison of expectation of generated power between analytical solution and experimental test for (a) Highway I situation and soft spring setup, (b) Highway I situation and hard spring setup, (c) City situation and soft spring setup, and (d) City situation and hard spring setup

Figure 4.7 shows the absolute acceleration and generated power in the time domain when damping is selected at the ride comfort optimal point or power generation optimal point in the Highway I situation, while Figure 4.8 shows the results in the City situation. Comparing the responses between different performance optimizations (ride comfort / power generation) in the time domain, we can see that changing damping and stiffness values significantly influences the suspension system’s performance.

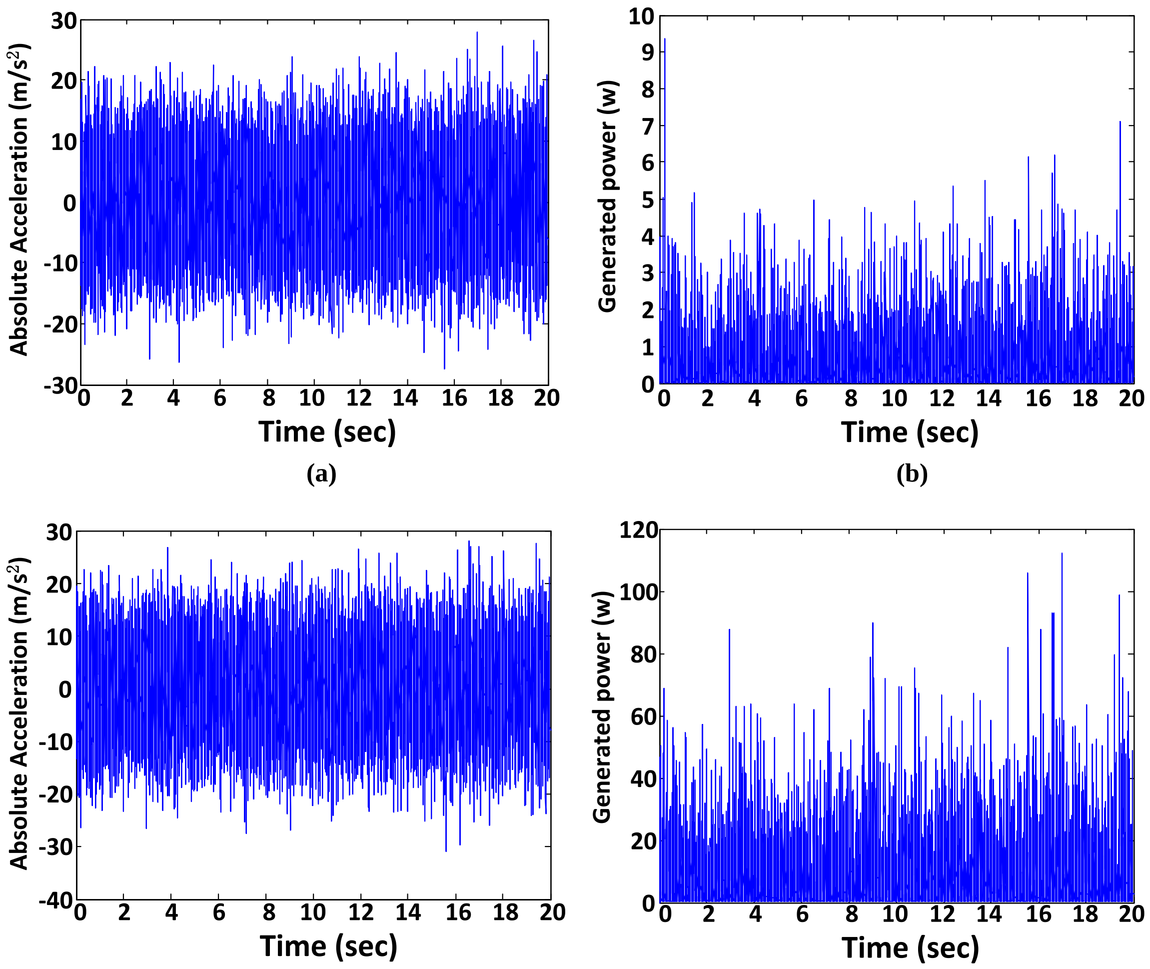

(a) (b)

(c) (d)

Figure 4.7 System responses in the Highway I situation with optimal damping for best ride comfort performance: (a) absolute acceleration and (b) generated power; for best power generation performance: (c) absolute acceleration and (d) generated power

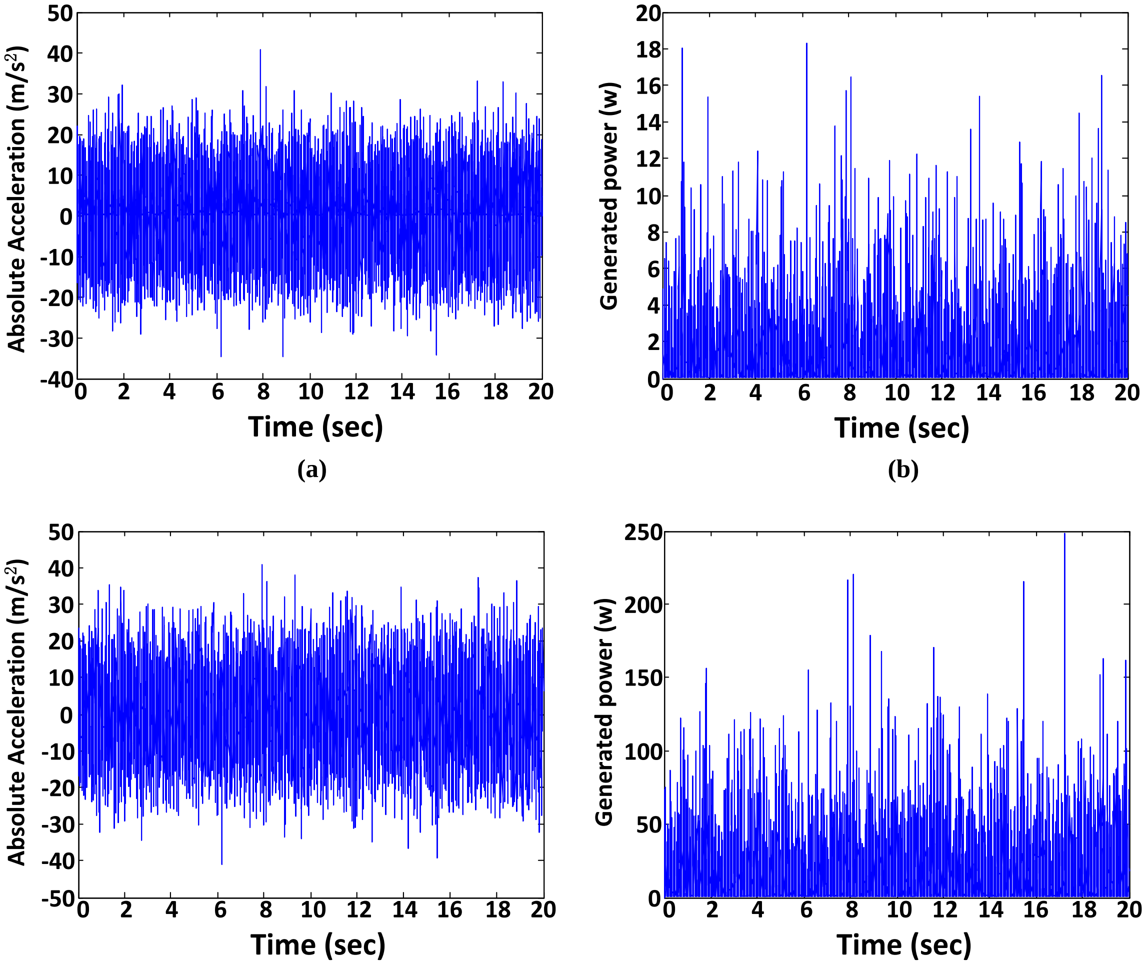

(a) (b)

(c) (d)

Figure 4.8 System responses in the City situation with optimal damping for best ride comfort performance: (a) absolute acceleration and (b) generated power; for best power generation performance: (c) absolute acceleration and (d) generated power

Table 4.2 demonstrates the calculated values of experimental results in the corresponding Figure 4.7 and Figure 4.8 for a better comparison. From the table, we can see that optimization makes a significant improvement in both ride comfort and power generation.

Table 4.2 Experimental results of performance indices in Highway I and City situations

	Highway I		City	
	RMS of Absolute Acceleration (m/s^2)	Average of Generated Power (W)	RMS of Absolute Acceleration (m/s^2)	Average of Generated Power (W)
Optimal Ride Comfort	7.0889	0.4496	9.0132	1.2851
Optimal Power Generation	7.7261	6.3898	10.3372	14.5139

4.4. Conclusion

In this chapter, an analytical methodology for the optimal design of the suspension system based on stochastic road excitation was proposed. The actual road roughness was modeled by the ISO 8608 standard road profile for different roughness grades and utilized in deriving the closed-form solutions. Four different driving conditions were analyzed, and optimization design charts were produced analytically. To validate the obtained optimum parameters, experiments were implemented under different driving conditions, and test results suggested that the proposed method was effective and credible in predicting and determining the optimality of system performance.

Thus far the suspension system has a narrow bandwidth which limits the power regeneration capability, as opposed to the system which has wider bandwidth. Therefore, an attempt is made to enhance the system's frequency bandwidth by introducing nonlinearities, and is presented in the next chapter.

Chapter 5.

Bandwidth Enhancement Utilizing Nonlinear Stiffness

This chapter aims at introducing how to utilize cubic nonlinearities in the system to extend the bandwidth, which has been proven to be useful for energy harvesting purposes but was not used in vehicle systems before. It also aims to explain how the regenerative damper can act as a traditional damper to provide the damping force for vibration suppression and how much power the system can regenerate. Two different nonlinear systems are investigated that electrically and mechanically realize the cubic nonlinearity, respectively.

5.1. Motivation

To date, the linear resonant generator is the most common device used in energy harvesting applications. In accordance with this concept, the generator captures the maximum power at its resonant frequency. However, a drawback occurs in that performance is sacrificed significantly if a difference between two frequencies exists because of the narrow bandwidth of this system, as shown in Figure 5.1.

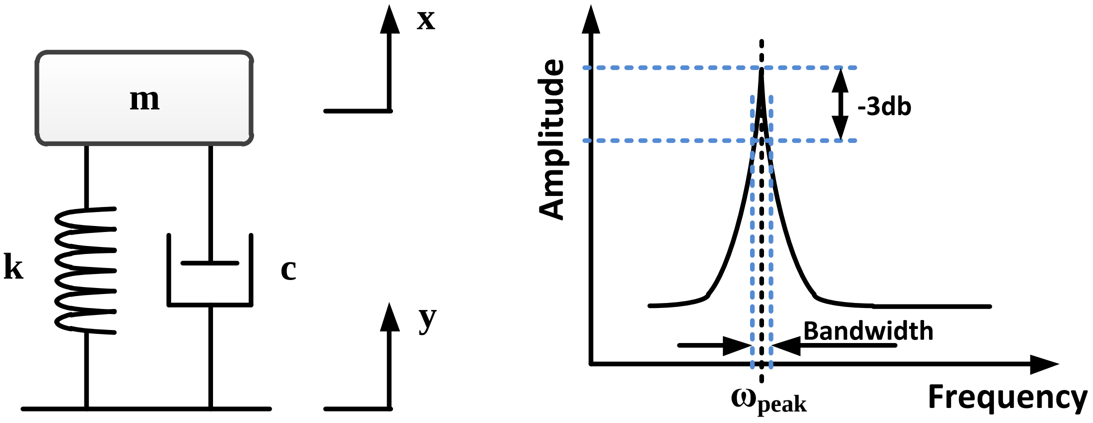

Figure 5.1 A simple model of a linear suspension system and its frequency-response curve

The limited bandwidth of the linear resonant generator restricts the effectiveness of harvesting energy because it must ensure that its natural frequency matches the main frequency of the input vibration. However, road roughness always contains a broad range of frequencies, and it is hard to measure the main frequency. To overcome this disadvantage, a cubic nonlinearity strategy is considered in this chapter. By adding cubic nonlinearities into the regenerative suspension system, the forced oscillation of the system is governed by the Duffing equation (Nayfeh, 2011), whose form is expressed as

$$\ddot{x} + \delta\dot{x} + \alpha x + \beta x^3 = Y\cos(\omega t) \tag{73}$$

where $Y\cos(\omega t)$ is the external excitation; δ, α, and β indicate the level of damping, spring constant, and nonlinearity in the system. The system modeled by the Duffing equation presents a jump resonance phenomenon in the frequency response and is supposed to bend the frequency-response curve to the higher/lower range, thus effectively extending the bandwidth. A typical frequency response of the vibrational system with cubic nonlinearities is shown in Figure 5.2 and is compared with the frequency response of the conventional linear vibrational system. There are two unstable response regions indicated in red.

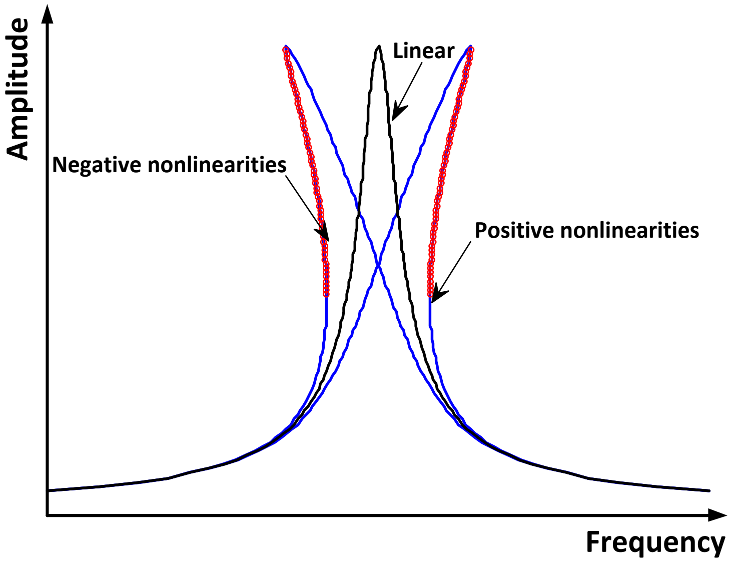

Figure 5.2 Frequency-response curves of linear and nonlinear systems

For the purpose of providing cubic nonlinearities for the suspension system, there are two different methods taken into consideration: physical nonlinear spring and synthesized nonlinear stiffness. Theoretically, both methods result in the same system response, but they have different effects in terms of power regeneration. The 1-DOF suspension systems using these two methods are represented in Figure 5.3, respectively.

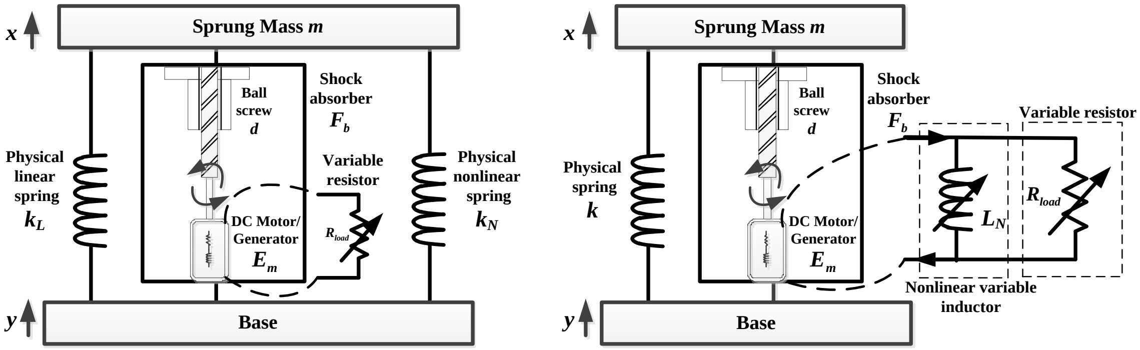

(a) (b)

Figure 5.3 1-DOF model of the regenerative suspension system with (a) physical nonlinear spring and (b) nonlinear variable inductor

5.2. Nonlinear Variable Inductor System

5.2.1. *System Description and Modeling*

Since it is difficult to manufacture a pure cubic nonlinear physical spring in practice, nonlinear stiffness synthesization in the electrical domain is taken into consideration first. In order to correctly supply the cubic nonlinearity to the system, a variable inductor was designed in the electronic circuit (Hsieh, Huang, Golnaraghi, & Moallem, 2013). The controller should always maintain both the instantaneous current and voltage flux through the inductor to the following relationship:

$$i_L = \alpha_N \varphi^3 \tag{74}$$

Where $\varphi = \int v_L dt$ is the flux (integral of terminal voltage) of the inductor, α_N is the factor of the nonlinearity. Differentiating both sides of Eq. (74), we obtain

$$\frac{di_L}{dt} = 3\alpha_N \varphi^2 v_L \tag{75}$$

$$\begin{aligned} L_N(\varphi) &= \frac{1}{3\alpha_N \varphi^2} \\ &= \frac{1}{3\alpha_N (\int v_L dt)^2} \end{aligned} \tag{76}$$

Therefore, $L_N(\varphi)$ in Eq. (76) is the nonlinear inductance to be designed in the electronic circuit in order to satisfy the relationship, as indicated in Eq. (74). Since a permanent magnetic DC motor acts as a generator simultaneously, the internal resistance of the motor is concerned while the internal inductance is ignored. Therefore, the total current and output torque of the motor can be derived as

$$I = \frac{k_e k_g \eta_g}{R_{int} + R_{load}} \dot{\theta} + \frac{R_{load} \alpha_N k_e^3 k_g^3 \eta_g^3}{R_{int} + R_{load}} \theta^3 \tag{77}$$

$$\begin{aligned} \tau_i &= k_t I \\ &= \frac{k_t k_e k_g \eta_g}{R_{int} + R_{load}} \dot{\theta} + \frac{R_{load} \alpha_N k_t k_e^3 k_g^3 \eta_g^3}{R_{int} + R_{load}} \theta^3 \end{aligned} \tag{78}$$

Based on Eq. (7), the equation of the rotor dynamics, the output torque of the damper would be

$$\begin{aligned} \tau_b &= k_g \eta_g \tau_i + (J_m k_g^2 \eta_g^2 + J_g + J_b) \ddot{\theta} \\ &= \frac{k_t k_e k_g^2 \eta_g^2}{R_{int} + R_{load}} \dot{\theta} + \frac{R_{load} \alpha_N k_t k_e^3 k_g^4 \eta_g^4}{R_{int} + R_{load}} \theta^3 + (J_m k_g^2 \eta_g^2 + J_g + J_b) \ddot{\theta} \end{aligned} \tag{79}$$

According to the properties of the ball screw mechanism, as indicated in Eq. (5) and (9), the equivalent output force of the damper is obtained as follows:

$$F_b = \frac{k_t k_e k_g^2 \eta_g^2}{(R_{int} + R_{load}) d^2 \eta_b^2} \dot{z} + \frac{R_{load} \alpha_N k_t k_e^3 k_g^4 \eta_g^4}{(R_{int} + R_{load}) d^4 \eta_b^4} z^3 + \frac{(J_m k_g^2 \eta_g^2 + J_g + J_b)}{d^2 \eta_b^2} \ddot{z} \tag{80}$$

Consequently, assuming the external excitation is $y = Y \cos \omega t$, the dynamic equation of the whole system is derived as

$$\left(m + \frac{J_m k_g^2 \eta_g^2 + J_g + J_b}{d^2 \eta_b^2}\right) \ddot{z} + \left(c_f + \frac{k_t k_e k_g^2 \eta_g^2}{(R_{int} + R_{load}) d^2 \eta_b^2}\right) \dot{z} + kz + \frac{R_{load} \alpha_N k_t k_e^3 k_g^4 \eta_g^4}{(R_{int} + R_{load}) d^4 \eta_b^4} z^3 = mY\omega^2 \cos \omega t \tag{81}$$

Eq. (81) can be simplified as

$$m_{eq} \ddot{z} + c_{eq} \dot{z} + kz + k_N z^3 = mY\omega^2 \cos \omega t \tag{82}$$

The equivalent mass, damping coefficient, linear and nonlinear spring constant, and excitation amplitude are listed in Table 5.1.

Table 5.1 Equivalent parameters of the nonlinear suspension model

Symbol	Description
$\boldsymbol{m_{eq}}$	$m+\dfrac{J_m k_g^2 \eta_g^2 + J_g + J_b}{d^2 \eta_b^2}$
$\boldsymbol{c_{eq}}$	$c_f+\dfrac{k_t k_e k_g^2 \eta_g^2}{(R_{int}+R_{load}) d^2 \eta_b^2}$
$\boldsymbol{k_N}$	$\dfrac{R_{load}\alpha_N k_t k_e^3 k_g^4 \eta_g^4}{(R_{int}+R_{load}) d^4 \eta_b^4}$

5.2.2. Theoretical Analysis

In this section, the effect of cubic nonlinearities is studied by utilizing the perturbation method (e.g., method of multiple scales, method of averaging, Lindstedt-Poincare technique). Especially the method of multiple scales will be used to analyze the system dynamics. The dynamic equation of the nonlinear suspension system, as shown in Eq. (82), can be rewritten as

$$\ddot{z}+2\zeta\omega_0\dot{z}+\omega_0^2 z+k_N'\omega_0^2 z^3=F\omega^2\cos\omega t \tag{83}$$

where

$$\omega_0=\sqrt{\frac{k}{m_{eq}}} \qquad \zeta=\frac{c_{eq}}{2\sqrt{m_{eq}k}} \qquad k_N'=\frac{k_N}{k} \qquad F=\frac{mY}{m_{eq}} \tag{84}$$

Theoretically, there are multiple resonances existing in the system with cubic nonlinearities (Nayfeh & Mook, 2008). Since, in reality, most energy introduced from the road surface to the suspension locates in the region around the natural frequency, we focused on analyzing the nonlinear effect on the primary resonance where the excitation frequency is near the natural frequency.

(1) Nondimensionalization

In order to guarantee the solution to be independent, the system response z needs to be dimensionless with respect to the initial displacement z_0, whereas the time t can be made dimensionless by using $T = \frac{1}{\omega_0}$. Thus, let

$$u = \frac{z}{z_0} \qquad t^* = \frac{t}{T} = \omega_0 t \tag{85}$$

and

$$\begin{aligned} \frac{dz}{dt} &= \omega_0 z_0 \frac{du}{dt^*} \\ \frac{d^2z}{dt^2} &= \omega_0^2 z_0 \frac{d^2u}{dt^{*2}} \end{aligned} \tag{86}$$

By performing transformation, Eq. (83) becomes

$$\omega_0^2 z_0 \frac{d^2u}{dt^{*2}} + 2\zeta\omega_0^2 z_0 \frac{du}{dt^*} + \omega_0^2 z_0 u + k_N' \omega_0^2 z_0^3 u^3 = F\omega^2 \cos\frac{\omega}{\omega_0} t^* \tag{87}$$

$$\frac{d^2u}{dt^{*2}} + 2\zeta \frac{du}{dt^*} + u + \epsilon k_N^* u^3 = F^* \omega^{*2} \cos\omega^* t^* \tag{88}$$

where

$$\epsilon \in (0,1) \qquad k_N^* = \frac{k_N' z_0^2}{\epsilon} \qquad F^* = \frac{F}{z_0} \qquad \omega^* = \frac{\omega}{\omega_0} \tag{89}$$

Assuming the damping and nonlinear terms interact at the same level of approximation, we let

$$\zeta = \epsilon\mu \tag{90}$$

where

$$\mu = \frac{\zeta}{\epsilon} = \frac{c_{eq}}{2\epsilon\sqrt{m_{eq}k}} \tag{91}$$

Finally, Eq. (88) becomes

$$\frac{d^2u}{dt^{*2}} + 2\epsilon\mu\frac{du}{dt^*} + u + \epsilon k_N^* u^3 = F^*{\omega^*}^2\cos\omega^* t^* \tag{92}$$

(2) Perturbation Analysis of Primary Resonance

A detuning parameter, σ, is introduced to quantitatively describe the nearness of excitation frequency ω to natural frequency ω_0. Accordingly, it can be written as

$$\omega^* = 1 + \epsilon\sigma \tag{93}$$

An approximate solution to the problem can be obtained by a number of perturbation techniques. To use the method of multiple scales, we reorder the level of excitation so that it appears at $O(\epsilon)$, where the nonlinear and damping terms first appear. This leads to a linear problem at $O(\epsilon^0)$.

Let $F^* = \epsilon f$ and rewrite Eq. (92) as

$$\frac{d^2u}{dt^{*2}} + 2\epsilon\mu\frac{du}{dt^*} + u + \epsilon k_N^* u^3 = \epsilon f(1+\epsilon\sigma)^2 \cos\omega^* t^* \tag{94}$$

Introducing the normal scale $T_0 = t^*$ and the slower scale $T_1 = \epsilon t^*$, then Eq. (94) becomes

$$D_0^2 u + 2\epsilon D_0 D_1 u + 2\epsilon\mu D_0 u + u + \cdots + \epsilon k_N^* u^3 = \epsilon f(1+\epsilon\sigma)^2 \cos\omega^* T_0 \tag{95}$$

where first- and second-order derivative operators with respect to the T_0 and T_1 are

$$\frac{d}{dt^*} = D_0 + \epsilon D_1 + \cdots \tag{96}$$

$$\frac{d^2}{dt^{*2}} = D_0^2 + 2\epsilon D_0 D_1 + \cdots \tag{97}$$

We seek an approximate solution for u in a power series of ϵ, which is expressed in the form

$$u = u_0(T_0, T_1) + \epsilon u_1(T_0, T_1) + \cdots \tag{98}$$

Substituting (98) into (95) and equating coefficients of like powers of ϵ, we obtain

$$D_0^2 u_0 + u_0 = 0 \tag{99}$$

$$D_0^2 u_1 + u_1 = -2D_0 D_1 u_0 - 2\mu D_0 u_0 - k_N^* u_0^3 + f\cos\omega^* T_0 \tag{100}$$

The general solution of Eq. (99) is expected to be in the form of

$$u_0 = A(T_1)e^{iT_0} + \bar{A}(T_1)e^{-iT_0} \tag{101}$$

where $A(T_1)$ and $\bar{A}(T_1)$ are complex conjugates and in polar form:

$$A = \frac{1}{2}ae^{i\beta} \qquad \bar{A} = \frac{1}{2}ae^{-i\beta} \tag{102}$$

Substituting Eq. (101) into (100) results in

$$\begin{aligned} D_0^2u_1 + u_1 = -(2iA' + 2i\mu A + 3k_N^*A^2\bar{A})e^{iT_0} - k_N^*A^3e^{3iT_0} + \frac{1}{2}fe^{i\omega^*T_0} \\ + cc \end{aligned} \tag{103}$$

where cc stands for the complex conjugate of the preceding terms. Based on Eq. (93), we can derive that

$$\omega^*T_0 = (1+\epsilon\sigma)T_0 = T_0 + \sigma T_1 \tag{104}$$

Substituting (104) into (103) and eliminating the secular terms (setting coefficients of e^{iT_0} to 0) yields

$$2iA' + 2i\mu A + 3k_N^*A^2\bar{A} - \frac{1}{2}fe^{i\sigma T_1} = 0 \tag{105}$$

Expressing A in polar form as in Eq. (102) and separating real and imaginary parts in Eq. (105) lead to a pair of first-order ordinary differential equations

$$a' = -\mu a + \frac{1}{2} f \sin(\sigma T_1 - \beta) \tag{106}$$

$$a\beta' = \frac{3}{8} k_N^* a^3 - \frac{1}{2} f \cos(\sigma T_1 - \beta) \tag{107}$$

In order to transform the non-autonomous system depicted by Eq. (106) and (107) into an autonomous system, a transformation is introduced

$$\gamma = \sigma T_1 - \beta \tag{108}$$

$$\gamma' = \sigma - \beta' \tag{109}$$

Therefore, Eq. (106) and (107) become

$$a' = -\mu a + \frac{1}{2} f \sin\gamma \tag{110}$$

$$a\gamma' = \sigma a - \frac{3}{8} k_N^* a^3 + \frac{1}{2} f \cos\gamma \tag{111}$$

Considering that when the steady-state motions of the system occur, the time derivatives of a and γ are both zero, which means $a' = \gamma' = 0$. Thus, Eq. (110) and (111) become

$$\mu a = \frac{1}{2} f \sin\gamma \tag{112}$$

$$-\sigma a + \frac{3}{8} k_N^* a^3 = \frac{1}{2} f \cos\gamma \tag{113}$$

Squaring and adding the two equations, we obtain the solution as

$$\sigma = \frac{3}{8}k_N^* a^2 \pm \left(\frac{f^2}{4a^2} - \mu^2\right)^{1/2} \tag{114}$$

In addition, we can also obtain the solution in terms of σ and γ, which gives

$$\sigma = \frac{3k_N^* f^2}{32\mu^2}\sin^2\gamma - \mu\cot\gamma \tag{115}$$

For the first-order approximation, Eq. (103) can be rewritten as

$$\begin{aligned} D_0^2 u_1 + u_1 &= -k_N^* A^3 e^{3iT_0} - k_N^* \bar{A}^3 e^{-3iT_0} \\ &= -\frac{1}{4}k_N^* a^3 \cos(3T_0 + 3\beta) \end{aligned} \tag{116}$$

The particular solution of Eq. (116) can be derived as

$$\begin{aligned} u_1 &= \frac{1}{32}k_N^* a^3 \cos(3T_0 + 3\beta) \\ &= \frac{1}{32}k_N^* a^3 \cos(3\omega^* t^* - 3\gamma) \end{aligned} \tag{117}$$

Finally it follows that the approximation solution (dimensionless) of the system is

$$u = a\cos(\omega^* t^* - \gamma) + \frac{1}{32}\epsilon k_N^* a^3 \cos(3\omega^* t^* - 3\gamma) + \cdots \tag{118}$$

We determined the stability of the steady-state motion by investigating the nature of the singular points a_0, γ_0 of Eq. (110) and (111). The Jacobian matrix of Eq. (110) and (111) at (a_0, γ_0) is derived as

$$\begin{bmatrix} \left.\dfrac{\partial a'}{\partial a}\right|_{a_0} & \left.\dfrac{\partial a'}{\partial \gamma}\right|_{\gamma_0} \\ \left.\dfrac{\partial \gamma'}{\partial a}\right|_{a_0} & \left.\dfrac{\partial \gamma'}{\partial \gamma}\right|_{\gamma_0} \end{bmatrix} = \begin{bmatrix} -\mu & -a_0\left(\sigma - \dfrac{3}{8}k_N^* a_0^2\right) \\ \dfrac{1}{a_0}\left(\sigma - \dfrac{9}{8}k_N^* a_0^2\right) & -\mu \end{bmatrix} \tag{119}$$

One can obtain the following eigenvalue equation by taking the determinant of the matrix:

$$\det\begin{bmatrix} -\mu-\lambda & -a_0\left(\sigma - \dfrac{3}{8}k_N^* a_0^2\right) \\ \dfrac{1}{a_0}\left(\sigma - \dfrac{9}{8}k_N^* a_0^2\right) & -\mu-\lambda \end{bmatrix} = 0 \tag{120}$$

Expanding this determinant yields

$$\lambda^2 + 2\mu\lambda + \mu^2 + \left(\sigma - \frac{3}{8}k_N^* a_0^2\right)\left(\sigma - \frac{9}{8}k_N^* a_0^2\right) = 0 \tag{121}$$

Hence the steady-state motions are unstable (saddle points) when

$$\mu^2 + \left(\sigma - \frac{3}{8}k_N^* a_0^2\right)\left(\sigma - \frac{9}{8}k_N^* a_0^2\right) < 0 \tag{122}$$

and are otherwise stable.

(3) Frequency Responses

A representative curve of a or γ as a function of σ can be obtained for given μ, k_N^* and f, which is called a frequency-response curve. By solving Eq. (114) and (115), a series of points corresponding to the singular points in different state planes can be plotted. From Eq. (114), the amplitude curve is obtained. The solution is valid only if $a \leq \frac{f}{2\mu}$, so the peak amplitude is given by $a_p = \frac{f}{2\mu}$. Figure 5.4 (a) shows the amplitude curve. From Eq. (115), the phase curve is obtained. Since $a > 0$ and $\sin\gamma > 0$, we know that $\gamma \in (0, \pi)$. Figure 5.4 (b) shows the phase curve. The other parameters are selected as $\epsilon = 0.1$, $\mu = 1.51$, $f = 19.10$, $k_N^* = 1.1$.

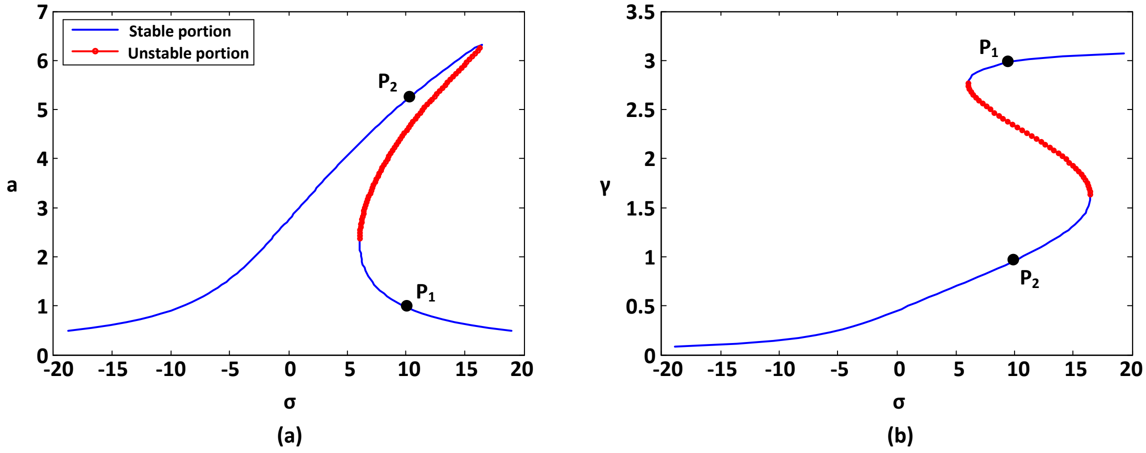

Figure 5.4 Frequency responses of the system at primary resonance: (a) amplitude curve and (b) phase curve

From the frequency-response curves, it can be seen that the effect of the cubic stiffness is to bend the amplitude curve and distort the phase curve to the right for the positive nonlinearity (or to the left for the negative nonlinearity). The extent of bending is dependent on the value of k_N^*. From Figure 5.4, the portion indicated by a series of red circles indicates the unstable states that meet the condition in Eq. (122). Therefore, the steady-state solutions corresponding to the portion of red circles cannot be physically realized by the system.

In the region where unstable steady-state solutions exist, there are more than one stable steady-state solutions. In this case, the initial conditions determine which steady-state solution is physically realized by the system. To illustrate this point, we used Eq. (110) and (111) to calculate trajectories in the state plane corresponding to certain σ with different initial conditions. Figure 5.5 shows the trajectories for $\sigma = 10$. The blue curve indicates the trajectory with the initial condition ($a_0 = 0.5, \gamma_0 = 1.1$), and it leads to the stable foci P_1(0.98, 2.99); the red curve indicates the trajectory with the initial condition ($a_0 = 4, \gamma_0 = 0.1$), and it leads to the stable foci P_2(5.18, 0.96). The arrows indicate the direction of the motion of the representative points.

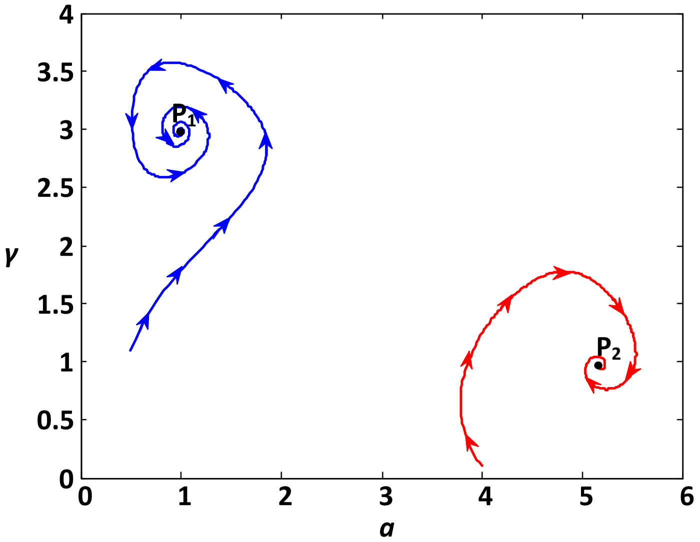

Figure 5.5 State plane of (a, γ) for $\sigma = 10$, where two stable solutions exist

(4) Jump Phenomenon

The bending of the frequency-response curve is responsible for a jump phenomenon. A simulation was performed to illustrate this phenomenon. In this simulation, the amplitude of the excitation was held fixed, the frequency of the excitation (σ) is slowly varied up (-5 to +25) and down (+25 to -5), and the amplitude and phase of the harmonic response were observed. Figure 5.6 shows jump phenomena of the amplitude and phase. The blue curves indicate the trajectories when σ starts from a low frequency ($\sigma = -5$) to a high frequency ($\sigma = 25$); the red curves indicate the trajectories when σ starts from a high frequency ($\sigma = 25$) to a low frequency ($\sigma = -5$). The arrows indicate the direction of the motion and jump.

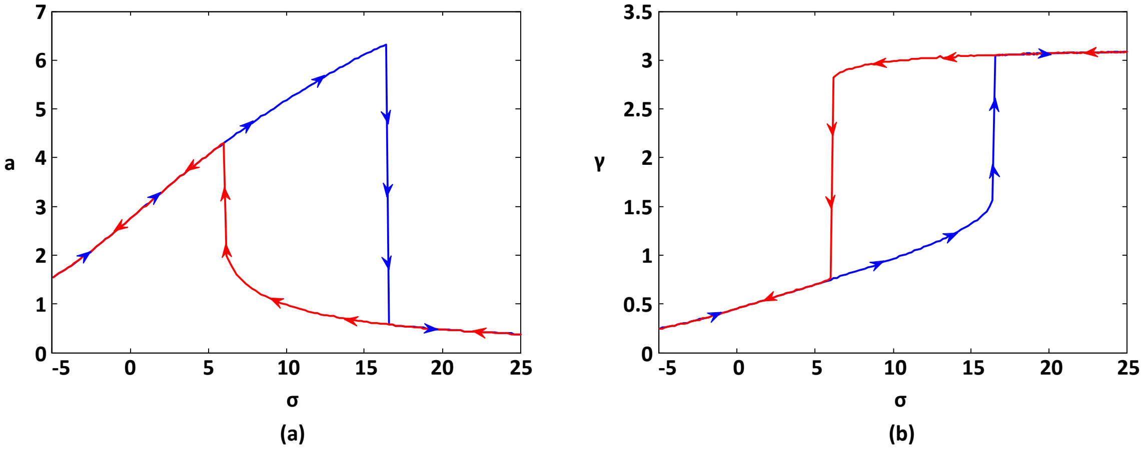

Figure 5.6 Jump phenomena of the system at primary resonance: (a) amplitude curve and (b) phase curve

(5) Time Responses

To verify the correctness of system responses approximated by the perturbation method, time response curves of dimensional solutions were generated and showed both transient and steady-state responses, based on two stable points at lower frequency ($\sigma = -2$) and higher frequency ($\sigma = 5$). The comparison was performed between numerical simulation results and analytical results approximated by the method of multiple scales, as shown in Figure 5.7. From the comparison, we can see that there are some deviations in phases under transient responses at the higher frequency. The results verify that the approximation using the perturbation method (i.e., the method of multiple scales) is capable of predicting the system responses with some errors in certain regions.

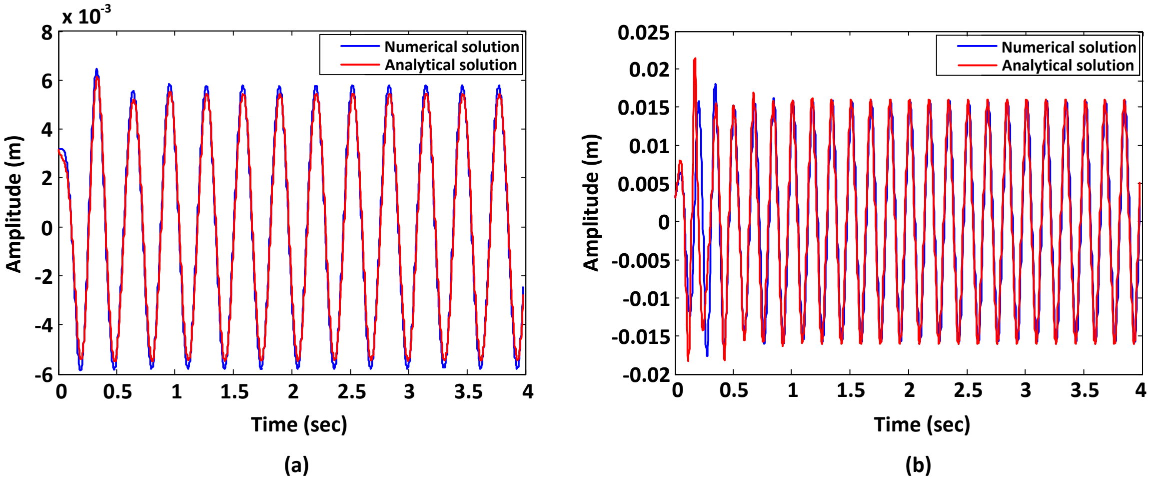

Figure 5.7 Time responses of the system at primary resonance: (a) low frequency ($\sigma = -2$) and (b) high frequency ($\sigma = 5$)

5.3. Physical Nonlinear Spring System Versus Synthesized Nonlinear Inductor System

The purpose of introducing the nonlinear variable inductor was to apply the cubic nonlinearity to the system, thus widening the bandwidth and increasing power generation potential. Therefore, it was necessary to examine the generated power delivered to the electrical load and compare it to the power from the physical nonlinear spring system.

(1) Circuit Model

Physical Nonlinear Spring System	Synthesized Nonlinear Inductor System
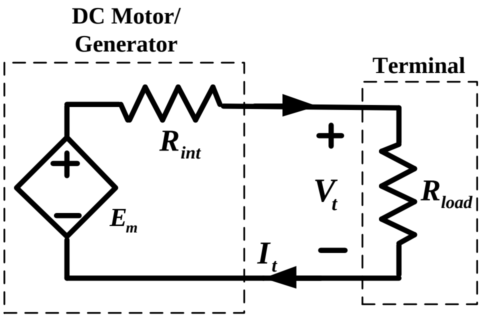	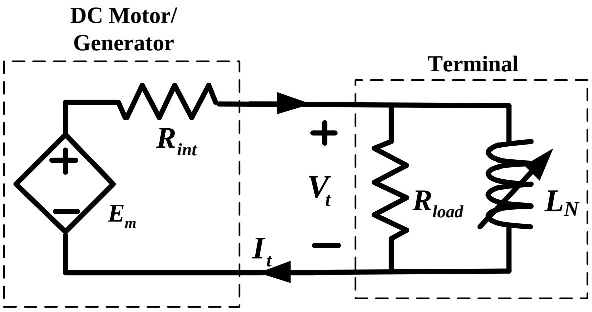

The circuit model represents the terminal of power generation connected to the DC motor/generator. For the physical nonlinear spring system, the terminal is a load resistor; for the synthesized nonlinear inductor system, the terminal is a parallel of load resistor and variable nonlinear inductor.

(2) Nonlinear Stiffness

Physical Nonlinear Spring System	Synthesized Nonlinear Inductor System
k_N	$\boldsymbol{\frac{R_{load}\alpha_N k_t k_e^3 k_g^4 \eta_g^4}{(R_{int}+R_{load})d^4\eta_b^4}}$

The nonlinear variable inductor is studied here to replace the nonlinear physical spring, so this is the prerequisite that the nonlinear stiffness from the two systems should be equivalent. That is,

$$k_N = \frac{R_{load}\alpha_N k_t k_e^3 k_g^4 \eta_g^4}{(R_{int}+R_{load})d^4\eta_b^4} \tag{123}$$

(3) Dynamic Equation and Responses

Physical Nonlinear Spring System	Synthesized Nonlinear Inductor System
$m_{eq}\ddot{z} + c_{eq}\dot{z} + kz + k_N z^3 = Y_t \cos \omega t$	$\boldsymbol{m_{eq}\ddot{z} + c_{eq}\dot{z} + kz + \frac{R_{load}\alpha_N k_t k_e^3 k_g^4 \eta_g^4}{(R_{int}+R_{load})d^4\eta_b^4} z^3 = Y_t \cos \omega t}$

The two dynamic equations are equal and result in the same responses $(\ddot{z}, \dot{z}, z)$. Therefore, the back-EMF generated from the two systems are both equal to $\frac{k_e k_g \eta_g}{d\eta_b}\dot{z}$.

(4) Terminal Current I

Physical Nonlinear Spring System	Synthesized Nonlinear Inductor System
$\frac{k_e k_g \eta_g}{(R_{int} + R_{load})d\eta_b}\dot{z}$	$\boldsymbol{\frac{k_e k_g \eta_g}{(R_{int} + R_{load})d\eta_b}\dot{z} + \frac{R_{load}\alpha_N k_e^3 k_g^3 \eta_g^3}{(R_{int} + R_{load})d^3\eta_b^3} z^3}$

The terminal current is also the current through the DC motor/generator, which differs between the two systems. Part of the current in the second system comes from the nonlinear inductor element.

(5) Terminal Voltage V_{load}

Physical Nonlinear Spring System	Synthesized Nonlinear Inductor System
$\frac{R_{load} k_e k_g \eta_g}{(R_{int} + R_{load})d\eta_b}\dot{z}$	$\boldsymbol{\frac{R_{load} k_e k_g \eta_g}{(R_{int} + R_{load})d\eta_b}\dot{z} - \frac{R_{int} R_{load}\alpha_N k_e^3 k_g^3 \eta_g^3}{(R_{int} + R_{load})d^3\eta_b^3} z^3}$

The terminal voltage is derived from the following relationship referring to the circuit models of the two systems:

$$V_{load} = E_M - I \cdot R_{int} \tag{124}$$

(6) Instantaneous Power Delivered to the Terminal $\boldsymbol{P_{inst}}$

Physical Nonlinear Spring System	Synthesized Nonlinear Inductor System
$\frac{R_{load}k_e^2k_g^2\eta_g^2}{(R_{int}+R_{load})^2d^2\eta_b^2}\dot{z}^2$	$\boldsymbol{\frac{R_{load}k_e^2k_g^2\eta_g^2}{(R_{int}+R_{load})^2d^2\eta_b^2}\dot{z}^2 + \frac{\alpha_N R_{load}(R_{load}-R_{int})k_e^4k_g^4\eta_g^4}{(R_{int}+R_{load})^2d^4\eta_b^4}z^3\dot{z} - \frac{R_{int}R_{load}^2\alpha_N^2k_e^6k_g^6\eta_g^6}{(R_{int}+R_{load})^2d^6\eta_b^6}z^6}$

The instantaneous power delivered to the terminal is the multiplication of terminal voltage by terminal current, which is

$$P_{inst} = V_{load} \cdot I \tag{125}$$

(7) Average Power Delivered to the Terminal $\boldsymbol{P_{avg}}$

Physical Nonlinear Spring System	Synthesized Nonlinear Inductor System
$\frac{R_{load}k_e^2k_g^2\eta_g^2}{2(R_{int}+R_{load})^2d^2\eta_b^2}\omega^2A^2$	$\boldsymbol{\frac{R_{load}k_e^2k_g^2\eta_g^2}{2(R_{int}+R_{load})^2d^2\eta_b^2}\omega^2A^2 - \frac{5R_{int}R_{load}^2\alpha_N^2k_e^6k_g^6\eta_g^6}{16(R_{int}+R_{load})^2d^6\eta_b^6}A^6}$

Assuming the external excitation is $y = Y\cos\omega t$, the steady-state response around the primary resonance can be approximated by performing the perturbation analysis with the method of multiple scales (Nayfeh & Mook, 2008) (Hsieh, Huang, Golnaraghi, & Moallem, 2013), which is

$$\begin{aligned} z &= A\cos(\omega t-\gamma) + \tfrac{1}{32}\epsilon\beta\alpha_N A^3\cos(3\omega t-3\gamma) \\ &= A\cos(\omega t-\gamma) + O(\epsilon) \end{aligned} \tag{126}$$

where A is the amplitude of the dominant approximation term, ϵ is a small parameter and $\epsilon \in (0,1)$, γ is the phase shift of the solution, and β is a constant. The average energy harvested per cycle is

$$P_{avg} = \frac{\omega}{2\pi}\int_{0}^{\frac{2\pi}{\omega}} P_{inst}\, dt \tag{127}$$

Substituting Eq. (126) into the expression of P_{inst} and calculating P_{avg} based on Eq. (127), we obtain the expression of P_{avg}, as shown in the above table. Since the following conditions are always satisfied,

$$\begin{gathered} \frac{R_{load}k_e^2k_g^2\eta_g^2}{2(R_{int}+R_{load})^2d^2\eta_b^2}\omega^2A^2 \geq 0 \\ -\frac{5R_{int}R_{load}^2\alpha_N^2k_e^6k_g^6\eta_g^6}{16(R_{int}+R_{load})^2d^6\eta_b^6}A^6 \leq 0 \end{gathered} \tag{128}$$

The average power harvested from the nonlinear synthesized inductor system is always less than that from the nonlinear physical spring system. The reason is that part of the power ($\frac{5R_{int}R_{load}^2\alpha_N^2k_e^6k_g^6\eta_g^6}{16(R_{int}+R_{load})^2d^6\eta_b^6}A^6$ in average per cycle) is consumed to control the circuit for nonlinear inductor realization.

Therefore, it is necessary to utilize the physical spring instead of electrical elements to provide cubic nonlinearities to the system for the purpose of maximizing energy harvesting.

5.4. Piecewise Linear Spring System

5.4.1. Introduction

Piecewise linear systems were studied as nonlinear isolators to prevent the relative displacement of the vibration system from exceeding an undesirable amount. A Lord controlled equilibrium mount system, shown in Figure 5.8, was developed as a joint research project by the Lord Corporation and the University of Waterloo. The system utilizes the feedback control based on the measurement of relative displacement/velocity sensors to generate the ideal mount that is hard at low frequency and soft at high frequency (Narimani, 2004).

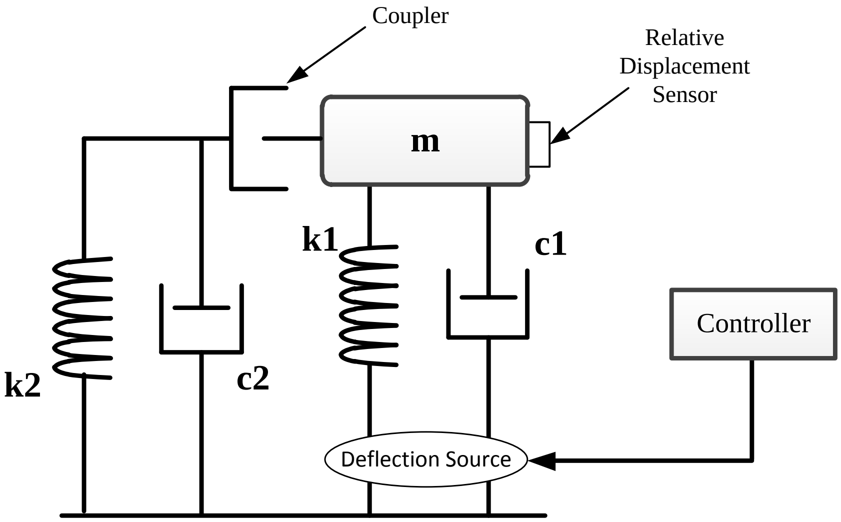

Figure 5.8 Lord controlled equilibrium mount system

(Shaw & Holmes, 1983) studied a 1-DOF periodically forced nonlinear oscillator, where the nonlinearity existed in the stiffness and was piecewise linear changed in slope. Harmonic, subharmonic, and chaotic motions were found to exist and analyzed. Since the nonlinearity was piecewise linear, explicit solutions can be known on each side of the point of discontinuity in slope. The system studied is shown in Figure 5.9.

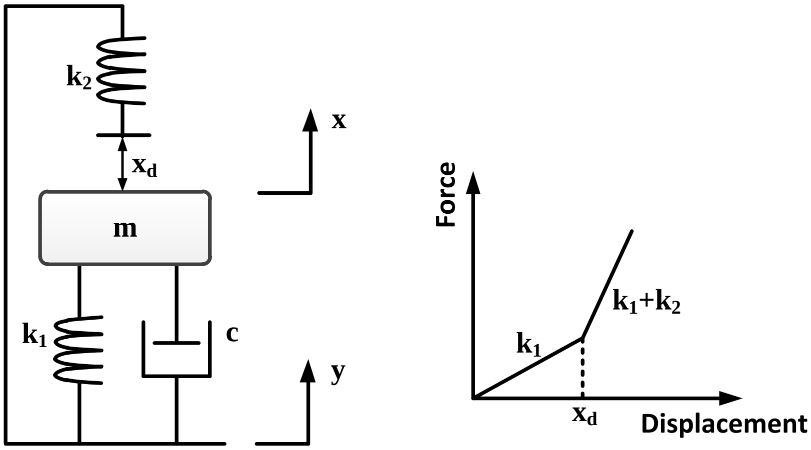

Figure 5.9 1-DOF piecewise linear oscillator and its stiffness property

Inspired by previous investigations on piecewise linear oscillation systems, the work in this chapter presents a nonlinear energy-regenerative system with piecewise linear springs to simulate physical nonlinear springs that provide the cubic nonlinearity, thus improving the bandwidth of power recovery. Figure 5.10 shows the displacement-force curve of the cubic nonlinear spring, with a piecewise linear fit that can be realized by piecewise linear springs. This means that the nonlinear relationship between the displacement and the force is expressed by

$$F = k_N x^3 \tag{129}$$

and can be approximated by the piecewise linear function:

$$F_{est} = \begin{cases} (k_1 + k_2)x - k_2 x_d & x \geq x_d \\ k_1 x & -x_d < x < x_d \\ (k_1 + k_2)x + k_2 x_d & x \leq x_d \end{cases} \tag{130}$$

where k_1, k_2, and x_d are the stiffness of the first, second spring, and the clearance between the second spring and sprung mass. Their values can be determined by minimizing the mean-square error, MSE(F_{est}), between the cubic curve and piecewise linear fitting curve, given k_N, x, F, and constraint x_{max}, which is the maximum displacement the system can achieve.

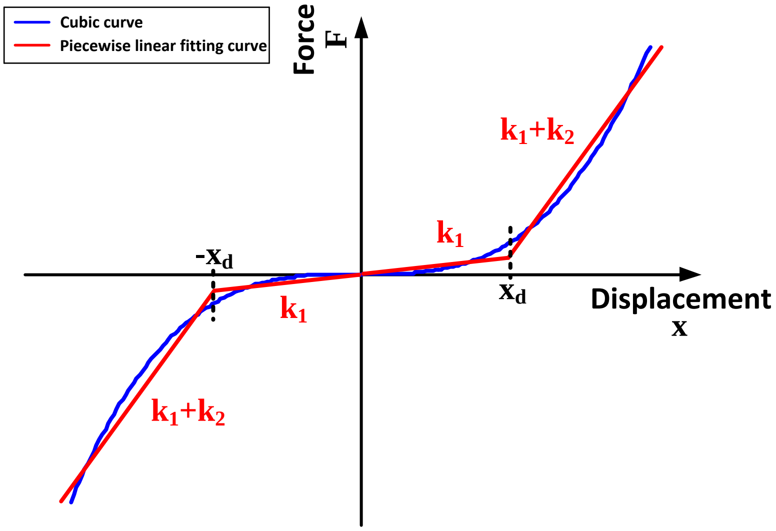

Figure 5.10 Cubic curve and piecewise linear fitting curve

5.4.2. System Description and Modeling

Figure 5.11 illustrates the mechanical model of the nonlinear regenerative suspension system that was considered. Based on the previous proposed model in Figure 2.1, a second spring set was installed and will interact if the relative motion of the sprung mass, with respect to the base excitation, exceeds the clearance Δ. When the amplitude of the relative motion is smaller than the clearance Δ, the system oscillates at the first stage, where the overall stiffness is equal to k_1. When the amplitude of the relative motion exceeds the clearance Δ, the system oscillates at the second stage, where the overall stiffness is equal to $k_1 + k_2$. The stiffness of the system is illustrated in Figure 5.12.

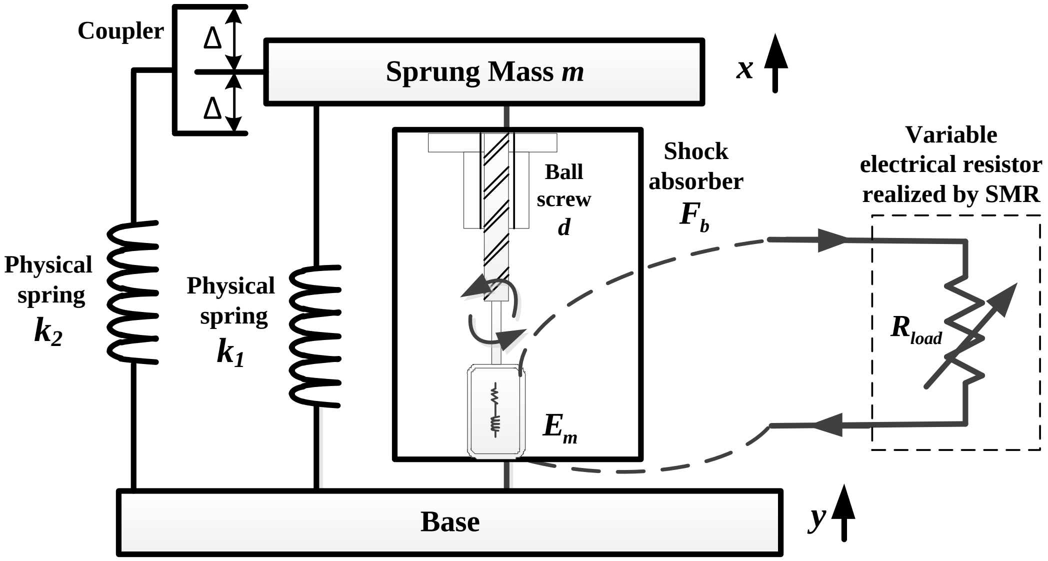

Figure 5.11 Mechanical model of the nonlinear regenerative suspension system

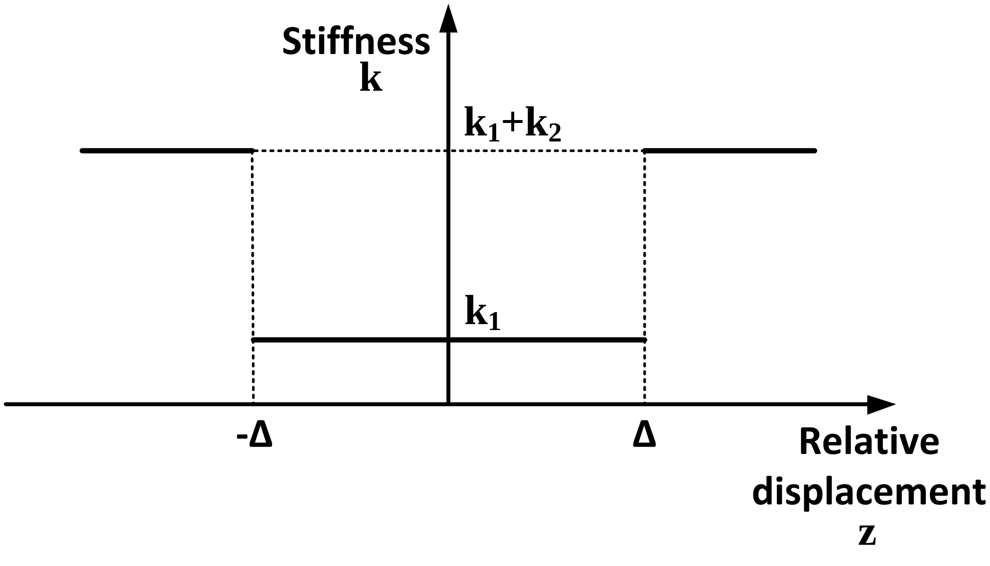

Figure 5.12 Stiffness of the system in terms of the relative displacement

Based on the dynamic modeling in Chapter 2, the governing equation of the system in Figure 5.11 is expressed as

$$m_{eq}\ddot{z} + c_{eq}\dot{z} + g(z) = -m\ddot{y} \tag{131}$$

where

$$g(z) = \begin{cases} (k_1 + k_2)z - k_2\Delta & z \geq \Delta \\ k_1 z & -\Delta < z < \Delta \\ (k_1 + k_2)z + k_2\Delta & z \leq -\Delta \end{cases} \tag{132}$$

The other parameters, m_{eq} and c_{eq}, are presented in Table 5.1.

Similar to Section 5.2.2, the dynamic equation of the nonlinear suspension system, as shown in Eq. (131), can be rewritten as

$$\ddot{z} + 2\zeta_1\omega_1\dot{z} + g_1(z) = -\frac{m}{m_{eq}}\ddot{y} \tag{133}$$

where

$$g_1(z) = \begin{cases} \omega_{12}^2 z - \omega_2^2\Delta & z \geq \Delta \\ \omega_1^2 z & -\Delta < z < \Delta \\ \omega_{12}^2 z + \omega_2^2\Delta & z \leq -\Delta \end{cases}$$
$$\omega_1 = \sqrt{\frac{k_1}{m_{eq}}} \quad \omega_2 = \sqrt{\frac{k_2}{m_{eq}}} \quad \omega_{12} = \sqrt{\frac{k_1 + k_2}{m_{eq}}} \quad \zeta_1 = \frac{c_{eq}}{2\sqrt{m_{eq}k_1}} \tag{134}$$

In order to approximate the system response by using the perturbation method, we perform the nondimensionalization of the dynamic equation with respect to the excitation displacement Y and dimensionless time $T = \frac{1}{\omega_1}$. Assuming the excitation is in the harmonic form $\mathrm{y} = \mathrm{Y}\sin\omega\mathrm{t}$, let

$$u = \frac{z}{Y} \quad \gamma = \omega_1 t \quad \delta = \frac{\Delta}{Y} \quad \omega_{01} = \frac{\omega}{\omega_1} \tag{135}$$

Therefore, the dynamic equation (133) is rearranged as

$$u'' + 2\zeta_1 u' + u + g_2(u) = \rho\omega_{01}^2 \sin \omega_{01}\gamma \tag{136}$$

where

$$g_2(u) = \begin{cases} \omega_{21}^2 u - \omega_{21}^2 \delta & u \geq \delta \\ 0 & -\delta < u < \delta \\ \omega_{21}^2 u + \omega_{21}^2 \delta & u \leq -\delta \end{cases}$$
$$u'' = \frac{d^2u}{d\gamma^2} \quad u' = \frac{du}{d\gamma} \quad \rho = \frac{m}{m_{eq}} \quad \omega_{21} = \frac{\omega_2}{\omega_1} \tag{137}$$

When the relative displacement stays within the clearance (i.e., $|u| < |\delta|$), the system operates as a linear system based on forced excitation; when the relative displacement goes beyond the clearance (i.e., $|u| \geq |\delta|$), the system acts as another linear system with a combined spring constant and an offset on the excitation by $\pm\omega^*\delta$.

5.4.3. *Perturbation Analysis*

Among the different methods used in perturbation analysis, the method of averaging is the only one that is applicable when the system contains hard nonlinearity because it transforms nonlinearities to slow and fast varying parameters (Nayfeh, 2011).

We are trying to find out the first-order approximation of the solution of Eq. (136), which is considered to be

$$u = a \sin \varphi = a \sin(\omega_{01}\gamma + \beta) \tag{138}$$

It follows from Eq. (138) that

$$u' = a\omega_{01}\cos(\omega_{01}\gamma + \beta) = a\omega_{01}\cos\varphi \tag{139}$$

Using the method of averaging, we assume that parameters a and β are slowly varying functions of γ; that is, $a = a(\gamma)$ and $\beta = \beta(\gamma)$. In this case, by differentiating (138), we have

$$u' = a\omega_{01}\cos\varphi + a'\sin\varphi + a\beta'\cos\varphi \tag{140}$$

Comparing Eq. (139) and (140) implies

$$a'\sin\varphi + a\beta'\cos\varphi = 0 \tag{141}$$

By differentiating (139), we have

$$u'' = a'\omega_{01}\cos\varphi - a\omega_{01}^2\sin\varphi - a\beta'\omega_{01}\sin\varphi \tag{142}$$

Substituting Eq. (142), (139), and (138) into (136) yields

$$a'\omega_{01}\cos\varphi - a\beta'\omega_{01}\sin\varphi = a(\omega_{01}^2 - 1)\sin\varphi - 2\zeta_1 a\omega_{01}\cos\varphi + \\ \rho\omega_{01}^2\sin(\varphi - \beta) - g_2(u) \tag{143}$$

Eq. (143) can be simplified by substituting $\sin(\varphi - \beta) = \sin\varphi\cos\beta - \sin\beta\cos\varphi$,

$$a'\cos\varphi - a\beta'\sin\varphi = \left[\frac{a}{\omega_{01}}(\omega_{01}^2 - 1) + \rho\omega_{01}\cos\beta\right]\sin\varphi - \\ (2\zeta_1 a + \rho\omega_{01}\sin\beta)\cos\varphi - \frac{1}{\omega_{01}}g_2(u) \tag{144}$$

Solving Eq. (141) and (144) leads to

$$\begin{aligned} a' = &\left[\frac{a}{\omega_{01}}(\omega_{01}^2 - 1) + \rho\omega_{01}\cos\beta\right]\sin\varphi\cos\varphi \\ &- (2\zeta_1 a + \rho\omega_{01}\sin\beta)\cos^2\varphi - \frac{1}{\omega_{01}}g_2(u)\cos\varphi \end{aligned} \tag{145}$$

$$\begin{aligned} a\beta' = &\left[-\frac{a}{\omega_{01}}(\omega_{01}^2 - 1) - \rho\omega_{01}\cos\beta\right]\sin^2\varphi \\ &+ (2\zeta_1 a + \rho\omega_{01}\sin\beta)\sin\varphi\cos\varphi + \frac{1}{\omega_{01}}g_2(u)\sin\varphi \end{aligned} \tag{146}$$

Since a and β are assumed to be slowly varying, averages of a' and β' may remain constant over a period [0, 2π], so that

$$\begin{aligned} a' = \frac{1}{2\pi}\int_0^{2\pi}&\left\{\left[\frac{a}{\omega_{01}}(\omega_{01}^2 - 1) + \rho\omega_{01}\cos\beta\right]\sin\varphi\cos\varphi\right. \\ &\left.- (2\zeta_1 a + \rho\omega_{01}\sin\beta)\cos^2\varphi - \frac{1}{\omega_{01}}g_3(\varphi)\cos\varphi\right\}\mathrm{d}\varphi \end{aligned} \tag{147}$$

$$\begin{aligned} a\beta' = \frac{1}{2\pi}\int_0^{2\pi}&\left\{\left[-\frac{a}{\omega_{01}}(\omega_{01}^2 - 1) - \rho\omega_{01}\cos\beta\right]\sin^2\varphi\right. \\ &+ (2\zeta_1 a + \rho\omega_{01}\sin\beta)\sin\varphi\cos\varphi \\ &\left.+ \frac{1}{\omega_{01}}g_3(\varphi)\sin\varphi\right\}\mathrm{d}\varphi \end{aligned} \tag{148}$$

where

$$g_3(\varphi) = \begin{cases} \omega_{21}^2 a(\sin\varphi - \sin\varphi_0) & \varphi_0 \le \varphi \le \pi - \varphi_0 \\ 0 & \text{other domain} \\ \omega_{21}^2 a(\sin\varphi + \sin\varphi_0) & \pi + \varphi_0 \le \varphi \le 2\pi - \varphi_0 \end{cases} \tag{149}$$

$$\varphi_0 = \sin^{-1}\left(\frac{\delta}{a}\right) \tag{150}$$

$\varphi_0 \in [0, \pi/2]$ since $0 < \delta/a \le 1$. Performing the integration in Eq. (147) and (148), we get

$$a' = -\left(\zeta_1 a + \frac{1}{2}\rho\omega_{01}\sin\beta\right) \tag{151}$$

$$\begin{aligned} a\beta' = -\frac{1}{2}\left[\frac{a}{\omega_{01}}(\omega_{01}^2 - 1) + \rho\omega_{01}\cos\beta\right] \\ + \frac{\omega_{21}^2 a}{2\pi\omega_{01}}[\pi - 2\varphi_0 - \sin(2\varphi_0)] \end{aligned} \tag{152}$$

Considering that when the steady-state motions of the system occur, the time derivatives of a and β are both zero, which means $a' = \beta' = 0$. Thus, Eq. (151) and (152) lead to

$$\pi\rho\omega_{01}^2 \sin\beta = -2\zeta_1 a\pi\omega_{01} \tag{153}$$

$$\pi\rho\omega_{01}^2 \cos\beta = -a\pi\omega_{01}^2 + a\pi(\omega_{21}^2 + 1) - 2a\omega_{21}^2\varphi_0 - 2\delta\omega_{21}^2\cos\varphi_0 \tag{154}$$

Squaring and adding the above two equations, we obtain the solution as

$$\omega_{01} = \left\{\frac{1}{2H_3}\left[-H_4 \pm (H_4^2 - 4H_3H_5)^{1/2}\right]\right\}^{1/2} \tag{155}$$

where

$$H_1 = \pi\omega_{21}^2 + \pi - 2\omega_{21}^2\varphi_0 \tag{156}$$

$$H_2 = -2\delta\omega_{21}^2 \cos\varphi_0 \tag{157}$$

$$H_3 = (a^2 - \rho^2)\pi^2 \tag{158}$$

$$H_4 = (4\zeta_1^2\pi^2 - 2\pi H_1)a^2 - 2\pi H_2 a \tag{159}$$

$$H_5 = (aH_1 + H_2)^2 \tag{160}$$

Since ω_{01} is a positive real number, it should always satisfy that

$$H_4^2 - 4H_3H_5 \geq 0 \tag{161}$$

and

$$H_3\left[-H_4 \pm (H_4^2 - 4H_3H_5)^{1/2}\right] > 0 \tag{162}$$

Eq. (155) is an implicit function of frequency response that describes the relationship between dimensionless amplitude and excitation frequency. We can also obtain the phase function using Eq. (153) and (154), which is

$$\beta = \tan^{-1}\left(\frac{2\zeta_1 a\pi\omega_{01}}{a\pi\omega_{01}^2 - aH_1 - H_2}\right) \tag{163}$$

(1) Stability Analysis

To investigate the stability of the steady-state solution, we derived the Jacobian matrix of Eq. (151) and (152) at singular points (a_0, β_0)

$$J = \begin{bmatrix} \left.\frac{\partial a'}{\partial a}\right|_{a_0} & \left.\frac{\partial a'}{\partial \beta}\right|_{\beta_0} \\ \left.\frac{\partial \beta'}{\partial a}\right|_{a_0} & \left.\frac{\partial \beta'}{\partial \beta}\right|_{\beta_0} \end{bmatrix} = \begin{bmatrix} -\zeta_1 & a_0 p \\ -\frac{1}{a_0}(p+q) & -\zeta_1 \end{bmatrix} \tag{164}$$

where

$$p = -\frac{\omega_{21}^2 + 1}{2\omega_{01}} + \frac{\omega_{01}}{2} + \frac{\omega_{21}^2}{\pi\omega_{01}}\left[\sin^{-1}\left(\frac{\delta}{a_0}\right) + \frac{\delta}{a_0}\left(1 - \frac{\delta^2}{a_0^2}\right)^{\frac{1}{2}}\right] \tag{165}$$

$$q = \frac{\omega_{21}^2}{\pi\omega_{01}}\left[-\frac{\delta}{a_0}\left(1 - \frac{\delta^2}{a_0^2}\right)^{-\frac{1}{2}} - \frac{\delta}{a_0}\left(1 - \frac{\delta^2}{a_0^2}\right)^{\frac{1}{2}} + \frac{\delta^3}{a_0^3}\left(1 - \frac{\delta^2}{a_0^2}\right)^{-\frac{1}{2}}\right] \tag{166}$$

By studying the characteristics of eigenvalues of the Jacobian matrix, it always satisfies that the trace of the Jacobian matrix, $\mathrm{tr}(J) < 0$. Therefore, the steady-state motions are unstable when the determinant of the Jacobian matrix, $\det(J) < 0$. That is

$$\zeta_1^2 + p(p+q) < 0 \tag{167}$$

Otherwise, the steady-state motions satisfying that $\det(J) > 0$ are stable.

(2) Frequency Responses

Frequency-response curves of the amplitude and phase of the system's relative displacement can be obtained analytically by solving Eq. (155) and (163), given that $Y = 7\,mm$, $\Delta = 4\,mm$, $R_{\text{load}} = 200\,\Omega$, $k_1 = 25288\,N/m$, and $k_2 = 116109\,N/m$. The curves are compared with responses of the linear system and plotted in Figure 5.13.

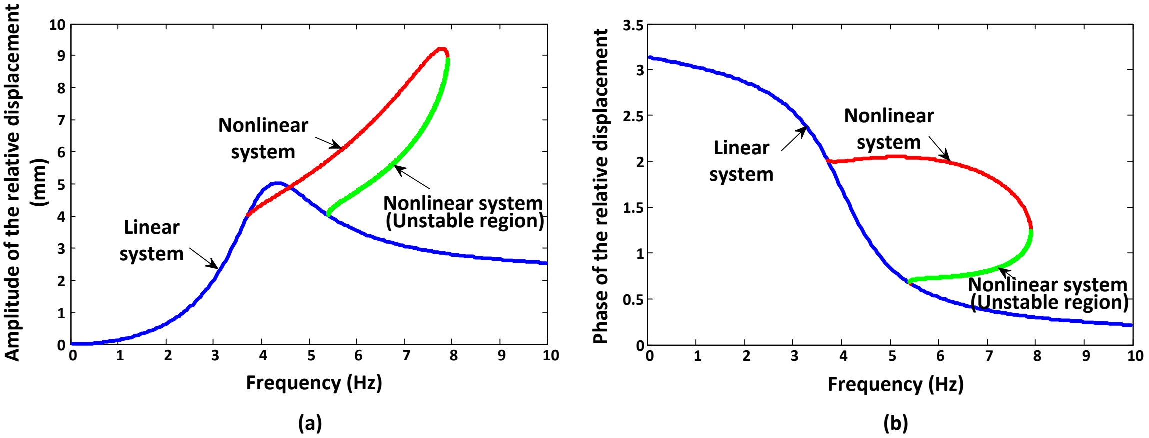

Figure 5.13 **The analytical frequency-response curves of the relative displacement: (a) amplitude and (b) phase**

Similar to the frequency-response curves of the system with the nonlinear variable inductor, the amplitude curve is bent and the phase curve is distorted due to the effect of the piecewise linear stiffness. The extent of bending is dependent on the value of k_1 and k_2. The portion in green indicates the unstable states that meet the condition in Eq. (167). Therefore, the steady-state solutions corresponding to the unstable portion cannot be realized by the system.

In the region where unstable steady-state solutions exist, there are two stable steady-state solutions: One is nonlinear response, and the other is linear response. Therefore, two possible stable motions can be observed and the status is determined by the initial condition. Due to the existence of multiple solutions, a jump phenomenon occurs when the frequency of the excitation is slowly varied up or down. Figure 5.14 shows the amplitude and phase of the harmonic response by performing the numerical simulation based on Eq. (151) and (152). Blue solid curves indicate the trajectories when the frequency sweeps up and red dot curves indicate the trajectories when the frequency sweeps down. Arrows in each figure demonstrate the direction of the motion and jump.

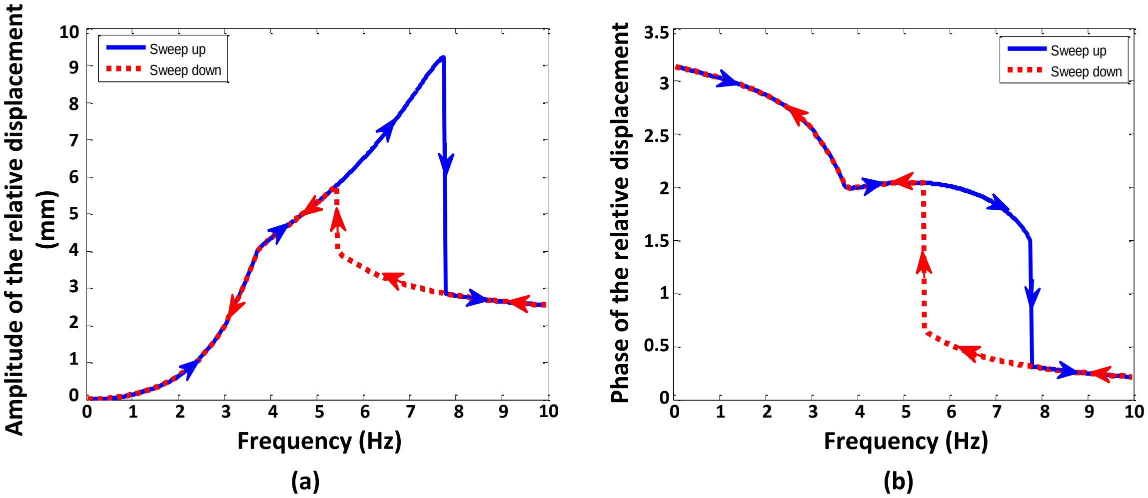

(a) (b)

Figure 5.14 Jump phenomena of relative displacement curves: (a) amplitude and (b) phase

5.4.4. Power Generation and Bandwidth Analysis

Assuming excitation $y = Y\sin\omega t$ and period of the cycle $T = 2\pi/\omega$, the average power flow per cycle is calculated according to Eq. (31)

$$P_{avg} = \frac{1}{2}\left(c - \frac{c^2 d^2 \eta_b^2 R_{int}}{k_e k_t {k_g}^2 \eta_g^2}\right)\omega^2 Y^2 a^2 \tag{168}$$

Furthermore, the average power can be nondimensionalized as

$$\hat{P}_{avg} = \left|\frac{P_{avg}}{\dot{y}^2}\right| = \frac{1}{2}\left(c - \frac{c^2 d^2 \eta_b^2 R_{int}}{k_e k_t {k_g}^2 \eta_g^2}\right) a^2 \tag{169}$$

By solving Eq. (155) and (169), the frequency-response curves of power generation can be obtained and plotted in Figure 5.15. Based on this, we can define the bandwidth of the proposed system and a figure of merit (FoM) for energy harvesting capability.

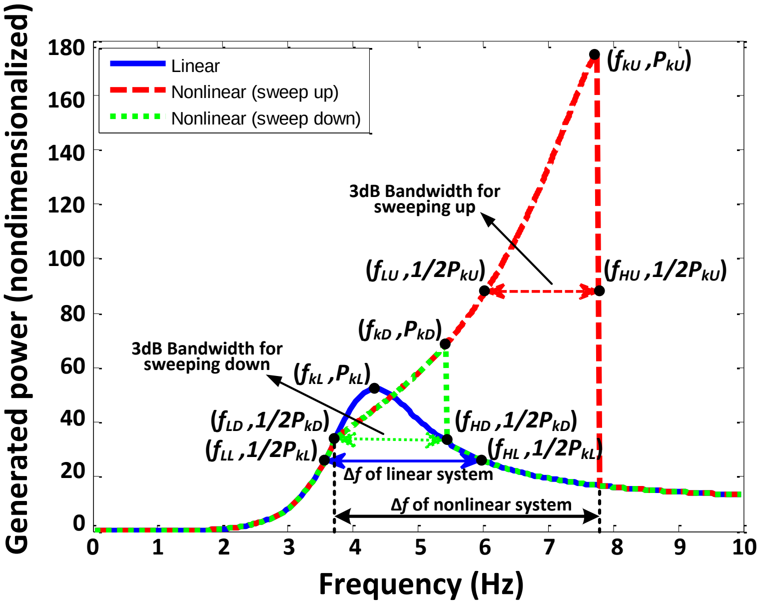

Figure 5.15 Frequency-response curve of power generation and bandwidth

The operation bandwidth of a wideband energy harvester was introduced by (Liu, Badel, Formosa, & Wu, 2015). Due to the characteristics of the piecewise energy harvester, its bandwidth needs to be analyzed for the frequency sweep up and sweep down, respectively. As shown in Figure 5.15, the 3 dB bandwidth for sweeping up can be found from the peak-power point (f_{kU}, P_{kU}) and two half peak-power points $(f_{LU}, 1/2P_{kU})$ and $(f_{HU}, 1/2P_{kU})$. Similarly, the bandwidth for sweeping down can be obtained from three corresponding parameters (f_{kD}, P_{kD}), $(f_{LD}, 1/2P_{kD})$, and $(f_{HD}, 1/2P_{kD})$. Therefore, the total operation bandwidth is defined to cover the favorable range for both sweeping up and sweeping down responses, which is

$$\Delta f_{non} = f_{HU} - f_{LD} \tag{170}$$

The bandwidth of the linear system is also depicted based on three points (f_{kL}, P_{kL}), $(f_{LL}, 1/2P_{kL})$, and $(f_{HL}, 1/2P_{kL})$ and is expressed as $\Delta f_{lin} = f_{HL} - f_{LL}$.

To examine the energy harvesting capability of the proposed system, a new FoM is introduced based on two critical factors: operation bandwidth, Δf, as described in Eq. (170); and expectation of power generation across the whole excited frequency range, E_P, which can be expressed as

$$E_{p\_non} = \frac{1}{f_{high} - f_{low}} \int_{f_{low}}^{f_{high}} P_{avg\_U}(f) \cdot p_U(f) + P_{avg\_D}(f) \cdot p_D(f) \mathrm{d}f \tag{171}$$

where f_{high} and f_{low} are upper and lower bounds of the excitation frequency. $P_{avg\_U}(f)$ and $P_{avg\_D}(f)$ are the average power generation at a certain frequency for sweeping up and down situations, respectively. $p_U(f)$ and $p_D(f)$ denote the probability to obtain a response in frequency sweeping up and down, which satisfy that

$$p_U(f) + p_D(f) = 1 \tag{172}$$

Therefore, the energy harvesting FoM can be defined as

$$\mathrm{FoM}_{ENG} = E_p \cdot \Delta f \tag{173}$$

FoM_{ENG} provides a systematic methodology to evaluate the system's energy harvesting performance. It also implies that the sum of the average power generation and the ratio of the operation bandwidth to the whole frequency range make a coupling contribution to the evaluation.

5.4.5. Experimental Setup and Test Results

To validate the analytical results from the previous theoretical analysis by the perturbation method, a prototype was fabricated and an experimental test-bed was developed to test its nonlinearity and performance.

(1) Prototype Design and Test-Bed

Based on the prototype, as shown in Figure 2.2, a second pair of die springs with higher stiffness (i.e., 116109 N/m) was installed on top of the first pair of springs and a pair of couplers was set up around the sprung mass, as depicted in Figure 5.16. Figure 5.17 indicates the test-bed setup based on the designed prototype. All the other hardware descriptions are mentioned in Chapter 2.4, and the values of corresponding parameters are listed in Table 2.1.

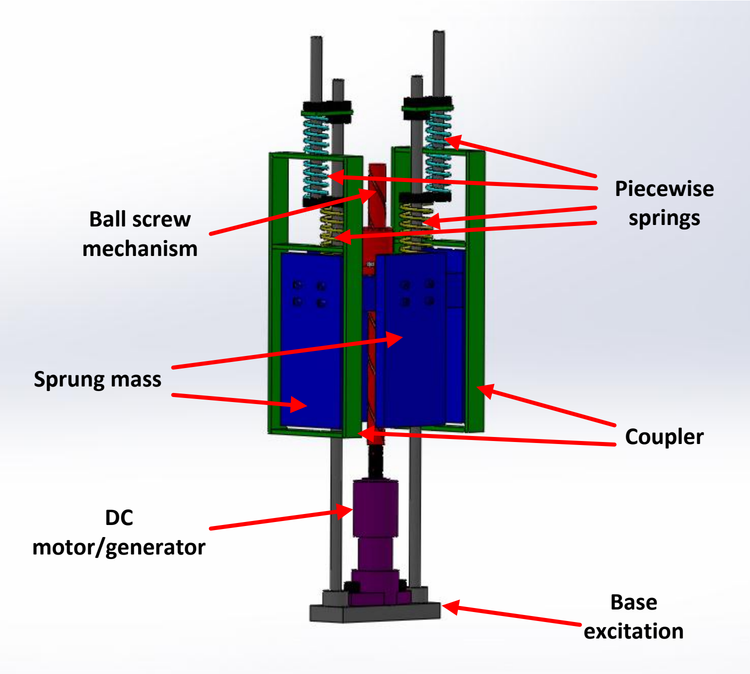

Figure 5.16 CAD prototype of the regenerative suspension system with piecewise springs

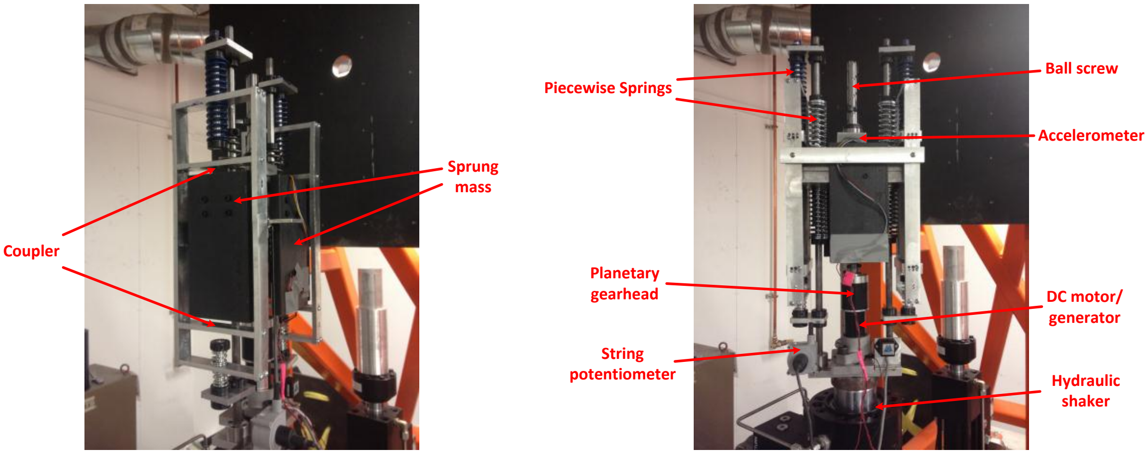

Figure 5.17 Experimental test setup for the regenerative suspension system with piecewise springs

(2) Frequency Responses

This experiment was performed to study frequency responses of the system based on harmonic excitations and compare its energy harvesting performance with that of the linear system. After applying a sweeping sinusoidal excitation slowly increased from 2 Hz to 10 Hz and also decreased from 10 Hz to 2 Hz, the responses of the system were measured and analyzed. During the test, the amplitude of the excitation was held constant at 7 mm, and the clearance between the coupler and sprung mass was 4 mm. The value of the load resistor was chosen as 490 Ω. At each frequency step, the amplitude of the relative displacement was captured by the string potentiometer, the absolute acceleration of the sprung mass was measured by the accelerometer, and the terminal voltage of the load resistant was read and recorded by the dSPACE DS1103 system. The generated power was calculated by the load resistance and its terminal voltage at different frequencies. Figure 5.18 shows the frequency responses of the system, where experimental results are indicated by dotted lines compared to the numerical simulation results depicted by solid lines.

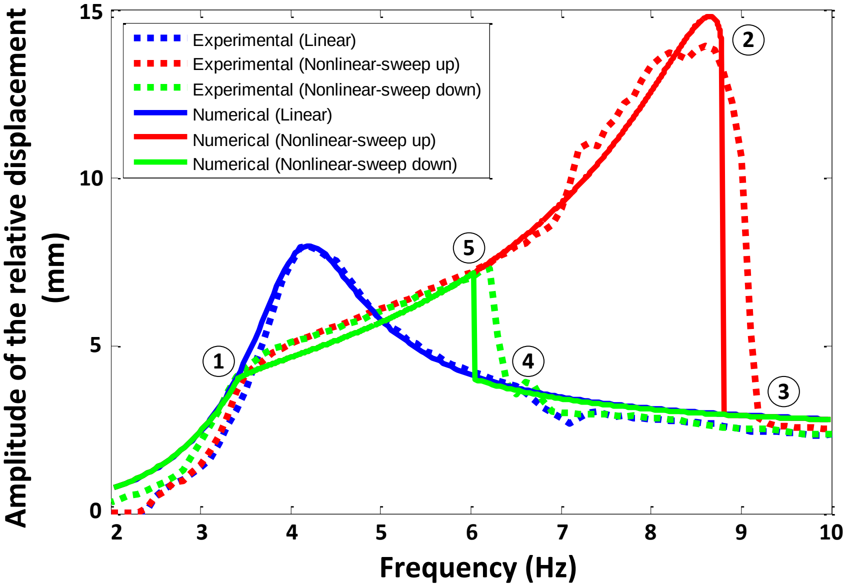

(a)

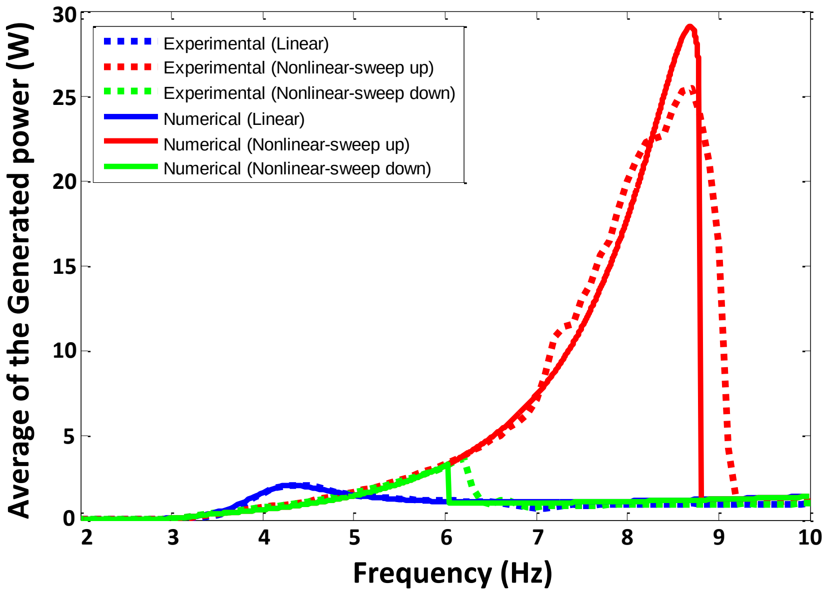

(b)

Figure 5.18 Experimental frequency responses of the regenerative suspension system with piecewise springs: (a) relative displacement and (b) generated power

Referring to Figure 5.18 (a), when the excitation frequency increases, the relative displacement increases the same as the linear system until the moving mass hits the couplers at point 1. From this moment, the increasing rate changes, and the amplitude keeps increasing until it reaches point 2, where the amplitude suddenly and dramatically decreases to point 3. Then the system becomes linear, and no more rattling occurs.

As the excitation frequency decreases, the system acts as linear from point 3 to point 4, where the moving mass hits the couplers again and the rattling begins. The amplitude of the relative displacement rapidly increases to point 5 and begins to decrease to point 1, where the mass stops hitting the couplers and the system resumes as linear.

From the results, it can be seen that the regenerative suspension system with piecewise springs provides a jump phenomenon, which is a typical feature of the cubic nonlinearity, as shown in Figure 5.6. Therefore, the bandwidth of the regenerative suspension system is extended by utilizing the piecewise linear springs.

The comparison between the linear and nonlinear systems is indicated in Figure 5.19. The results reveal the advantages and disadvantages of the nonlinear suspension system. By using piecewise springs, the system's response bandwidth is widened, thus improving its power generation capability. But the relative displacement and absolute acceleration are both increased, which means the control performance of the system is sacrificed as a result. The trade-off between dynamic control and power generation should be considered when applying the nonlinear technique.

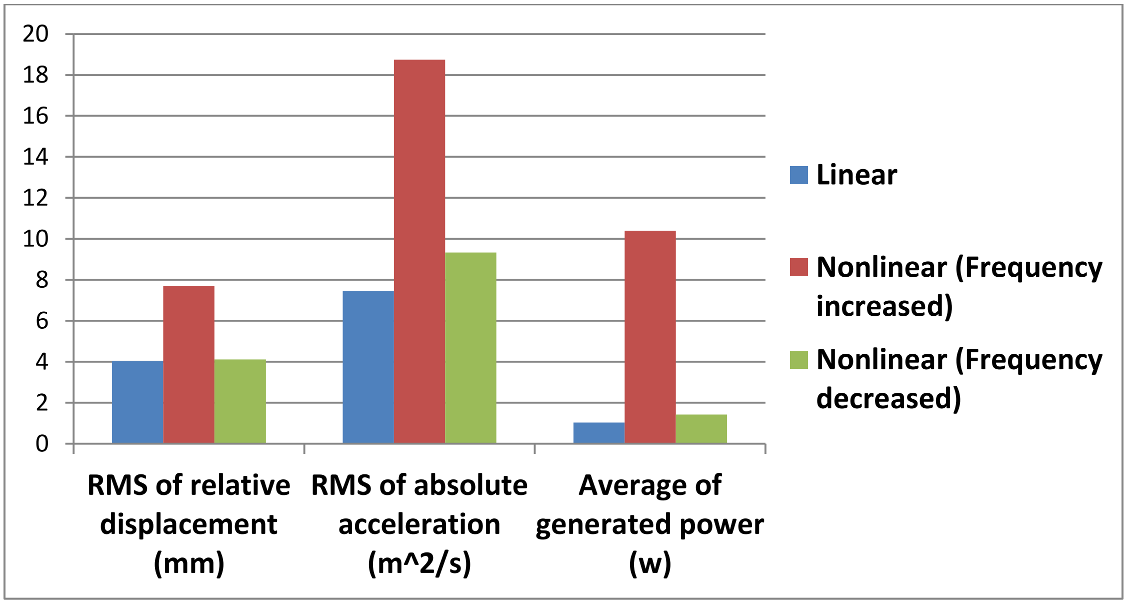

Figure 5.19 Comparison between linear and nonlinear systems

(3) Power Generation Efficiency

According to Section 2.3.4, mechanical efficiency, electrical efficiency, and overall efficiency of power generation are defined. The experimental results from 4 Hz to 8 Hz where nonlinearities exist were obtained, as displayed in Figure 5.20.

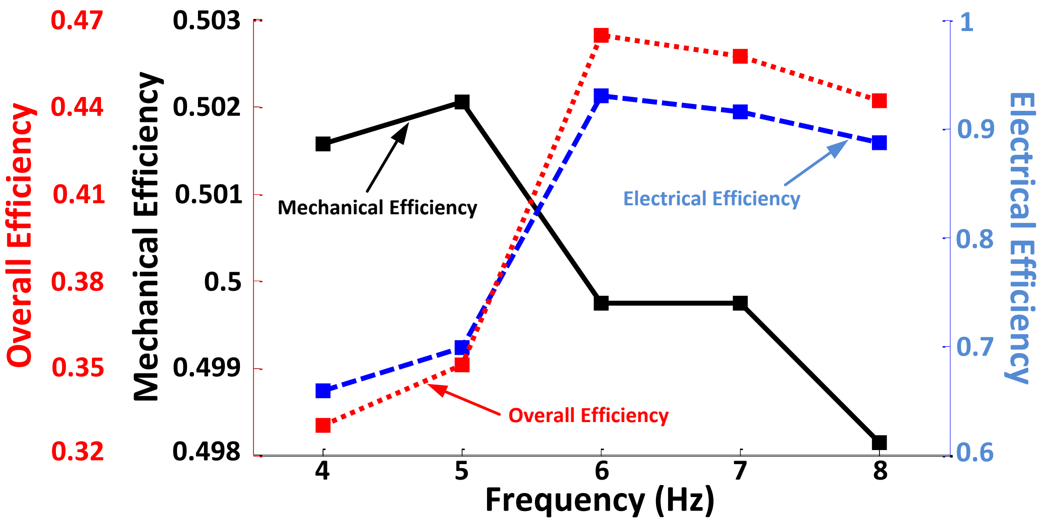

Figure 5.20 Mechanical, electrical, and overall efficiency of power generation

Results show that the mechanical efficiency maintains at around 50% and the electrical efficiency ranges from 66% to 93%. The overall efficiency of power generation was obtained within the range of 33% to 46%, and the highest efficiency was obtained around 6 Hz.

(4) Comparison of FoM for energy harvesting performance

FoMs of the proposed energy harvesting system and linear system were calculated, and corresponding values are listed in Table 5.2, along with parameters Δf and E_p. It is assumed that the probability of frequency increase and frequency decrease is equal, which means $p_U(f) = p_D(f) = 1/2$.

Table 5.2 Comparison of FoMs for linear and nonlinear energy harvesters

	$\Delta\mathrm{f}$ (Hz)	$\mathrm{E_p}$ (W)	$\mathrm{FoM_{ENG}}$ (W·Hz)
Linear system	1.39	1.03	1.432
Nonlinear system	4.40	5.91	26.004

Figure 5.18 and Table 5.2 confirm that both the amplitude of power generation across the excitation frequency range and operation bandwidth are

increased due to the piecewise linear stiffness. Thus, the FoM of the system's energy harvesting performance is improved significantly.

To analyze system parameters' effect on FoM for energy harvesting, we obtained frequency responses of the energy harvester based on different values of the electrical load resistor (i.e., R_{load}) and coupler clearance (i.e., Δ). The corresponding FoMs were calculated and compared, as shown in Figure 5.21 and Figure 5.22.

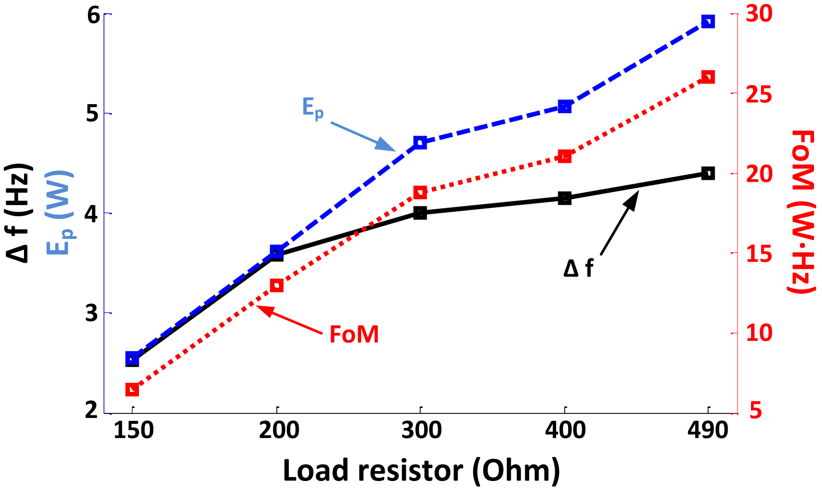

Figure 5.21 FoM for different values of load resistor

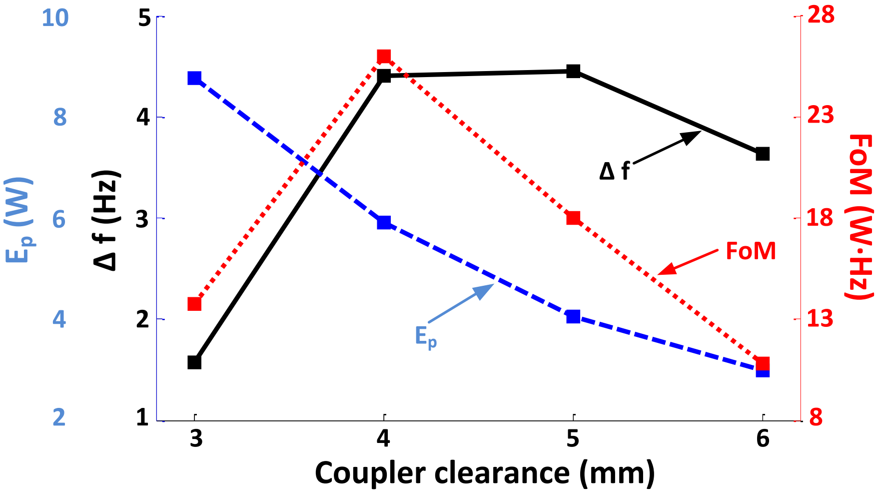

Figure 5.22 FoM for different values of coupler clearance

By varying R_{load} and Δ, we find some characteristics of the proposed energy harvester as follows:

- Higher load resistor provides larger bandwidth and higher average of power generation, thus increasing the FoM for energy harvesting;
- Increasing coupler clearance improves bandwidth but decreases average of power generation. There is an optimum value of clearance setup to obtain the best FoM for energy harvesting.

(5) Experimental Results of Stochastic Excitation

The system was also examined by applying a stochastic excitation which was generated as a standard road roughness in the time domain to simulate a City situation (See Table 4.1). The excitation profile is shown in Figure 5.23.

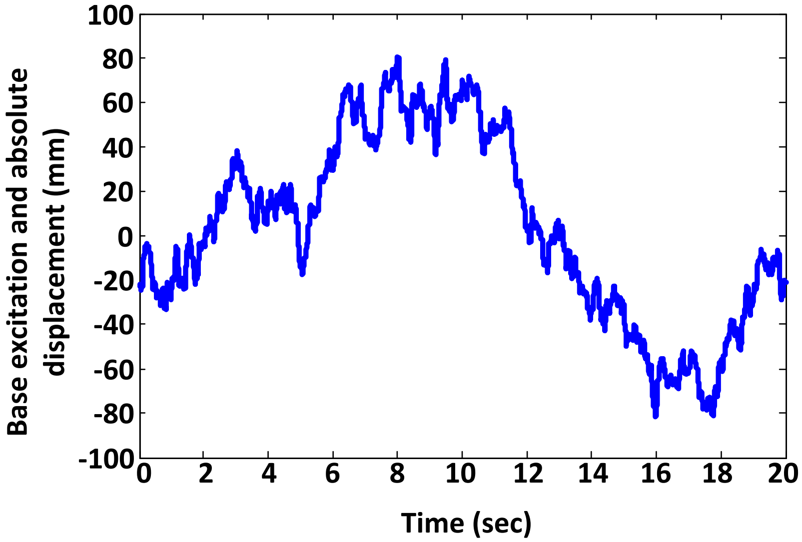

Figure 5.23 Stochastic road profile to simulate a City situation

Figure 5.24 through Figure 5.26 show the system responses, including relative displacement, absolute acceleration, and generated power in the time domain, compared with the linear system responses. The results show that the control of relative displacement and the power generation capability both improved, while the control of absolute acceleration declined. Therefore, from the energy harvesting point of view, piecewise linear springs improve the system's performance and can be a physical alternative to the nonlinear variable inductor. On the other hand, it should be noted that the system's control performance is sacrificed by utilizing piecewise linear springs so it must be maintained at an acceptable level. The balance between dynamic control and power generation may vary in different driving situations and depending on the user's demand.

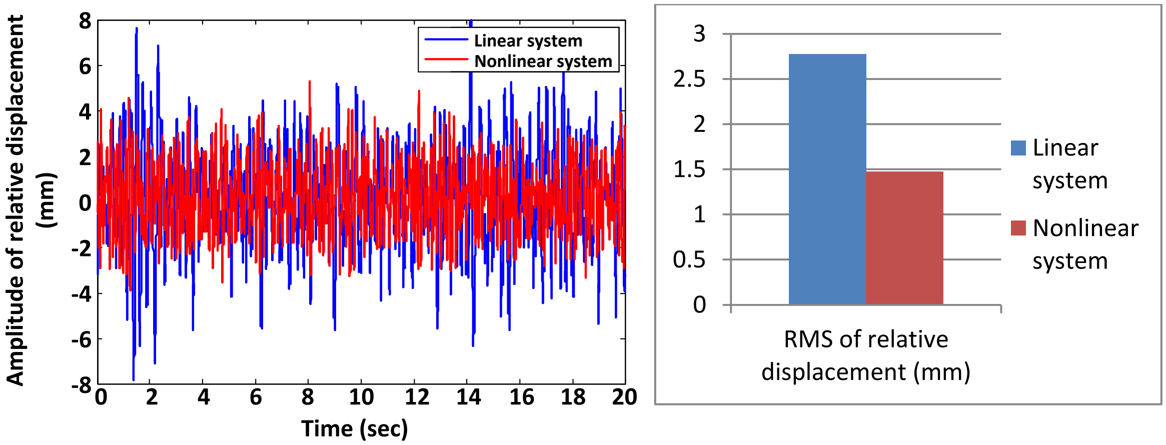

(a) (b)

Figure 5.24 Relative displacement of linear and nonlinear systems

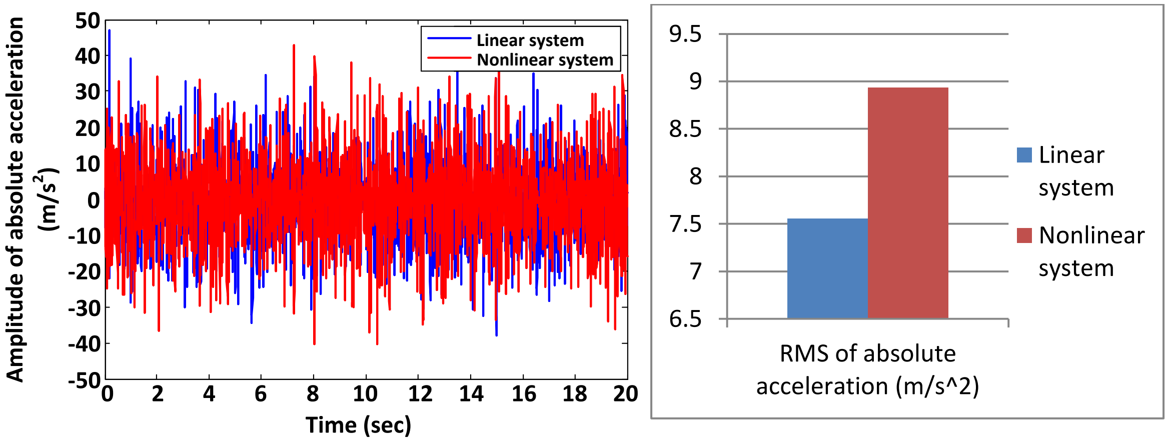

(a) (b)

Figure 5.25 Absolute acceleration of linear and nonlinear systems

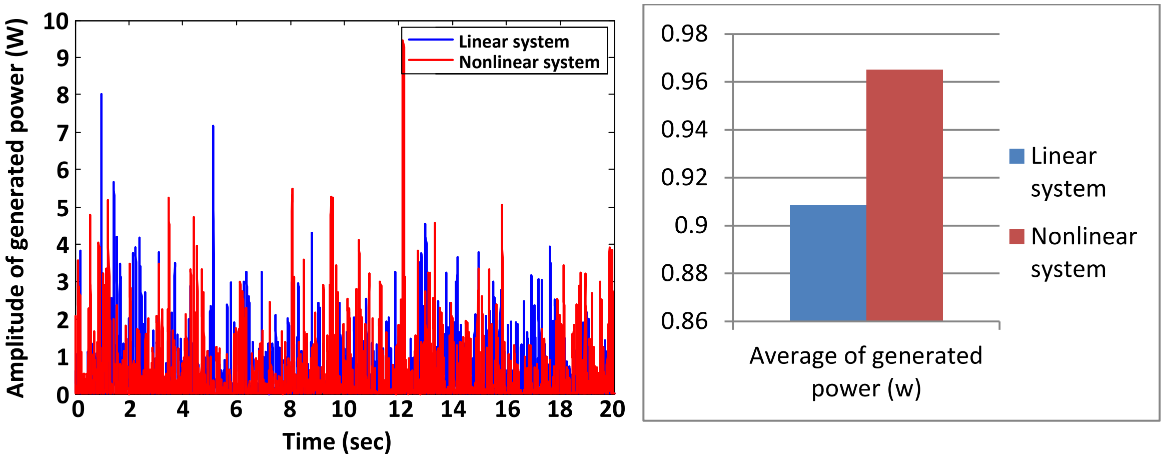

(a) **(b)**

Figure 5.26 Generated power of of linear and nonlinear systems

5.5. Conclusion

In this chapter, a bandwidth enhancement for extending the operational frequency region of the regenerative suspension system was studied. The technique utilized nonlinearities from piecewise stiffness to bend the frequency-response curve and resulted in a wider bandwidth. To realize the nonlinearities, two methods utilizing physical components or electronics circuit were analyzed by using perturbation methods and compared in terms of power regeneration. A piecewise linear spring mechanism was designed to supply cubic-like nonlinearities to the suspension system. The closed-form analytical solution for the system's frequency response was derived. A corresponding prototype was fabricated and its performance was evaluated in terms of a new FoM. Test results indicated that the bandwidth of the proposed suspension system was around 300% wider than that of the traditional linear system. Furthermore, effects of different parameters on the system's power regeneration performance were investigated.

Besides the improvement on the energy regeneration, some improvements on system's dynamic control should also be taken into consideration. Compared to the passive suspension system, the semi-active suspension system can provide a better control performance, so a study on a self-powered regenerative Skyhook control is demonstrated in the next chapter.

Chapter 6.

Regenerative Skyhook Control for the Hybrid Vehicle Suspension System

In this chapter, the hybrid suspension system, a self-powered suspension system with capabilities of energy harvesting and active/semi-active control, is presented. A modified Skyhook control strategy is designed to offer better control performance while recapturing energy from the excitation input. Two operational modes, including regeneration mode and control mode, are studied. An intelligent strategy to manage the switching between two modes is also proposed. Based on the rule, the system can be prevented from running out of energy. Therefore, unlike the traditional active and semi-active suspension systems, the control of the hybrid suspension system is independent of external energy. The numerical simulation is conducted, and the results reveal that the system performs not only as well as the active suspension system but saves energy at the same time.

6.1. Control Methods for Vehicle Suspension Systems

In this section, passive damping control and several active/semi-active control methods are examined (Shen, Golnaraghi, & Heppler, 2006). The control performances of different methods are compared through the numerical simulation. To fully understand the effects of the examined control strategies, the transient response and steady-state response are evaluated based on bump excitation and harmonic excitation, respectively.

6.1.1. *Active Skyhook Control*

Because one of the major performance metrics of a vehicle suspension system is the minimization of acceleration of the sprung mass, (Karnopp, Crosby, & Harwood, 1974) proposed the Skyhook method, which attempts to limit the movement of the sprung mass through the introduction of a fictitious damper between the mass and a fixed inertial reference. The schematic structure of a typical Skyhook control system model is shown in Figure 6.1.

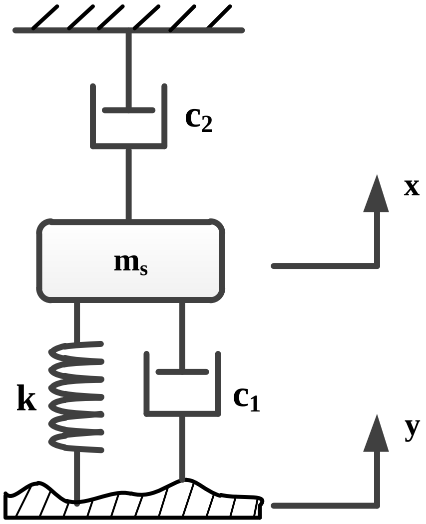

Figure 6.1 Schematic structure of a typical Skyhook control system model

This control method is achieved in practice through use of an actuator in a fully-active system. Considering a 1-DOF suspension system equipped with a Skyhook damper, the damping force can be found as follows:

$$F_d = c_{sky}\dot{x} \tag{174}$$

where c_{sky} is the damping coefficient of the Skyhook damper and $\dot{x}$ is the velocity of the sprung mass. However, conventional dampers and the electrical damper proposed in this thesis can only generate the damping force proportional to the relative velocity, $\dot{x} - \dot{y}$. When $\dot{x}$ and $\dot{x} - \dot{y}$ move in opposite directions, active Skyhook control is not usable, as it may result in worse responses.

6.1.2. Semi-Active Skyhook Control

In absence of an active actuator, the suspension system uses a semi-active damper mounted conventionally between the base and the sprung mass to replicate a Skyhook damping force. In this case, the control law for a 1-DOF system is designed as follows:

$$F_d = \begin{cases} c_{sa}(\dot{x} - \dot{y}) & \dot{x}(\dot{x} - \dot{y}) \geq 0 \\ 0 & \dot{x}(\dot{x} - \dot{y}) < 0 \end{cases} \tag{175}$$

where c_{sa} is the semi-active damping coefficient. Since the semi-active damper can only provide a force in the direction of relative velocity, $\dot{x} - \dot{y}$, when $\dot{x}$ and $\dot{x} - \dot{y}$ are of opposite signs, the force required for the Skyhook damper is opposite to the damping force provided by the semi-active damper. Therefore, the best that can be done is to minimize the damping force, which ideally means supply no force at all. The switching of the damper's status is controlled by the condition $\dot{x}(\dot{x} - \dot{y})$. Comparing Eq. (174) and (175), when the damper is on, it should be able to supply the damping force as needed by the Skyhook control law, which means

$$F_d = c_{sky}\dot{x} = c_{sa}(\dot{x} - \dot{y}) \tag{176}$$

Therefore, the value of c_{sa} should be given as

$$c_{sa} = \frac{c_{sky}\dot{x}}{(\dot{x} - \dot{y})} \tag{177}$$

It can be seen from Eq. (177) that when the relative velocity is very small, the required damping coefficient can be extremely large. However, in reality, the damping coefficient is limited by the physical constraints of the semi-active damper, which are upper and lower bounds, c_{max} and c_{min}. Thus, according to (Liu, Waters, & Brennan, 2005), the feasible damping coefficient can be rewritten as

$$c_{sa} = \begin{cases} max\left(c_{min}, min\left(\frac{c_{sky}\dot{x}}{(\dot{x}-\dot{y})}, c_{max}\right)\right) & \dot{x}(\dot{x}-\dot{y}) \geq 0 \\ c_{min} & \dot{x}(\dot{x}-\dot{y}) < 0 \end{cases} \tag{178}$$

The control law described in Eq. (178) is continuously variable. To simplify the operation, an on-off control scheme has been proposed which acts as a conventional passive damper, and the damping coefficient is switched between the maximum and minimum values of the damper (Karnopp, Crosby, & Harwood, 1974). The control law can be written as

$$c_{sa} = \begin{cases} c_{max} & \dot{x}(\dot{x}-\dot{y}) \geq 0 \\ c_{min} & \dot{x}(\dot{x}-\dot{y}) < 0 \end{cases} \tag{179}$$

The difference between continuous Skyhook control and on-off Skyhook control is that the former method attempts to provide the same amplitude and phase as those of the active Skyhook control when the damper is enabled. However, its performance is constrained by the limitations of the physical device. The latter method can only guarantee that the damping force remains the same sign as the active Skyhook damper. Experiments show that both semi-active Skyhook control methods provide comparable performance and gain big improvements over the passive suspension system (Ivers & Miller, 1989).

6.1.3. Semi-Active Rakheja-Sankar Control

Research by (Rakheja & Sankar, 1985) found that the damping force provided by a passive damper tends to increase the acceleration of the suspended mass when it is in the same direction as the spring force. Ideally, a semi-active damper should provide no damping force or minimized damping in this situation. To overcome this effect, (Alanoly & Sankar, 1987) suggested that the damping force should be set off when in the same direction as the spring force, and should cancel out the spring force when in the opposite direction. An on-off control strategy was designed accordingly and mathematically expressed as follows:

$$F_d = \begin{cases} -k(x-y) & (x-y)(\dot{x}-\dot{y}) \leq 0 \\ 0 & (x-y)(\dot{x}-\dot{y}) > 0 \end{cases} \tag{180}$$

Much as the Skyhook method was simplified to provide an on-off control since it is difficult to make the damping force fully follow the spring force due to the limitation of the physical damper in practice, a new form of the Rakheja-Sankar control strategy that does not require following the spring force was created as

$$c_{sa} = \begin{cases} c_{max} & (x-y)(\dot{x}-\dot{y}) \leq 0 \\ c_{min} & (x-y)(\dot{x}-\dot{y}) > 0 \end{cases} \tag{181}$$

6.1.4. Modified Skyhook Control

By utilizing a control method called double-band hysteresis current control (DB-HCC), a SMR power electronic circuit was developed that is capable of providing either positive or negative damping by controlling the electric current to alternate between regenerative and motoring modes (Hsieh, Huang, Golnaraghi, & Moallem, 2016). Therefore, the damper can supply a negative force from a negative damping coefficient, $-c_{sky}$. In this case, a modified Skyhook control algorithm was proposed and can be written as

$$F_d = \begin{cases} c_{sky}(\dot{x}-\dot{y}) & \dot{x}(\dot{x}-\dot{y}) \geq 0 \\ -c_{sky}(\dot{x}-\dot{y}) \quad or \quad 0 & \dot{x}(\dot{x}-\dot{y}) < 0 \end{cases} \tag{182}$$

when $\dot{x}(\dot{x}-\dot{y}) < 0$, F_d is determined for either better vehicle control (i.e., negative force) or energy harvesting (i.e., zero force), respectively. This is due to the negative direction of current results in power consumption of the electrical load. The Skyhook damping coefficient c_{sky} can be realized by synthesizing a tunable load resistance, R_{load} , by the proposed SMR power electronics. Specifically, it can be calculated referring to Eq. (29)

$$R_{load} = \frac{k_e k_t {k_g}^2 \eta_g^2}{c_{sky} d^2 \eta_b^2} - R_{int} \tag{183}$$

The desired positive or negative damping force can be provided by tuning the circuit current I, in terms of the reference current I_{ref}. By recalling Eq. (27), in order to implement the control algorithm in the electrical domain by the SMR, the current should be controlled to the following reference current:

$$I_{ref} = \begin{cases} \dfrac{k_e k_g \eta_g}{(R_{int} + R_{load}) d \eta_b} \dot{z} & \dot{x}(\dot{x}-\dot{y}) \geq 0 \\ -\dfrac{k_e k_g \eta_g}{(R_{int} + R_{load}) d \eta_b} \dot{z} \quad or \quad 0 & \dot{x}(\dot{x}-\dot{y}) < 0 \end{cases} \tag{184}$$

When the stored energy is enough to supply a negative current, the damper provides active Skyhook control to maintain the best dynamic control. Otherwise, it acts as a semi-active Skyhook damper.

6.1.5. *Comparison of Different Control Methods*

Numerical simulations are conducted in this section to compare the control performance of different control methods, including passive control, semi-active Skyhook control, semi-active Rakheja-Sankar control, and modified Skyhook control. The evaluated system is the proposed 1-DOF regenerative suspension system whose dynamic equation follows Eq. (42) and (43).

During the simulation spring constant k does not vary, while the damping coefficient c is adjusted by the control strategy and can have a value of either $c_{max}(= c_{sky})$ or $c_{min}(= 0)$. In the following simulation, the value of the load resistance is selected as $40\,\Omega$ to achieve the optimal damping for energy harvesting, as introduced in Chapter 3. The testing is conducted under the following assumptions:

- The damper is capable of a c_{min} value of zero and is able to instantly change values;
- The spring and damper are operating linearly;
- The modified Skyhook control is able to provide negative damping force as needed;
- The relative displacement sensor and the absolute acceleration sensor are operating with perfect accuracy, linearly and instantaneously;
- Ride comfort is used as the criterion of control performance so the absolute acceleration of the sprung mass is compared based on different control methods.

(1) Transient Response

The test of the system's transient response utilizing different control methods is based on bump excitation. Assuming a vehicle is running through a speed hump that is 350 mm wide and 50 mm high and the vehicle speed is kept at 12.6 km/h, the situation is indicated in Figure 6.2.

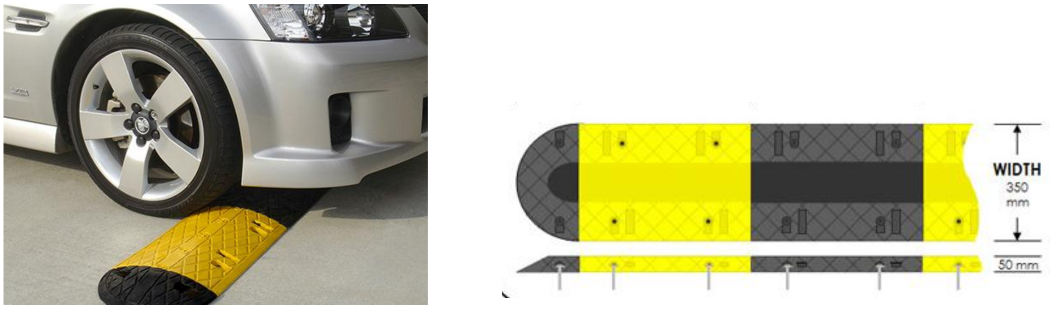

Figure 6.2 Situation of a vehicle running through a speed hump[2]

The bump excitation can be expressed mathematically as

$$y = 0.05[\sin(10\pi t)]^2 \tag{185}$$

and the profile of the excitation is shown in Figure 6.3.

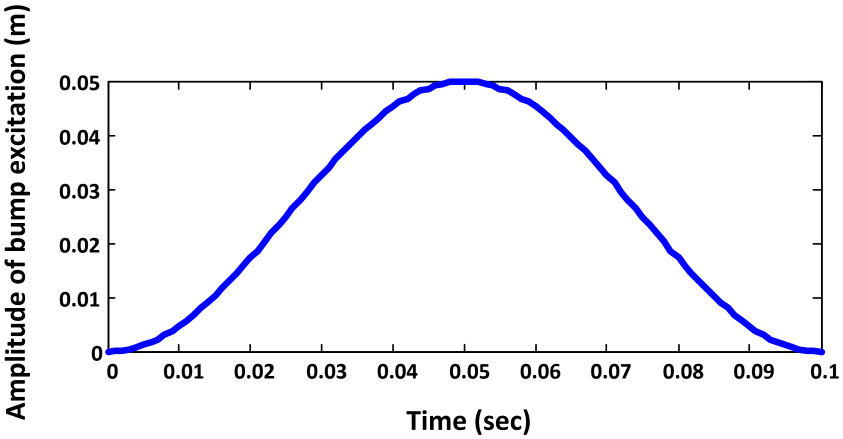

Figure 6.3 Profile of the bump excitation

The simulation results are shown in Figure 6.4. All the semi-active and active control methods can provide better control of the bump excitation. Specifically, both semi-active control methods made 10.3% and 11.2% decreases in the first and second peak acceleration (Point 1 and Point 2) compared with the passive system. Furthermore, Skyhook control decreased

---

[2] According to product specifications from JMP Holdings Pty Ltd.

28.4%, and Rakheja-Sankar control decreased 16.2% in the third peak acceleration (Point 3). The modified Skyhook control method contributed to 11.3%, 56.8%, and 43% decreases, respectively. Due to the discontinuity of the excitation acceleration at Point 3, a sudden drop happened from Point 3 to Point 4, where all the control methods performed worse than the passive system. Overall, the modified Skyhook strategy offers the best control performance in dealing with the bump excitation.

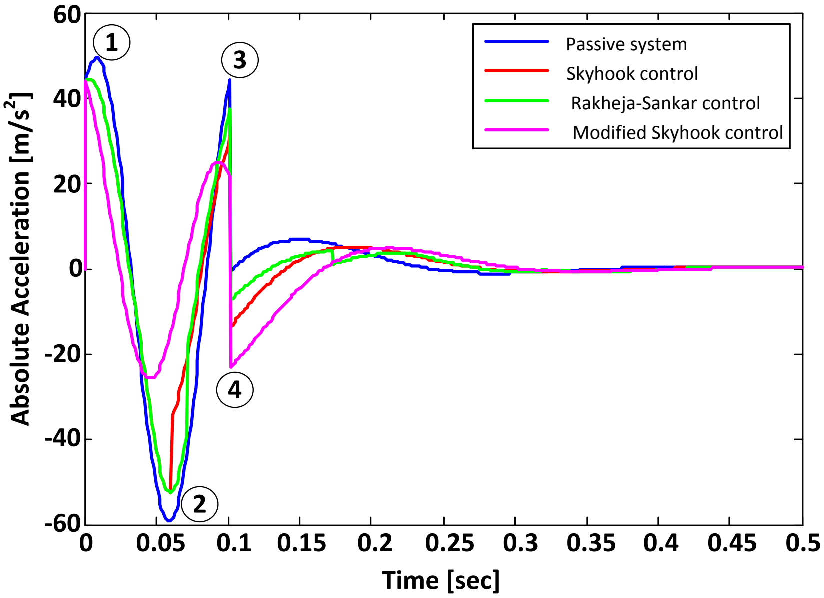

Figure 6.4 Absolute acceleration responses of the system with different control methods based on bump excitation

(2) Steady-State Response (Frequency Response)

The test of the system’s steady-state response based on different control methods is examined in terms of the system’s frequency response over 2 Hz to 9 Hz with base excitation amplitude of 20mm. The curves of the system’s absolute acceleration transmissibility are plotted in Figure 6.5. Results show that both semi-active control methods did not improve performance in the low frequency region (i.e., excitation frequency lower than natural frequency) and the Rakheja-Sankar method even performed worse than the passive system. However, in the high-frequency region where excitation frequency is higher than natural frequency, both semi-active controls obtained lower absolute acceleration than the passive system. Apparently, the modified Skyhook control strategy contributed to a significant reduction of absolute acceleration over the whole frequency range, thus achieving the best control performance. The RMS values of the absolute acceleration transmissibility are calculated and plotted in Figure 6.6, which quantifies the control performance by using different control methods (lower is better).

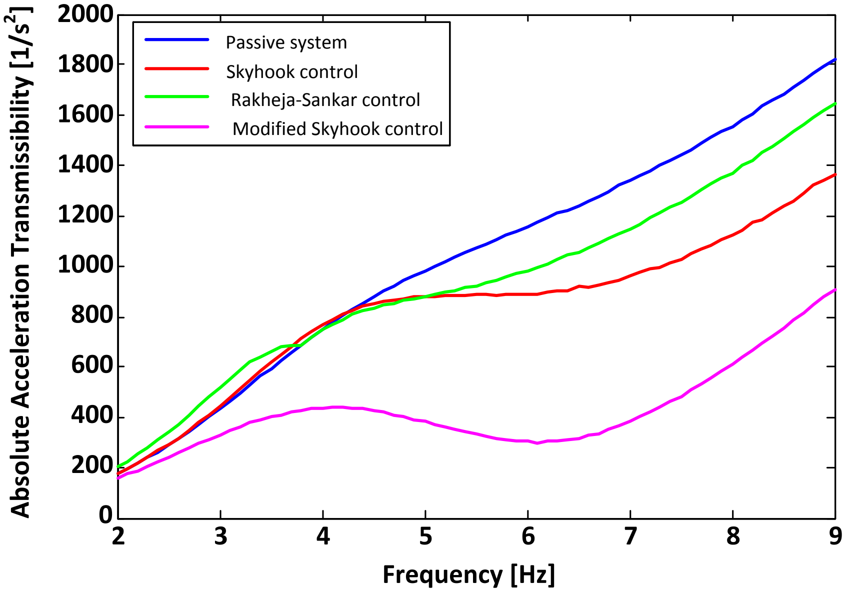

Figure 6.5 Absolute acceleration responses of the system with different control methods based on harmonic excitation

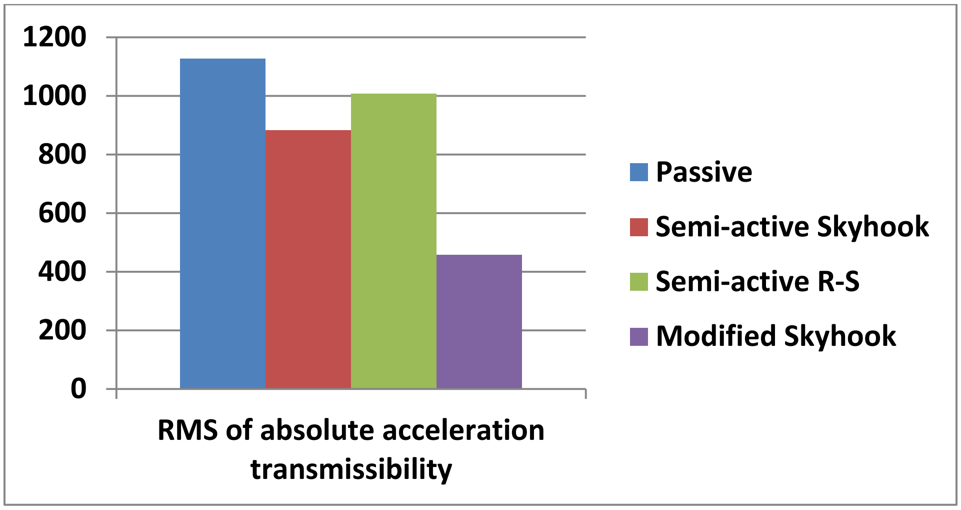

Figure 6.6 RMS of absolute acceleration transmissibility for different control methods

6.2. Operation Modes for the Hybrid Suspension System

In this section, a decision strategy for mode switch between energy harvesting and dynamic control is proposed. The amount of the energy required for the active control is calculated, and the conditions under which the self-powered system would be feasible are studied.

6.2.1. Schematic of the Hybrid Suspension System

The schematic of the proposed hybrid suspension system is shown in Figure 6.7. The system consists of two operating modes: regeneration mode and control mode.

In regeneration mode ($\dot{x}(\dot{x}-\dot{y}) \geq 0$), the system supplies the positive damping force while harvesting real power from the regenerative vehicle suspension. In control mode ($\dot{x}(\dot{x}-\dot{y}) < 0$), the system provides either negative (i.e. consuming energy) or zero (i.e. no energy flow) damping force that depends on the relationship between desired energy and stored energy, and the damper alternates between active and semi-active while the suspension is under control.

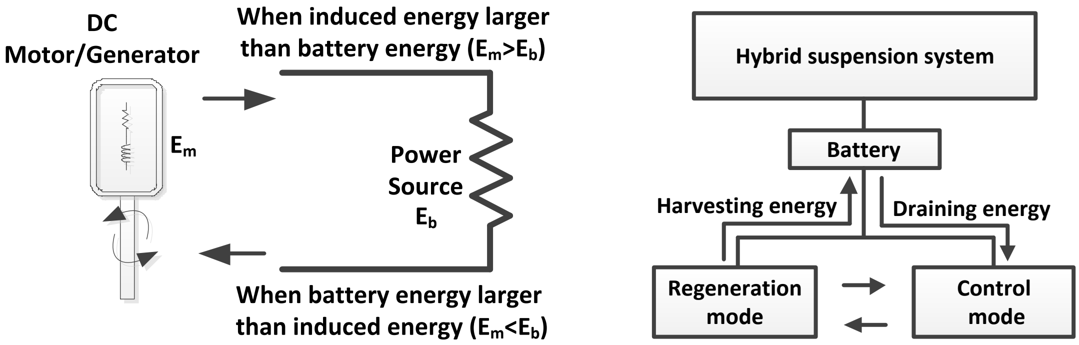

Figure 6.7 Schematic of the hybrid suspension system

6.2.2. Conditions of Self-Powered Control

Assuming the induced back-EMF voltage by the electrical motor/generator is E_m, the instantaneous electrical power generated by the damper is

$$P_{gen} = \left(\frac{E_m}{R_{int} + R_{load}}\right)^2 \cdot R_{load} \tag{186}$$

Thus, the cumulative generated energy is calculated as

$$E_{gen} = \int_0^t P_{gen} dt \tag{187}$$

When the active Skyhook control is set on, the desired negative damping force is given by

$$F_d^- = -c_{sky}(\dot{x} - \dot{y}) \tag{188}$$

Since F_d^- is to be provided by the DC motor, the desired power to supply the damping force can be calculated by

$$P_d = F_d^-(\dot{x} - \dot{y}) = -c_{sky}(\dot{x} - \dot{y})^2 \tag{189}$$

Eq. (189) shows that the power is always negative to provide a negative damping force, which means the damper is draining power in this case. Therefore, the required energy during the time Δt will be

$$E_d = P_d \cdot \Delta t \tag{190}$$

When the stored energy in the battery, E_{gen}, is higher than the desired energy for the active control, E_d, the system is able to provide enough power for the damping force without external energy.

The algorithm to determine the suspension system operating with the self-powered regenerative Skyhook control strategy is described in Figure 6.8.

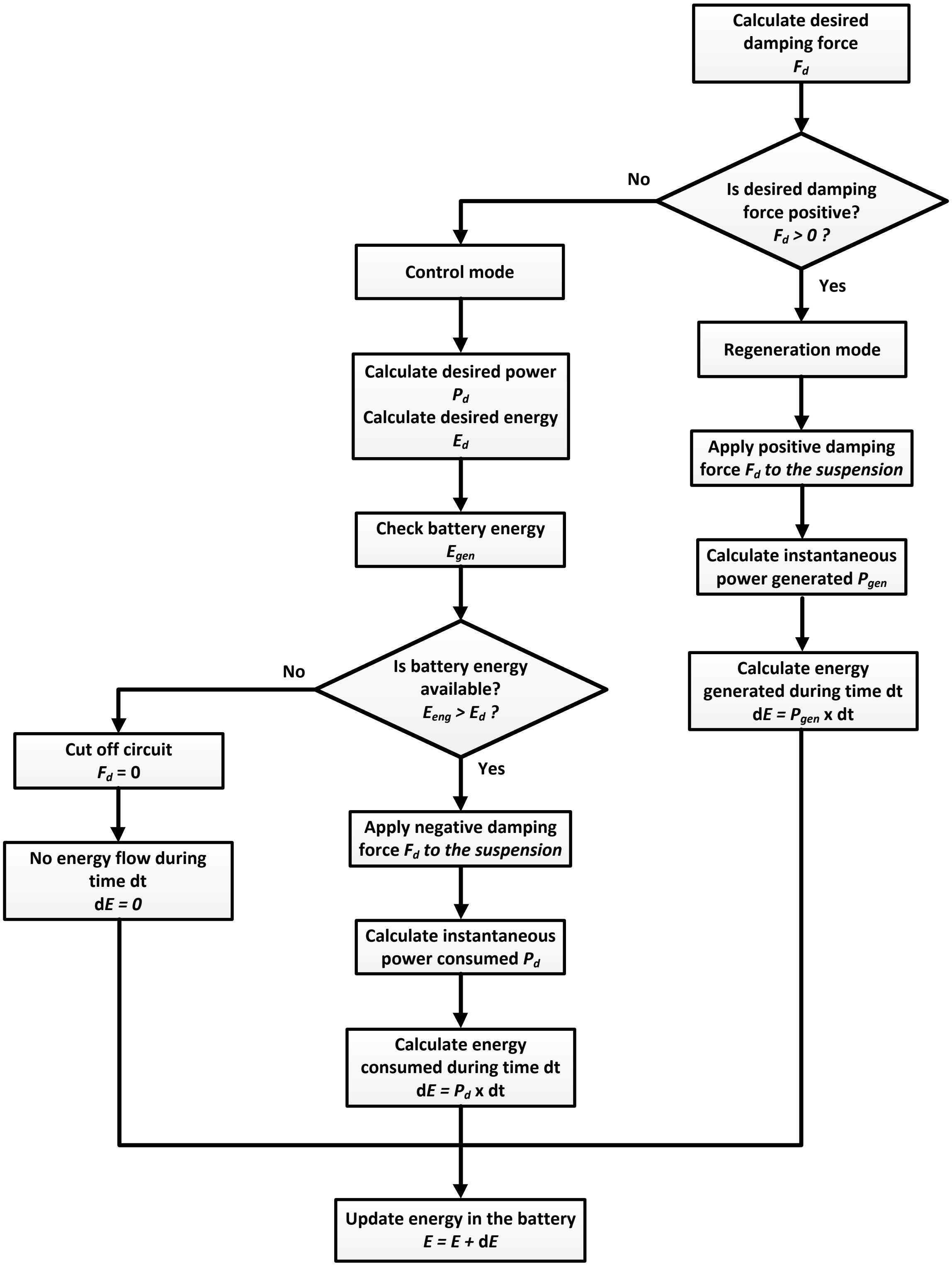

Figure 6.8 Algorithm for determining the suspension system operating with the self-powered regenerative Skyhook control strategy

6.3. Numerical Simulation Results

To verify the feasibility and effectiveness of the suspension system utilizing the proposed self-powered regenerative Skyhook control strategy, the numerical simulation was implemented in Matlab environment to evaluate the performance of the controlled system. The values of the main parameters for the quarter-car suspension system were selected as in Table 2.1. The capacity of the battery was 24 kWh, and initially it was assumed that the battery was fully discharged. The excitation profile is a harmonic waveform whose amplitude is 20 mm, and frequency is sweeping from 2 Hz to 9 Hz with increments at 0.1 Hz/s for 70 s. The profile of the excitation is shown in Figure 6.9.

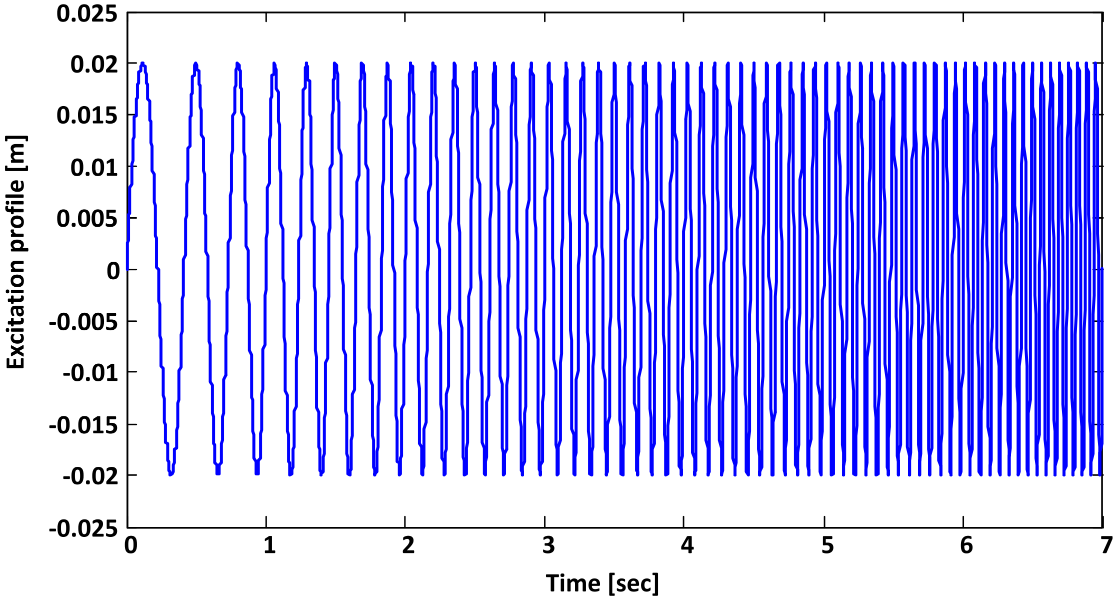

Figure 6.9 Excitation profile with frequency sweeping from 2 Hz to 9 Hz

Figure 6.10 (a) indicates the absolute acceleration of the sprung mass for passive control, semi-active Skyhook control, externally-powered modified Skyhook control, and self-powered modified Skyhook control. The zoomed-in waveform between 1 s to 3 s is shown in Figure 6.10 (b). The instantaneous power of the battery and its cumulative energy the whole time are depicted in Figure 6.11.

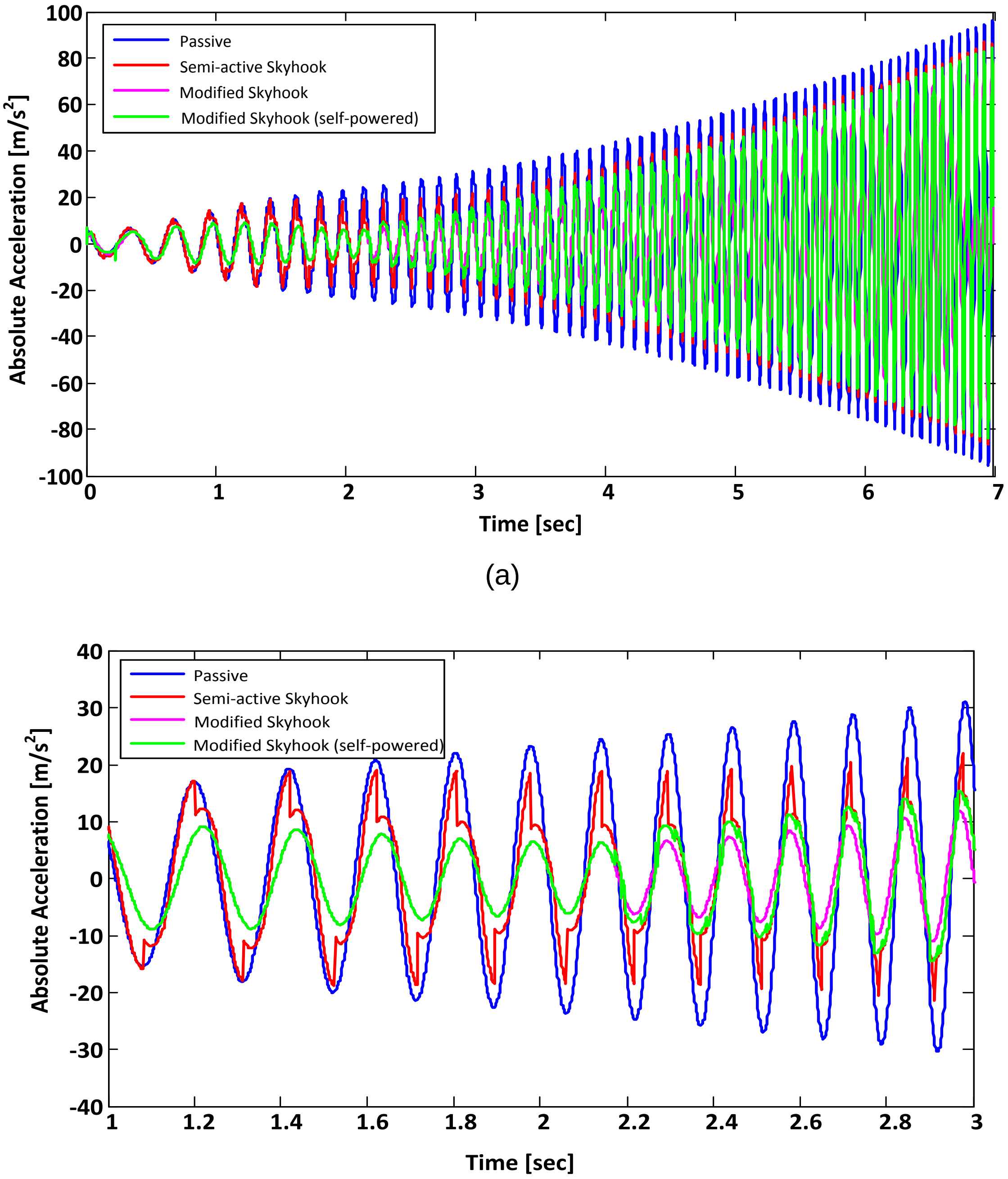

(a)

(b)

Figure 6.10 Absolute acceleration of the sprung mass for passive and controlled systems: (a) 0 - 7 s and (b) zoomed-in at 1 s - 3 s

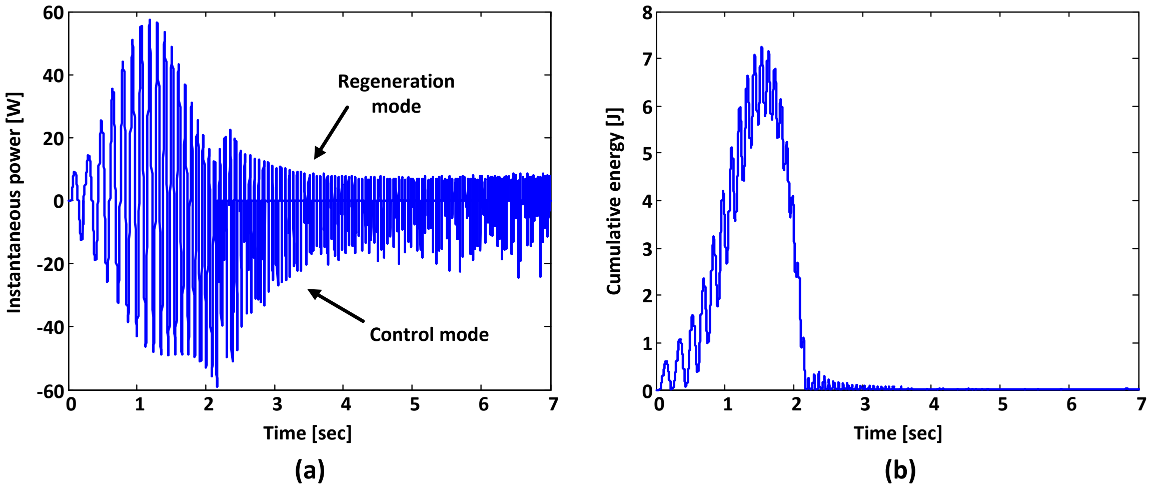

Figure 6.11 Instantaneous power and cumulative energy of the battery

Referring to Figure 6.10, the self-powered modified Skyhook control method performed as well as the externally-powered modified Skyhook control method before 2 Hz. After 2 Hz, the performance of the self-powered modified Skyhook control appears moderate, between the externally-powered modified Skyhook control and semi-active Skyhook control. Figure 6.11 (a) shows how the controller switched between regeneration mode and control mode. Figure 6.11 (b) indicates that the energy reached maximum before 2 Hz and reduced gradually afterwards, which explains why the control performance declined after 2 Hz. Apparently, the self-powered modified Skyhook control strategy proposed in this work outperformed semi-active control methods, and its property of external power independence is a big advantage over active control methods.

6.4. Conclusion

In this chapter, a regenerative Skyhook control strategy was demonstrated and compared with other damping control methods based on bump and harmonic excitations. The strategy was able to provide energy harvesting and dynamic control simultaneously. An algorithm was described in determining two operating modes for the suspension system. It was demonstrated, through the numerical simulation, that the proposed control strategy was able to operate using self-generated power and outperformed the conventional semi-active control methods. The next chapter concludes the overall work proposed in this thesis, and outlines potential future works.

Chapter 7.

Conclusion and Future Work

7.1. Conclusion

At present, a series of energy and environmental issues caused by excessive vehicles have been a serious concern. Large amounts of energy are consumed, but only a small ratio of that is utilized to drive a car. One important reason is that much energy has been wasted by the shock absorber in the suspension system. The traditional suspension system contains a viscous shock absorber that dissipates road energy into waste heat. On the other hand, to maintain better ride comfort for passengers, conventional passive suspension is not suitable because it cannot accomplish variable control objectives. Various sophisticated suspension control strategies, including active and semi-active control methods, have been proposed to improve the control performance; however, they consume a certain level of electrical power.

The main objective of the research in this thesis is to regenerate the waste energy from the vehicle suspension and enable the dynamic control of the vehicle sprung mass simultaneously. Motivated by the demand of both energy saving and dynamic control, an energy-regenerative vehicle suspension system is developed to meet the purpose. The proposed system not only harvests vibrational energy induced by road irregularities, but also provides adjustable levels of damping in the electrical domain to achieve a suitable ride comfort. The contributions of this thesis are summarized as follows:

1. A 1-DOF energy-regenerative suspension system was designed, and its mathematical modeling was derived. A small-scale proof-of-concept prototype was manufactured, and a test-bed was established to verify its effectiveness. Experimental results were obtained and compared with numerical simulation results. The results showed that the proposed system is capable of providing appropriate damping control and regenerating energy from external excitation.

2. Two systematic optimization methodologies for parameters design of the suspension system were proposed, with respect to harmonic excitation and ISO standard road profile. Both methods presented graphical optimization rules in terms of RMS of the absolute acceleration transmissibility and average of the power generation transmissibility. The experimental results demonstrated that the optimization strategies well predicted the system performance under different conditions and were effective when used as the guideline for optimal design of the regenerative suspension system.

3. A nonlinear strategy for the purpose of extending the suspension system's operational frequency region was implemented. The technique utilized cubic nonlinearity to introduce a Duffing equation to the system's dynamic modeling. Thus, it overcomes the limited bandwidth of the linear resonant generator. A piecewise linear spring system was used to physically realize nonlinear phenomena, and it significantly improved the energy harvesting capability of the suspension system according to the experiment results.

4. A regenerative Skyhook control strategy was proposed for the combination of power regeneration and active Skyhook control. The possibility of the strategy's external power independence was examined, and a mode switch algorithm was designed to guarantee

that the Skyhook control operates using the self-generated energy. Numerical simulations were conducted to verify the effectiveness of the proposed strategy, which therefore mitigates the contradiction between control deficiency of passive suspension control and power consumption of active suspension control.

7.2. Future Work

Based on the completed work and results obtained from this research, additional works are taken into consideration and expected to be accomplished in the future, as follows:

1. This work has shown a strong relationship between RMS analysis and stochastic-based analysis. The expectation of the stochastic response has been derived from the RMS information. In future work, the explicit relationship between RMS results for the harmonic excitation and results for the stochastic excitation should be investigated. Similar method can be utilized to analyze the system response based on bump excitation, by transforming the response in time-domain to the sequence in frequency-domain.
2. The cubic nonlinearity introduced in this thesis is able to extend the system’s bandwidth; however, it also sacrifices the control performance, especially at high frequency. To maintain ride comfort and road handling at an acceptable level, some advanced optimization strategies should be investigated to deal with the trade-off between power regeneration and ride comfort/road handling of the nonlinear suspension system using perturbation methods.
3. Currently the nonlinearities are added physically to the system by using piecewise linear spring. However, considering the size and

weight would be increased due to additional components, future work should investigate on introducing nonlinearities electronically.

4. In this work, feasibility of the regenerative Skyhook control strategy using self-power is examined by numerical simulations but lacks experimental verification. The experimental test on the regenerative Skyhook control strategy should be implemented for future work.

References

Adcock, I. (2012). *Michelin's innovative active wheel*. Retrieved from http://www.roadandtrack.com/car-shows/news/a21961/michelins-innovative-active-wheel-2012-goodwood-festival-of-speed-36312/.

Adhikari, S., Friswell, M. I., & Inman, D. J. (2009). Piezoelectric energy harvesting from broadband random vibrations. *Smart Materials and Structures, 18*(11), 115005.

Alanoly, J., & Sankar, S. (1987). A new concept in semi-active vibration isolation. *Journal of Mechanical Design, 109*(2), 242-247.

Anderson, T. J., Nayfeh, A. H., & Balachandran, B. (1996). Coupling between high-frequency modes and a low-frequency mode: Theory and experiment. *Nonlinear Dynamics, 11*(1), 17-36.

Appleyard, M., & Wellstead, P. E. (1995). Active suspensions: Some background. *In Control Theory and Applications, IEE Proceedings, IET, 142*(2), 123-128.

Arzanpour, S., Eslaminasab, N., Shubert, B., Narimani, A., & Golnaraghi, M. F. (2006). A novel technique for frequency and time optimization of automotive engine mount parameters. *ASME International Mechanical Engineering Congress and Exposition*, (pp. 1613-1620).

Ashmore, S. C., & Hodges, H. C. (1992). Dynamic force measurement vehicle (DFMV) and its application to measuring and monitoring road roughness. In J. J. Henry, & J. C. Wambold, *Vehicle, Tire, Pavement Interface* (pp. 69-69). ASTM Special Technical Publication 1164.

Barton, D. A., Burrow, S. G., & Clare, L. R. (2010). Energy harvesting from vibrations with a nonlinear oscillator. *Journal of Vibration and Acoustics, 132*(2), 021009.

Bastow, D., Howard, G., & Whitehead, J. P. (2004). *Car suspension and handling* (4th ed.). Warrendale, PA: SAE international.

Beeby, S. P., Torah, R. N., Tudor, M. J., Glynne-Jones, P., O'Donnell, T., Saha, C. R., et al. (2007). A micro electromagnetic generator for vibration energy harvesting. *Journal of Micromechanics and Microengineering, 17*(7), 1257.

Biglarbegian, M. M., & Golnaraghi, F. (2006). Intelligent control of vehicle semi-active suspension systems for improved ride comfort and road handling. *In Fuzzy Information Processing Society. NAFIPS 2006. Annual meeting of the North American* (pp. 19-24). IEEE.

Biglarbegian, M. M., & Golnaraghi, F. (2008). A novel neuro-fuzzy controller to enhance the performance of vehicle semi-active suspension systems. *Vehicle System Dynamics, 46*(8), 691-711.

Bogsjö, K., Podgórski, K., & Rychlik, I. (2012). Models for road surface roughness. *Vehicle System Dynamics, 50*(5), 725-747.

Bolandhemmat, H. C., & Golnaraghi, F. (2010). Development of a systematic and practical methodology for the design of vehicles semi-active suspension control system. *Vehicle System Dynamics, 48*(5), 567-585.

Bose Suspension System. (n.d.). Retrieved from https://www.bose.co.uk/GB/en/automotive/innovations/suspension-system/.

Bourmistrova, A., Storey, I., & Subic, A. (2005). Multiobjective optimisation of active and semi-active suspension systems with application of evolutionary algorithm. *In Proceedings of the 2005 International Conference on Modelling and Simulation*, (pp. 12-15). Melbourne, Australia.

Burrow, S. G., & Clare, L. R. (2007). A resonant generator with non-linear compliance for energy harvesting in high vibrational environments. *In Electric Machines & Drives Conference. IEMDC'07. IEEE International* (pp. 715-720). IEEE.

Burrow, S. G., Clare, L. R., Carrella, A., & Barton, D. (2008). Vibration energy harvesters with non-linear compliance. *The 15th International Symposium on: Smart Structures and Materials & Nondestructive Evaluation and Health Monitoring* (pp. 692807-692807). International Society for Optics and Photonics.

Cammarano, A., Burrow, S. G., Barton, D. A., Carrella, A., & Clare, L. R. (2010). Tuning a resonant energy harvester using a generalized electrical load. *Smart Materials and Structures, 19*(5), 055003.

Challa, V. R., Prasad, M. G., Shi, Y., & Fisher, F. T. (2008). A vibration energy harvesting device with bidirectional resonance frequency tunability. *Smart Materials and Structures, 17*(1), 015035.

Chen, C., & Liao, W. H. (2012). A self-sensing magnetorheological damper with power generation. *Smart Materials and Structures, 21*(2), 025014.

Choi, Y. T., & Wereley, N. M. (2009). Self-powered magnetorheological dampers. *Journal of Vibration and Acoustics, 131*(4), 044501.

Crews, J. H., Mattson, M. G., & Buckner, G. D. (2011). Multi-objective control optimization for semi-active vehicle suspensions. *Journal of Sound and Vibration, 330*(23), 5502-5516.

David, S., & Bobrovsky, B. (2011). Actively controlled vehicle suspension with energy regeneration capabilities. *Vehicle System Dynamics, 49*(6), 833-854.

Davis, B. R., & Thompson, A. G. (2001). Power spectral density of road profiles. *Vehicle System Dynamics, 35*(6), 409-415.

Di Monaco, F., Tehrani, M. G., Elliott, S. J., Bonisoli, E., & Tornincasa, S. (2013). Energy harvesting using semi-active control. *Journal of Sound and Vibration, 332*(23), 6033-6043.

Duquette, A. P., Tuer, K. L., & Golnaraghi, M. F. (1993). Vibration control of a flexible beam using a rotational internal resonance controller, part II: Experiment. *Journal of Sound and Vibration, 167*(1), 63-75.

Dyer, E. (2015). *3 technologies that are making car suspensions smarter than ever*. Retrieved from http://www.popularmechanics.com/cars/a14665/why-car-suspensions-are-better-than-ever/.

Ebrahimi, B. (2009). *Development of hybrid electromagnetic dampers for vehicle suspension systems.* Doctoral dissertation, University of Waterloo, Ontario, Canada.

Ebrahimi, B., Bolandhemmat, H., Khamesee, M., & Golnaraghi, M. F. (2011). A hybrid electromagnetic shock absorber for active vehicle suspension. *Vehicle System Dynamics, 49*(1), 311-332.

Ebrahimi, B., Khamesee, M. B., & Golnaraghi, F. (2008). Eddy current damper feasibility in automobile suspension: modeling, simulation and testing. *Smart Materials and Structures, 18*(1), 015017.

Ebrahimi, B., Khamesee, M. B., & Golnaraghi, F. (2009). A novel eddy current damper: theory and experiment. *Journal of Physics D: Applied Physics, 42*(7), 075001.

Ebrahimi, B., Khamesee, M. B., & Golnaraghi, F. (2010). Permanent magnet configuration in design of an eddy current damper. *Microsystem Technologies, 16*(1-2), 19-24.

Ebrahimi, B., Khamesee, M. B., & Golnaraghi, M. F. (2008). Design and modeling of a magnetic shock absorber based on eddy current damping effect. *Journal of Sound and Vibration, 315*(4), 875-889.

Ebrahimi, B., Khamesee, M. B., & Golnaraghi, M. F. (2008). Feasibility study of an electromagnetic shock absorber with position sensing capability. *In Industrial Electronics. IECON 2008. 34th Annual Conference of IEEE* (pp. 2988-2991). IEEE.

El-Hami, M., Glynne-Jones, P., White, N., Hill, M., Beeby, S., James, E., et al. (2001). Design and fabrication of a new vibration-based electromechanical power generator. *Sensors and Actuators A: Physical, 92*(1), 335-342.

Eslaminasab, N. (2008). *Development of a semi-active intelligent suspension system for heavy vehicles.* Doctoral dissertation, University of Waterloo, Ontario, Canada.

Eslaminasab, N., Arzanpour, S., & Golnaraghi, M. F. (2007). Optimal design of asymmetric passive and semi-active dampers. *ASME International Mechanical Engineering Congress and Exposition*, (pp. 1841-1847).

Gao, W., Zhang, N., & Dai, J. (2008). A stochastic quarter-car model for dynamic analysis of vehicles with uncertain parameters. *Vehicle System Dynamics, 46*(12), 1159-1169.

Georgiou, G., Verros, G., & Natsiavas, S. (2007). Multi-objective optimization of quarter-car models with a passive or semi-active suspension system. *Vehicle System Dynamics, 45*(1), 77-92.

Gillespie, T. D. (1992). *Fundamentals of vehicle dynamics.* Warren, PA: Society of Automotive Engineers.

Gobbi, M., & Mastinu, G. (2001). Analytical description and optimization of the dynamic behaviour of passively suspended road vehicles. *Journal of Sound and Vibration, 245*(3), 457-481.

Gobbi, M., Haque, I., Papalambros, P. P., & Mastinu, G. (2006). A critical review of optimization methods for road vehicles design. *In 11th AIAA/ISSMO Multidisciplinary Analysis and Optimization Conference*, (pp. 6-8).

Gobbi, M., Haque, I., Papalambros, P. Y., & Mastinu, G. (2005). Optimization and integration of ground vehicle systems. *Vehicle System Dynamics, 43*(6-7), 437-453.

Gobbi, M., Levi, F., & Mastinu, G. (2006). Multi-objective stochastic optimisation of the suspension system of road vehicles. *Journal of Sound and Vibration, 298*(4), 1055-1072.

Golnaraghi, M. F. (1991). Regulation of flexible structures via nonlinear coupling. *Dynamics and Control, 1*(4), 405-428.

Halvorsen, E. (2008). Energy harvesters driven by broadband random vibrations. *Journal of Microelectromechanical Systems, 17*(5), 1061-1071.

Hong, K. S., & Hedrick, J. K. (2002). Modified skyhook control of semi-active suspensions: A new model, gain scheduling, and hardware-in-the-loop tuning. *Journal of Dynamic Systems, Measurement, and Control, 124*(1), 158-167.

Hsieh, C. Y. (2014). *Energy harvesting and control of a regenerative suspension system using switched mode converters.* Doctoral dissertation, Simon Fraser University, BC, Canada.

Hsieh, C. Y., Huang, B., Golnaraghi, F., & Moallem, M. (2014). Sky-hook control for a regenerative suspension system. *IEEE 80th Vehicular Technology Conference*, (pp. 1-6). Vancouver.

Hsieh, C. Y., Huang, B., Golnaraghi, F., & Moallem, M. (2016). Regenerative skyhook control for an electromechanical suspension system using a switch mode rectifier. *IEEE Transactions on Vehicular Technology*, accepted.

Hsieh, C. Y., Huang, B., Golnaraghi, M. F., & Moallem, M. (2013). A bandwidth enhanced regenerative suspension system for electric vehicles. *Advanced Microsystems for Automotive Applications 2013*, (pp. 257-267).

Hsu, P. (1996). Power recovery property of electrical active suspension systems. *In Energy Conversion Engineering Conference, 1996. IECEC 96., Proceedings of the 31st Intersociety. IEEE.*

Huang, B., Hsieh, C. Y., Golnaraghi, F., & Moallem, M. (2015). A methodology for optimal design of a vehicle suspension system with energy regeneration capability. *Journal of Vibration and Acoustics, 137*(5), 051014.

Huang, B., Hsieh, C. Y., Golnaraghi, F., & Moallem, M. (2015). Development and optimization of an energy-regenerative suspension system under stochastic road excitation. *Journal of Sound and Vibration, 357*, 16-34.

Inamdar, K. V. (2011). *Vehicle suspension optimization for stochastic inputs.* Master's thesis, University of Texas at Arlington.

International Organization for Standardization. (1995). *ISO 8608: Mechanical vibration - Road surface profiles - Reporting of measured data.*

International Organization for Standardization. (1997). *ISO 2631-1: Mechanical vibration and shock – Evaluation of human exposure to whole-body vibration – Part 1: General requirements.*

Ivers, D., & Miller, L. (1989). Experimental comparison of passive, semi-active on/off, and semi-active continuous suspensions. *SAE Technical Paper*, No. 892484.

Jayachandran, R., & Krishnapillai, S. (2013). Modeling and optimization of passive and semi-active suspension systems for passenger cars to improve ride comfort and isolate engine vibration. *Journal of Vibration and Control, 19*(10), 1471-1479.

Jazar, G. N., Alkhatib, R., & Golnaraghi, M. F. (2006). Root mean square optimization criterion for vibration behaviour of linear quarter car using analytical methods. *Vehicle System Dynamics, 44*(6), 477-512.

Jazar, G. N., Narimani, A., Golnaraghi, M. F., & Swanson, D. A. (2003). Practical frequency and time optimal design of passive linear vibration. *Vehicle System Dynamics, 39*(6), 437-466.

Jin-qiu, Z., Zhi-zhao, P., Lei, Z., & Yu, Z. (2013). A review on energy-regenerative suspension systems for vehicles. *In Proceedings of the World Congress on Engineering*, *3*, pp. 3-5.

Karnopp, D. (1983). Active damping in road vehicle suspension systems. *Vehicle System Dynamics, 12*(6), 291-311.

Karnopp, D., Crosby, M. J., & Harwood, R. A. (1974). Vibration control using semi-active force generators. *Journal of Manufacturing Science and Engineering, 96*(2), 619-626.

Kawamoto, Y., Suda, Y., Inoue, H., & Kondo, T. (2007). Modeling of electromagnetic damper for automobile suspension. *Journal of System Design and Dynamics, 1*(3), 524-535.

Kawamoto, Y., Suda, Y., Inoue, H., & Kondo, T. (2008). Electro-mechanical suspension system considering energy consumption and vehicle manoeuvre. *Vehicle System Dynamics, 46*(S1), 1053-1063.

Kim, I. H., Jung, H. J., & Koo, J. H. (2010). Experimental evaluation of a self-powered smart damping system in reducing vibrations of a full-scale stay cable. *Smart Materials and Structures, 19*(11), 115027.

Kovacic, I., & Brennan, M. J. (2008). On the use of two classical series expansion methods to determine the vibration of harmonically excited pure cubic oscillators. *Physics Letters A, 372*(22), 4028-4032.

Kovacic, I., Brennan, M. J., & Lineton, B. (2008). On the resonance response of an asymmetric Duffing oscillator. *International Journal of Non-Linear Mechanics, 43*(9), 858-867.

Kowal, J., Pluta, J., Konieczny, J., & Kot, A. (2008). Energy recovering in active vibration isolation system—results of experimental research. *Journal of Vibration and Control, 14*(7), 1075-1088.

Li, Z., Zuo, L., Kuang, J., & Luhrs, G. (2012). Energy-harvesting shock absorber with a mechanical motion rectifier. *Smart Materials and Structures, 22*(2), 025008.

Li, Z., Zuo, L., Luhrs, G., Lin, L., & Qin, Y. (2013). Electromagnetic energy-harvesting shock absorbers: design, modeling, and road tests. *IEEE Transactions on Vehicular Technology, 62*(3), 1065 - 1074.

Liu, W. Q., Badel, A., Formosa, F., & Wu, Y. P. (2015). A new figure of merit for wideband vibration energy harvesters. *Smart Materials and Structures, 24*(12), 125012.

Liu, Y., Waters, T., & Brennan, M. (2005). A comparison of semi-active damping control strategies for vibration isolation of harmonic disturbances. *Journal of Sound and Vibration, 280*(1), 21-39.

Magneride™ Controlled Suspension System. (n.d.). Retrieved from http://www.bwigroup.com/en/pshow.php?pid=22.

Mann, B. P., & Sims, N. D. (2009). Energy harvesting from the nonlinear oscillations of magnetic levitation. *Journal of Sound and Vibration, 319*(1), 515-530.

Mercedes-Benz: Active Body Control ABC. (n.d.). Retrieved from http://techcenter.mercedes-benz.com/en_CA/abc/detail.html.

Mercedes-Benz: Magic Body Control. (n.d.). Retrieved from http://techcenter.mercedes-benz.com/en/magic_body_control/detail.html.

Montazeri-Gh, M., & Soleymani, M. (2010). Investigation of the energy regeneration of active suspension system in hybrid electric vehicles. *IEEE Transactions on Industrial Electronics, 57*(3), 918-925.

Montazeri-Gh, M., Soleymani, M., & Hashemi, S. (2013). Impact of traffic conditions on the active suspension energy regeneration in hybrid electric vehicles. *IEEE Transactions on Industrial Electronics, 60*(10), 4546-4553.

Nakano, K. (2004). Combined type self-powered active vibration control of truck cabins. *Vehicle System Dynamics, 41*(6), 449-473.

Nakano, K., Suda, Y., & Nakadai, S. (2003). Self-powered active vibration control using a single electric actuator. *Journal of Sound and Vibration, 260*(2), 213-235.

Narimani, A. (2004). *Development of linear and nonlinear isolation techniques for passive and semi-active applications.* Doctoral dissertation, University of Waterloo, Ontario, Canada.

Narimani, A., Golnaraghi, M. E., & Jazar, G. N. (2004). Frequency response of a piecewise linear vibration isolator. *Journal of Vibration and Control, 10*(12), 1775-1794.

Nayfeh, A. H. (2011). *Introduction to perturbation techniques.* Hoboken, NJ: John Wiley & Sons.

Nayfeh, A. H., & Mook, D. T. (2008). *Nonlinear oscillations.* Hoboken, NJ: John Wiley & Sons.

Nayfeh, A. H., Mook, D. T., & Marshall, L. R. (1973). Nonlinear coupling of pitch and roll modes in ship motions. *Journal of Hydronautics, 7*(4), 145-152.

Newland, D. E. (2012). *An introduction to random vibrations, spectral & wavelet analysis* (3rd ed.). Mineola, NY: Courier Dover Publications.

Oh, I. G., Nayfeh, A. H., & Mook, D. T. (2000). A theoretical and experimental investigation of indirectly excited roll motion in ships. *Philosophical Transactions of the Royal Society of London. Series A: Mathematical, Physical and Engineering Sciences, 358*(1771), 1853-1881.

Prabakar, R. S., Sujatha, C., & Narayanan, S. (2013). Response of a quarter car model with optimal magnetorheological damper parameters. *Journal of Sound and Vibration, 332*(9), 2191-2206.

Rakheja, S., & Sankar, S. (1985). Vibration and shock isolation performance of a semi-active “on-off” damper. *Journal of Vibration and Acoustics, 107*(4), 398-403.

Ramakrishnan, V., & Feeny, B. F. (2012). Resonances of a forced mathieu equation with reference to wind turbine blades. *Journal of Vibration and Acoustics, 134*(6), 064501.

Ramlan, R., Brennan, M. J., Mace, B. R., & Kovacic, I. (2010). Potential benefits of a non-linear stiffness in an energy harvesting device. *Nonlinear Dynamics, 59*(4), 545-558.

Renno, J. M., Daqaq, M. F., & Inman, D. J. (2009). On the optimal energy harvesting from a vibration source. *Journal of Sound and Vibration, 320*(1), 386-405.

Robson, J. D., & Dodds, C. J. (1976). Stochastic road inputs and vehicle response. *Vehicle System Dynamics, 5*(1-2), 1-13.

Rouillard, V., Bruscella, B., & Sek, M. (2000). Classification of road surface profiles. *Journal of Transportation Engineering, 126*(1), 41-45.

Roundy, S. (2005). On the effectiveness of vibration-based energy harvesting. *Journal of Intelligent Material Systems and Structures, 16*(10), 809-823.

Sabzehgar, R., Maravandi, A., & Moallem, M. (2014). Energy regenerative suspension using an algebraic screw linkage mechanism. *IEEE/ASME Transactions on Mechatronics*(99), 1-9.

Saha, C. R., O'Donnell, T., Loder, H., Beeby, S., & Tudor, J. (2006). Optimization of an electromagnetic energy harvesting device. *IEEE Transactions on Magnetics, 42*(10), 3509-3511.

Sapiński, B. (2010). Vibration power generator for a linear MR damper. *Smart Materials and Structures, 19*(10), 105012.

Sapiński, B. (2011). Experimental study of a self-powered and sensing MR-damper-based vibration control system. *Smart Materials and Structures, 20*(10), 105007.

Sharp, R. S., & Crolla, D. A. (1987). Road vehicle suspension system design- a review. *Vehicle System Dynamics, 16*(3), 167-192.

Shaw, S. W., & Holmes, P. J. (1983). A periodically forced piecewise linear oscillator. *Journal of Sound and Vibration, 90*(1), 129-155.

Shen, Y., Golnaraghi, M., & Heppler, G. (2006). Semi-active vibration control schemes for suspension systems using magnetorheological dampers. *Journal of Vibration and Control, 12*(1), 3-24.

Shirahatti, A., Prasad, P. S., Panzade, P., & Kulkarni, M. M. (2008). Optimal design of passenger car suspension for ride and road holding. *Journal of the Brazilian Society of Mechanical Sciences and Engineering, 30*(1), 66-76.

Singal, K., & Rajamani, R. (2013). Zero-energy active suspension system for automobiles with adaptive sky-hook damping. *Journal of Vibration and Acoustics, 135*(1), 011011.

Smith, M. C., & Swift, S. J. (2011). Power dissipation in automotive suspensions. *Vehicle System Dynamics, 49*(1-2), 59-74.

Song, X. (2009). Cost-effective skyhook control for semiactive vehicle suspension applications. *The Open Mechanical Engineering Journal, 3*(1), 17-25.

Stephen, N. G. (2006). On energy harvesting from ambient vibration. *Journal of Sound and Vibration, 293*(1-2), 409-425.

Stribrsky, A., Hyniova, K., Honcu, J., & Kruczek, A. (2007). Energy recuperation in automotive active suspension systems with linear electric motor. *Proceedings of the 15th Mediterranean Conference on Control & Automation. IEEE*, (pp. 1-5).

Suda, Y., Nakadai, S., & Nakano, K. (1998). Hybrid suspension system with skyhook control and energy regeneration (development of self-powered active suspension). *Vehicle System Dynamics, 29*(S1), 619-634.

Suda, Y., Shiiba, T., Hio, K., Kawamoto, Y., Kondo, T., & Yamagata, H. (2004). Study on electromagnetic damper for automobiles with nonlinear damping force characteristics: (road test and theoretical analysis). *Vehicle System Dynamics, 41*, 637-646.

Tamboli, J. A., & Joshi, S. G. (1999). Optimum design of a passive suspension system of a vehicle subjected to actual random road excitations. *Journal of Sound and Vibration, 219*(2), 193-205.

Tang, X., & Zuo, L. (2012). Simultaneous energy harvesting and vibration control of structures with tuned mass dampers. *Journal of Intelligent Material Systems and Structures, 23*(18), 2117-2127.

Tang, X., & Zuo, L. (2012). Vibration energy harvesting from random force and motion excitations. *Smart Materials and Structures, 21*(7), 075025.

Tehrani, M. G., & Elliott, S. J. (2014). Extending the dynamic range of an energy harvester using nonlinear damping. *Journal of Sound and Vibration, 333*(3), 623-629.

Thompson, A. G. (1976). An active suspension with optimal linear state feedback. *Vehicle System Dynamics, 5*(4), 187-203.

Tuer, K. L., Duquette, A. P., & Golnaraghi, M. F. (1993). Vibration control of a flexible beam using a rotational internal resonance controller, Part I: Theoretical development and analysis. *Journal of Sound and Vibration, 167*(1), 41-62.

U.S. Department of Energy. (n.d.). Retrieved from http://www.fueleconomy.gov/feg/evtech.shtml.

Valášek, M., Novak, M., Šika, Z., & Vaculin, O. (1997). Extended ground-hook-new concept of semi-active control of truck's suspension. *Vehicle System Dynamics, 27*(5-6), 289-303.

Verros, G., Natsiavas, S., & Papadimitriou, C. (2005). Design optimization of quarter-car models with passive and semi-active suspensions under random road excitation. *Journal of Vibration and Control, 11*(5), 581-606.

Wang, Z., Chen, Z., & Spencer Jr, B. F. (2009). Self-powered and sensing control system based on MR damper: presentation and application. *Proc. SPIE 7292, Sensors and Smart Structures Technologies for Civil, Mechanical, and Aerospace Systems*, 729240.

Williams, C. B., & Yates, R. B. (1996). Analysis of a micro-electric generator for microsystems. *Sensors and Actuators A: Physical, 52*(1), 8-11.

Williams, C. B., Shearwood, C., Harradine, M. A., Mellor, P. H., Birch, T. S., & Yates, R. B. (2001). Development of an electromagnetic micro-generator. *In IEE Proceedings- Circuits, Devices and Systems, 148*(6), 337-342.

Yao, G. Z., & Yeo, S. H. (2002). MR damper and its application for semi-active control of vehicle suspension system. *Mechatronics, 12*(7), 963-973.

Zhang, H. W., & Li, W. (2009). Comparison between skyhook and minimax control strategies for semi-active suspension system. *World Academy of Science, Engineering and Technology, 55*, (pp. 618-621).

Zhang, Y., Huang, K., Yu, F., Gu, Y., & Li, D. (2007). Experimental verification of energy-regenerative feasibility for an automotive electrical suspension system. *IEEE International Conference on Vehicular Electronics and Safety. ICVES*, (pp. 1-5).

Zhao, S., & Erturk, A. (2013). Electroelastic modeling and experimental validations of piezoelectric energy harvesting from broadband random vibrations of cantilevered bimorphs. *Smart Materials and Structures, 22*(1), 015002.

Zheng, X. C., Yu, F., & Zhang, Y. C. (2008). A novel energy-regenerative active suspension for vehicles. *Journal of Shanghai Jiaotong University (Science), 13*, 184-188.

Zhu, D., Tudor, J. M., & Beeby, P. S. (2010). Strategies for increasing the operating frequency range of vibration energy harvesters: a review. *Measurement Science and Technology, 21*(2), 022001.

Zuo, L., & Nayfeh, S. A. (2003). Low order continuous-time filters for approximation of the ISO 2631-1 human vibration sensitivity weightings. *Journal of Sound and Vibration, 265*(2), 459-465.

Zuo, L., & Zhang, P. S. (2013). Energy harvesting, ride comfort, and road handling of regenerative vehicle suspensions. *Journal of Vibration and Acoustics, 135*(1), 011002.